

AD-A072 009

STANFORD UNIV CALIF EDWARD L GINZTON LAB
LASER PHYSICS AND LASER TECHNIQUES.(U)
APR 79 A E SIEGMAN, R L BYER

F/6 20/5

UNCLASSIFIED

6L-2953

AFOSR-TR-79-0891

F49620-77-C-0092

NL

1 of 2
AD
A072009



AFOSR-TR- 79 - 0891

Edward L. Ginzton Laboratory
W. W. Hansen Laboratories of Physics
Stanford University
Stanford, California

LEVEL

A041714

LASER PHYSICS AND LASER TECHNIQUES

Annual Technical Report

for

Air Force Office of Scientific Research

Contract No. F49620-77-C-0092

for the period

1 January 1978 - 31 December 1978

Principal Investigators:

Professor A. E. Siegman
Professor R. L. Byer

G.L. Report No. 2953

April 1979

Approved for public release;
distribution unlimited.

79 07 27 073

ADA072009

DDC FILE COPY

DDC
RECEIVED
JUL 31 1979
RECEIVED
C

1. REPORT NUMBER AFOSR-TR-79-0891		2. GOVT ACCESSION NO.		3. RECIPIENT'S CATALOG NUMBER 19TR-79-0891	
4. TITLE (and Subtitle) LASER PHYSICS AND LASER TECHNIQUES				5. TYPE OF REPORT & PERIOD COVERED Annual Technical Report, 1 January - 31 December 1978	
7. AUTHOR(s) Professor A. E. Siegman Professor R. L. Byer				6. PERFORMING ORG. REPORT NUMBER GL-2953	
9. PERFORMING ORGANIZATION NAME AND ADDRESS Edward L. Ginzton Laboratory Stanford University Stanford, California 94305				8. CONTRACT OR GRANT NUMBER(s) F49620-77-C-0092	
11. CONTROLLING OFFICE NAME AND ADDRESS Air Force of Scientific Research Bolling AFB, Bldg. 410 Wash DC 20332				10. PROGRAM ELEMENT, PROJECT, TASK AREA & WORK UNIT NUMBERS 61102F/2301/A1	
14. MONITORING AGENCY NAME & ADDRESS (if different from Controlling Office)				12. REPORT DATE April 1979	
16. DISTRIBUTION STATEMENT (of this Report) Approved for public release; distribution unlimited.				13. NUMBER OF PAGES 175	
17. DISTRIBUTION STATEMENT (of this abstract entered in Block 20, if different from Report)				15. SECURITY CLASS. (of this report) unclassified	
18. SUPPLEMENTARY NOTES					
19. KEY WORDS (Continue on reverse side if necessary and identify by block number) Nonlinear Optics Harmonic Generation Optical Parametric Oscillation Hankel Transform Bessel Transform Optically Pumped Laser Mercury Laser Laser Frequency Stabilization					
20. ABSTRACT (Continue on reverse side if necessary and identify by block number) A program of basic research in laser physics and laser techniques has been carried out in order to help meet Air Force mid-term and long-term requirements as outlined in the AFSC Research Planning Guide. A Fast Hankel transform algorithm has been developed and applied to nonlinear interactions and to diffraction biased resonators studies. Picosecond spectroscopy via the induced grating approach has been successfully used to study fast relaxation processes. Optical parametric amplifiers and oscillators have been shown to be useful sources of coherent radiation over the 0.4 μ m to 4 μ m spectral range. Finally, <i>next page</i>					

DD FORM 1 JAN 73 1473

micrometers UNCLASSIFIED

11 SECURITY CLASSIFICATION OF THIS PAGE (When Data Entered)

Unclassified

stimulated Raman scattering and four-wave mixing has been used for efficient frequency conversion in the infrared. Detailed studies have shown excellent theoretical and experimental agreement in the Raman interactions.

ABSTRACT

A program of basic research in laser physics and laser techniques has been carried out in order to help meet Air Force mid-term and long-term requirements as outlined in the AFSC Research Planning Guide. A Fast Hankel transform algorithm has been developed and applied to non-linear interactions and to diffraction biased resonators studies. Pico-second spectroscopy via the induced grating approach has been successfully used to study fast relaxation processes. Optical parametric amplifiers and oscillators have been shown to be useful sources of coherent radiation over the 0.4 μm to 4 μm spectral range. Finally, stimulated Raman scattering and four-wave mixing has been used for efficient frequency conversion in the infrared. Detailed studies have shown excellent theoretical and experimental agreement in the Raman interaction.

Accession For	
NTIS GRL&I	<input checked="" type="checkbox"/>
DDC TAB	<input type="checkbox"/>
Unannounced	<input type="checkbox"/>
Justification	
By _____	
Distribution/	
Availability Codes	
Dist	Avail and/or special
<i>A</i>	

AIR FORCE OFFICE OF SCIENTIFIC RESEARCH (AFSC)
 NOTICE OF TRANSMITTAL TO DDC
 This technical report has been reviewed and is
 approved for public release IAW AFR 190-12 (7b).
 Distribution is unlimited.
 A. D. BLOSE
 Technical Information Officer

TABLE OF CONTENTS

	Page
Abstract.	iv
Personnel Involved in the Research Program.	vi
I. Introduction.	1
II. Optical Beam and Resonator Calculations	1
III. Picosecond Spectroscopy	3
IV. Optical Parametric Oscillator and Amplifier Studies	4
V. Stimulated Raman Studies.	5
VI. References -- Publications and Conference Papers.	7
Appendices:	
I. J. R. Salcedo and A. E. Siegman, "Laser Induced Photoacoustic Grating Effects in Molecular Crystals" . .	10
II. R. A. Baumgartner and R. L. Byer, "Optical Parametric Amplification".	20
III. S. J. Brosnan and R. L. Byer, "Optical Parametric Oscillator Threshold and Linewidth Studies"	81
IV. W. R. Trutna and R. L. Byer, "16 μm Generation by CO ₂ Pumped Rotational Raman Scattering in H ₂	170

PERSONNEL INVOLVED IN THE RESEARCH PROGRAM

Professor A.E. Siegman

Professor R.L. Byer

Dr. Jose R. Salcedo, Research Associate

Dr. W.R. Trutna Ph.D

Dr. R.A. Baumgartner Ph.D

Dr. S.J. Brosnan Ph.D

Shinan Chur Sheng

Yong Kwan Park

REVIEW OF ACCOMPLISHMENTS

I. INTRODUCTION

This annual report covers research work carried out by Professor A. E. Siegman in the areas of optical beam and resonator calculations and by Professor R. L. Byer in the areas of optical parametric amplifier and oscillator studies and stimulated Raman scattering studies.

During the past year several important results have been obtained under this research program. In particular, advances have been made in the application of the Fast Hankel transform algorithm to the problems of nonlinear interactions and diffraction biasing to prevent locking of ring gyroscopes. Picosecond spectroscopy techniques have been extended to the laser induced grating technique and to photo-acoustic spectroscopy. Detailed theoretical and experimental results were obtained for both optical parametric amplifiers and optical parametric oscillators. Finally, stimulated Raman scattering was studied and applied to problems of efficient frequency conversion in the infrared spectral range.

These studies have led to publications which are listed below and to the completion of four Ph.D. theses.

II. OPTICAL BEAM AND RESONATOR CALCULATIONS

During the past year very substantial steps were accomplished in completing and testing the novel Fast Hankel transform algorithm that we first invented,¹ and in applying it to optical calculations, particularly to

optical resonator and optical beam propagation calculations of importance to high power laser applications. Extensions to the algorithm itself included a simple "lower end correction" technique to compensate for the finite truncation of the transform integral at the lower end of the integration range; more accurate ways of handling the discrete Fast Fourier transform steps involved in the calculation; and better understanding of the choice of sampling intervals in the calculation. These improvements brought the accuracy of the transform close to the limits of single precision arithmetic on our machine (fractional error $\sim 10^{-6}$). In addition, a two-stage FHT algorithm requiring roughly twice the storage and computation time was developed which reduces the error of the algorithm itself, within its range of validity, to below $\sim 10^{-12}$ which is probably better than will ever be needed.

In addition substantial understanding was developed and testing carried out on the ranges of applicability of the transform, especially in optical beam calculations, in order to overcome the brute-force, cut-and-try methods too often used in these calculations. Some of these results were reported at the 1978 Annual Meeting of the OSA² and a major publication summarizing all of this work to date will be completed and submitted for publication shortly.³

Work on the application of fast transform methods to nonlinear beam calculations⁴ was also carried to completion. These results will be published in the near future.⁵

There is still useful work to be done on this topic. In particular, with the FHT algorithm itself now essentially completed it would be very useful to test and verify the heuristic "hand waving" criteria generally

used to select number of points and sampling size in optical diffraction calculations, so as to define the best compromise between accuracy and minimum number of points. The trade-off between "two-step" and "one-step" transform propagation methods needs to be tested, especially the alleged sensitivity to under-sampling of the latter. Many useful special resonator types, such as hole coupled and soft edged unstable resonators, need to be studied. We are continuing to work on all of these topics.

Finally, a rather different and unusual technique of "diffraction biasing" to obtain non-reciprocal propagation and freedom from locking in ring laser gyroscopes was invented and is being submitted for publication.⁶ Whether this technique will be of practical importance remains to be seen, but it does represent a quite different and novel attack on a long standing problem of substantial importance to Air Force requirements.

III. PICOSECOND SPECTROSCOPY

Some very interesting measurements on the picosecond spectroscopy of ultrafast relaxation times in solids were completed during this year, using the novel transient laser-induced grating technique developed in our group. The measurements demonstrated in particular a novel photo-acoustic pressure-induced amplitude grating effect in molecular crystals, of a type which does not appear to have ever been observed previously. This work was reported at the 1978 OSA Meeting⁷ and a complete publication is now in press.⁸ A preprint of this article is attached as Appendix I of this report.

An excellent Ph.D. dissertation on this topic was completed by Dr. Jose Salcedo at the end of this year.⁹ Dr. Salcedo will be staying on as a post-doctoral fellow to provide very valuable assistance in continuing this

research, at no cost to this contract.

IV. OPTICAL PARAMETRIC OSCILLATOR AND AMPLIFIER STUDIES

During this past year two extensive theoretical and experimental studies were completed on optical parametric amplification¹⁰ and optical parametric oscillators.¹¹

The gain, conversion efficiency and tuning behavior of KD*P and LiNbO₃ OPA's were studied in detail. The experimental results were shown to be in excellent agreement with theory. These results underscored the importance of OPA's as efficient, widely tunable, coherent radiation sources across the visible and near infrared spectral regions. The work was part of the Ph.D. thesis of Dr. Richard Baumgartner¹² and is to be published in the June issue of the Journal of Quantum Electronics. A preprint of the paper is attached as Appendix II. This work presented the first quantitative study of parametric amplifiers since their discovery in 1965.

A second detailed study of the threshold and linewidth of a LiNbO₃ optical parametric oscillator was completed recently. This study, which fulfilled part of the Ph.D. requirement for Dr. S. J. Brosnan,¹³ for the first time compared detailed theoretical models for OPO operation with careful measurements. The results were submitted for publication and have been accepted as an invited paper for the June issue of the Journal of Quantum Electronics.¹¹ The threshold and conversion efficiency behavior of an OPO is now well characterized. In addition, linewidth studies led to successful operation of the OPO at 8 mJ per pulse at 10 pps in a stable single axial mode. A preprint of this paper is attached as Appendix III.

V. STIMULATED RAMAN STUDIES

During the past year we completed detailed studies of stimulated Raman processes for conversion of tunable radiation sources to new frequencies. The work considered both stimulated emission processes and four-wave mixing interactions and the close coupling of the two phenomena.

We have theoretically and experimentally verified the pump linewidth independence of stimulated Raman scattering.^{14,15} This work was prepared for publication and is to appear in the July issue of the Journal of Quantum Electronics. The theoretical study showed in an elegant manner via coupled mode analysis the important role four-wave mixing plays in the stimulated Raman scattering process.

The threshold/bandwidth studies were undertaken in support of infrared rotational stimulated Raman studies in hydrogen gas at 10.6 μm . In a very important experiment, we were able to achieve 40% photon conversion efficiency from 10.6 μm to 16.95 μm by stimulated Raman scattering.^{16,17,18} This experiment demonstrated, for the first time, that efficient conversion of high energy and peak power infrared sources was possible by the stimulated Raman scattering approach. The results of the rotational Raman experiment have been published and are attached as Appendix IV.

It should be noted that for the first time it is possible to conceive of arbitrarily large energies available over the 8 μm to 20 μm spectral region by rotational Raman scattering of a pressure tunable CO_2 laser source in H_2 , D_2 and HD. Thus, Raman scattering should play an increasingly important role in the generation of tunable high average power infrared radiation.

In a separate study we quantitatively compared in detail four-wave mixing theory and experiment for application to a widely tunable infrared source. This work was also part of Dr. S. J. Brosnan's Ph.D. thesis.¹³ The thesis is now being prepared as a Ginzton Laboratory report and as a technical report for this program. The four-wave mixing studies showed that continuously tunable coherent radiation is now available over the extended 4 - 18 μm spectral range from a LiNbO_3 OPO pumped H_2 mixing cell. The results are being prepared for publication.¹⁹

A key technical innovation of the Raman studies was the invention and demonstration of a multiple pass Raman cell.²⁰ The cell allowed significant reduction in Raman pump power by providing 25 passes in a re-focusing geometry. The technical paper describing the multiple pass cell is being prepared for publication. The cell is also the subject of a patent application under Air Force Office of Scientific Research support.

VI. REFERENCES -- PUBLICATIONS AND CONFERENCE PAPERS

1. A. E. Siegman, "Quasi Fast Hankel Transform," Optics Lett. 1, 13 (July 1977).
2. A. E. Siegman and Shinan-Chur Sheng, "Optical Beam Calculations Using the Fast Hankel Transform," (Paper FD10, Abstract Only), J. Opt. Soc. Am. 68, 1436 (October 1978). Paper presented at the 1978 Annual Meeting of the O.S.A.
3. A. E. Siegman and Shinan-Chur Sheng, "The Fast Hankel Transform Algorithm." To be submitted for publication.
4. A. E. Siegman, Shinan-Chur Sheng, and Amos A. Hardy, "Nonlinear Optical Beam Calculations using Transform Methods," J. Opt. Soc. Am. 67, 1396 (October 1977). Paper WG16 presented at the Annual Meeting of the Optical Society of America, Toronto, October 1977.
5. Shinan-Chur Sheng and A. E. Siegman, "Computational Methods for Nonlinear Optical Beam Interactions: Second Harmonic Generation with Depletion and Diffraction," to be submitted for publication.
6. Shinan-Chur Sheng, "Diffraction Biased Unstable Ring Resonators with Possible Applications in Laser Gyroscopes," to be submitted for publication.
7. J. R. Salcedo and A. E. Siegman, "Amplitude Grating Effects Produced by Picosecond Laser Produced Acoustic Waves," (Paper THC10, abstract only), J. Opt. Soc. Am. 68, 1412 (October 1978). Paper presented at the 1978 Annual Meeting of OSA.

8. J. R. Salcedo and A. E. Siegman, "Laser Induced Photoacoustic Grating Effects in Molecular Crystals," IEEE J. Quant. Electr., accepted for publication April 1979.
9. J. R. Salcedo, "The Picosecond Transient Grating Technique: Studies on Energy Transport and Photo-acoustic Effects," Ph.D. Dissertation Stanford University, Stanford, California (February 1979).
10. B. A. Baumgartner and R. L. Byer, "Optical Parametric Amplification," to be published in the June 1979 issue of IEEE J. Quant. Electr.
11. S. J. Brosnan and R. L. Byer, "Threshold and Linewidth Studies of a LiNbO_3 Optical Parametric Oscillator," to be published as an invited paper in the IEEE J. Quant. Electr. June 1979 issue.
12. R. L. Baumgartner, "Optical Parametric Amplification and Applications to Remote Air Pollution Monitoring," Ph.D. Dissertation, Stanford University, Stanford, California (September 1978).
13. S. J. Brosnan, "Tunable Infrared Generation by Raman and Parametric Processes," Ph.D. Dissertation, Stanford University, Stanford, California (April 1979).
14. W. R. Trutna, Y. K. Park, and R. L. Byer, "Dependence of Raman Gain on Pump Laser Bandwidth," to be published in IEEE J. Quant. Electr. July 1979 issue.
15. W. R. Trutna, Y.K. Park, and R. L. Byer, "The Bandwidth Independence of Stimulated Raman Scattering," presented at the OSA Meeting, October 1978, San Francisco, California.
16. R. L. Byer and W. R. Trutna, " $16\text{ }\mu\text{m}$ Generation by CO_2 Pumped Rotational Raman Scattering in H_2 ," presented as a post-deadline paper at the Int'l. Quant. Electr. Conf., Atlanta, Georgia, June 1978; published in J. Opt. Soc. Am. 68, 1622 (1978).

17. R. L. Byer and W. R. Trutna, "16 μm Generation by CO_2 Pumped Rotational Raman Scattering in H_2 ," Optics Lett. 3, 144 (1978).
18. R. L. Byer, "16 μm Generation via Stimulated Rotational Raman Scattering at 10 μm ," Invited paper, Optical Society of America Meeting October 1978, San Francisco, California
19. S. J. Brosnan and R. L. Byer, "Infrared Generation via Four-Wave Mixing in H_2 Gas," to be published.
20. W. R. Trutna and R. L. Byer, "A Multipass Cell and Application to Raman Scattering," to be published in Appl. Optics.

APPENDIX I

J. R. Salcedo and A. E. Siegman, "Laser Induced Photo-
acoustic Grating Effects in Molecular Crystals"

J. R. SALCEDO AND A. E. SIEGMAN, FELLOW, IEEE

Abstract—A transient grating of singlet electronic excited states is produced in a pentacene-doped p-terphenyl molecular crystal by optical absorption from two crossed time-coincident picosecond excitation pulses at 532 nm. The diffraction properties of this volume grating are probed by a weak, variably delayed, Bragg-matched picosecond probe pulse. At high excitation intensities, a strong oscillatory behavior in the time-dependent scattering efficiency is observed superimposed on the exponential decay pattern of the excited-state grating. We attribute the oscillatory behavior to a thermal grating which induces coherent microwave acoustic phonons. These in turn modulate, at the sound frequency, the optical absorption properties of the pentacene molecules in the excited state. An acoustically induced amplitude grating effect is thus obtained, in contrast to conventional acousto-optic phase grating effects.

I. INTRODUCTION

WE report the observation of strong photoacoustic effects in molecular crystals, and particularly the observation of an acoustooptic *amplitude* grating effect, obtained while applying the picosecond transient grating method to the study of energy migration processes in molecular crystals.

The details of our transient-grating method and of the energy migration studies have been given elsewhere [1], [2], but it may be appropriate to briefly review the transient grating concept. Two coherent, time-coincident picosecond excitation pulses are transmitted through an experimental sample which is absorbing at the excitation wavelength, as in Fig. 1. In the experiment described here the absorbers consist of organic molecules (pentacene) imbedded in a transparent crystalline host (p-terphenyl). Optical absorption in the interference pattern between the two excitation beams produces a volume grating pattern of electronic singlet excited states of the pentacene molecules. This excited-state grating then acts as an optical absorption grating or "transient hologram." The time-dependent decay of the excited-state grating is probed by Bragg diffraction of a weak, variably delayed picosecond probe pulse. The intensity of the diffracted probe pulse is monitored as a function of probe pulse delay. In the case at hand, the grating pattern decays through a combination of excited-state decay and excited-state transport (which washes out the grating fringes). For purely diffusive excited-state energy transport, the decay is exponential, and the decay rate gives the transport parameters directly. A diffusion coefficient for the singlet excited electronic states of pentacene in p-terphenyl has thus been obtained [2].

Manuscript received November 13, 1978. This work was supported by the Air Force Office of Scientific Research.

The authors are with the Edward L. Ginzton Laboratory and the Department of Electrical Engineering, Stanford University, Stanford, CA 94305.

Laser Induced Photoacoustic Grating Effects in Molecular Crystals

To: The Author
Do you wish the IEEE to return your art work?
Yes No

THIS PAGE IS BEST QUALITY PRACTICABLE
FROM COPY FURNISHED TO DDC

When we performed the same experiments at optical excitation intensities above $\sim 500 \text{ MW/cm}^2$, a strong well defined oscillatory behavior in the scattering efficiency versus decay was observed. In this paper we interpret this oscillatory behavior as due to strong photoacoustic effects. At high excitation intensities, a significant thermal grating is superimposed on the excited-state grating. This thermal grating produces a transient disturbance which can be described as a "frozen" stress pattern plus two counterpropagating coherent microwave acoustic waves [3]. The density modulation associated with this disturbance modulates, at the microwave sound frequency, predominantly the optical absorption cross section of the pentacene excited electronic singlet states, most likely by pressure tuning the absorption line. This in turn modulates the effective depth of the excited-state grating and thus its scattering efficiency, producing an amplitude grating effect. To our knowledge, such photoacoustic amplitude grating effects have not been previously observed. They provide interesting information on phonon processes and on pressure tuning in the crystals, in addition to preserving the excited-state transport information.

II. EXPERIMENTAL OBSERVATIONS

A. Apparatus

28
The experimental apparatus for these studies is outlined in Fig. 2. A continuously pumped, high repetition rate, Q-switched and actively mode locked Nd:YAG laser [4] produces bursts of mode-locked pulses, from which single pulses are selected by a LiNbO₃ Pockels cell in a Blumlein configuration. These pulses are efficiently doubled to 532 nm by a temperature-tuned 90°-phase-matched CD* A crystal, and split into two strong excitation pulses ($\approx 300 \text{ kW}$ peak power each) and a weak variably delayed probe pulse ($\approx 20 \text{ kW}$). All pulses are linearly polarized in the plane of the figure, and are Gaussian in time and in space with a duration [full width at half maximum (FWHM)] of 50-75 ps. Due to the particular optical absorption properties of pentacene at 532 nm, excitation and probe pulses are chosen to be at the same wavelength. To meet the Bragg condition, the probe pulse is brought from the back of the crystal along the reverse path of one of the excitation pulses, but with its polarization rotated by 90°. The first-order Bragg-diffracted pulse preserves this polarization and is scattered along the reverse path of the other excitation pulse. A polarization beam splitter then deflects the signal into a photodetector connected to a lock-in amplifier. The lock-in output drives the y axis of an X-Y recorder, while the x axis is driven by the motorized probe pulse delay line. For slow delay scan rate and high laser repetition rate (100 Hz), data gathering is essentially continuous in a stroboscopic sense. Each experimental plot contains typically 50 000-100 000 laser shots and takes 10 min to complete. Observed scattering efficiencies are typically several percent, yielding high signal to noise ratio in the measurements ($S/N \approx 100$ is easily achieved). To further enhance the signal discrimination, every other pair of excitation pulses is chopped and phase sensitive detection is used. A microscope objective can also be used to image the interaction volume onto a vidicon tube with large magnification, allowing the display of the grating fringes on a television monitor. This provides a very accurate tool to align all three beams in the crystal.

THIS PAGE IS BEST QUALITY FRAGMENT
FROM COPY FURNISHED TO DDC

B. Results

Results showing diffusive energy transport at low excitation intensity have been previously reported and studied [2]. Here we concentrate on the high excitation intensity results, which show the oscillatory character of the time-dependent scattering efficiency. Fig. 3 shows this oscillatory dependence as observed in four experiments from a series performed under identical conditions except for different fringe spacings Λ , which are adjusted by changing the angle between the two excitation beams. In all these results the grating k vector is parallel to the crystal b axis. The time period T of the oscillatory modulation changes with fringe spacing Λ with the linear dependence shown in Fig. 4. A straight-line fit yields a slope of 2.63×10^3 cm/s, which we take to be the velocity of sound. The velocity of sound in the same crystal along the same direction was independently measured to be $v_s = 2.65 \pm 0.05$ cm/s, confirming the acoustic origin of the oscillations.

Further examination of the shape of the oscillatory decays in Fig. 3 leads us to conclude that the observed effects must result from thermal excitation of an acoustooptic amplitude grating. This grating must be produced, we believe, by acoustic pressure tuning of the excited molecular state absorption in the sample. The theoretical analysis supporting these conclusions is outlined in the following section.

III. THEORETICAL FORMULATION

A. Time Dependence of the Scattering Efficiency

The geometrical and parametric dependence of the scattering efficiency of volume holograms is well known [5], [6]. Here we are mainly interested in the exponentially decaying and oscillating time dependence of the observed scattering from the volume grating patterns produced by thermal plus excited-state gratings in our experiments. In these experiments scattered probe signals were observed primarily at the first-order Bragg-matching angle. However, the volume grating pattern also contains higher spatial harmonics, particularly at the second-order Bragg angle, which should also be observable. In general the diffracted probe signal intensity $I_n(t)$ at the n th order Bragg matching angle is given by

$$I_n(t) = \int_{-\infty}^{\infty} I_p(t' - t) |I_e(t') * \chi_n(t')|^2 dt' \quad (1)$$

where the $*$ denotes convolution, and $I_p(t' - t)$ and $I_e(t')$ are the probe and excitation pulse intensities, with the probe pulse being delayed in time by an amount t . Out of the total complex susceptibility $\chi(x, t)$ in the sample the relevant part is the spatial Fourier component of order n , i.e., the component $\chi_n(t) \exp(inkx)$, which corresponds to spatial vector $nk = n2\pi/\Lambda$, where Λ is the grating spacing. As written here, $\chi(x, t)$ is the Green's function or the unit impulse response produced by an excitation pulse that is a unit impulse in time. In this paper we will, in fact, treat the excitation pulse $I_e(t)$ as a unit impulse, since the ~ 70 ps excitation (and probe) pulses are short compared to the ~ 1 ns oscillation and decay times in these experiments. The scattering susceptibility $\chi_n(t)$ is in general complex, i.e., $\chi_n = \chi_n' + j\chi_n''$, with the real part being responsible for phase grating or index of refraction grating effects, and the imaginary part being responsible for amplitude or absorption grating effects.

The physical process that produces the coherent acoustic waves of interest here is a thermally induced acoustic grating which is superimposed on the excited-state grating [2]. The thermal grating and the associated acoustic waves can be analyzed starting from the linearized hydrodynamic equations [7] - [9]

$$\frac{\partial^2 \Delta \rho}{\partial t^2} + \frac{v_s^2}{\gamma} \nabla^2 \Delta \rho - \frac{\eta}{\rho_0} \frac{\partial}{\partial t} \nabla^2 \Delta \rho - \frac{v_s \beta \rho_0}{\gamma} \nabla^2 \Delta T = 0$$

$$\frac{\partial \Delta T}{\partial t} - \frac{\lambda}{\rho_0 c_p} \nabla^2 \Delta T - \frac{\gamma}{\beta \rho_0} \frac{1}{\partial t} \frac{\partial \Delta \rho}{\partial t} = \frac{n^2 \alpha}{4\pi \rho_0 c_p} (E^2). \quad (2)$$

Here ΔT and $\Delta \rho$ are the local temperature and density changes, ρ_0 is the equilibrium density, η is the viscosity, β is the expansion coefficient, λ is the thermal conductivity, α is the optical absorption coefficient, and E is the local optical electric field in the interaction volume. Electrostriction can be neglected, and the transient solution for the density variation $\Delta \rho$ can then be readily obtained [8] for an excitation pulse very short compared to the acoustic times of interest:

$$\Delta \rho(x, t) = \Delta \rho_{\max} [e^{-t/\tau_{ac}} \cos \omega t - e^{-t/\tau_{th}}] \cos(2\pi x/\Lambda) \quad (3)$$

Here τ_{ac} is the acoustic wave attenuation time or sound absorption time, τ_{th} is the thermal conduction time, and $\omega = 2\pi/\tau_A$ is the acoustic frequency where $\tau_A = \Lambda/v_s$, with v_s being the acoustic wave velocity. For the acoustic frequencies generated in these experiments ($\omega/2\pi \sim 300$ -800 MHz), the acoustic decay time is $\tau_{ac} \sim 50$ -100 ns, and the thermal conduction decay time can be ignored.

A more complete analysis would take into account the Gaussian transverse spatial dependence of the excitation beams, as well as the finite duration of the excitation pulse $I_e(t)$. In particular there will be an additional effective decay of the acoustic signals as the finite trains of left- and right-going acoustic cycles move across each other and eventually cease to overlap spatially with each other. Since our gratings typically had at least 20 fringes across the half width of the beam spot size, however, this had little effect during the 5 or 6 acoustic cycles typically followed in our experiments.

Although we will speak loosely of pressure tuning effects, we attribute the observed effects in our experiments to induced changes in the local optical properties of the medium caused primarily by local density changes rather than either local temperature, local stress, or pressure effects. Fig. 5 is a plot of the excited state grating pattern $N_1(x, t=0)$, the ground state molecular density $N_0(x, t=0)$, and the instantaneous local density change $\Delta \rho(x, t)$, with the latter quantity being plotted at successive instants of time through one complete acoustic cycle, neglecting damping or decay effects. The acoustic density grating pattern is in phase spatially with the excited-state grating pattern, as well as with the sinusoidal part of the ground state molecular density. Because of the instantaneous nature of the thermal excitation in bulk, both the density and the pressure must be described as having a static or "frozen" grating component as well as two counterpropagating traveling-wave components. (The "frozen" components will of course decay away with a much longer thermal relaxation time.) Note also that the density variations with time at any one point in space are "one-sided," i.e., the local density swings up and back, or down and back, but not both up and down at any one location. The molecular densities $N_0(x)$ and $N_1(x)$ decay slowly due to excited-state relaxation and diffusion.

B. Phase Versus Amplitude Grating Effects

Conventional acoustooptic interactions in solids nearly always occur through a phase grating mechanism, caused by a change in local index of refraction associated with the acoustic disturbance. Examination of the theoretical expressions and of Fig. 5 shows, however, that this cannot be the primary explanation for our observations, and that we are clearly observing an acoustooptic amplitude grating effect.

In our results the instantaneous scattering efficiency is seen to be reduced nearly to zero at each odd half acoustic cycle after the excitation pulse. This is also the instant when the density grating reaches its maximum amplitude in spatial phase with the excited-state grating. The implication is that the density-induced scattering at those instants must add in opposite phase (not in quadrature) to the excited-state induced grating. We believe the excited state grating must surely be an amplitude grating, and hence the density-induced grating must be an amplitude rather than a phase grating also.

viscosity

Fig. 5

THIS PAGE IS BEST QUALITY PRINTING
 FROM COPY FURNISHED TO DDC

Equation (3) shows that the density grating consists of two traveling-wave components of relative amplitude $\pm \frac{1}{2}$ each, and a fixed or constant component of relative amplitude -1. The two traveling-wave components decay with the acoustic decay time τ_{ac} , which lasts 25-50 acoustic cycles, while the fixed component decays with the thermal decay time τ_{th} , which is much longer. Each of these components will induce a scattered signal field component at the Bragg angle, with corresponding amplitudes and phases. Note that the three density grating components, and also the three vectorial scattered wave components, sum to exactly 0 at $t=0$ since the density modulation starts from an initial value that is identically zero.

Fig. 6 shows vectorially in the complex plane the scattered vector field amplitudes contributed by each of these three density wave components, plus the larger component contributed by the excited-state grating, at three instants of time corresponding to 0, $\frac{1}{2}$, and 1 acoustic cycle. The sketches are drawn with vertical arrows representing the excited state grating, assumed to be a pure amplitude grating. The heavy arrow in each case is the vector sum, or the instantaneous vector amplitude of the total Bragg-scattered signal field. The length of this vector squared would give the total Bragg-scattered intensity at that instant.

The upper sketch assumes that the density waves induce a phase grating effect, i.e., the three acoustically induced components are 90° out of phase with the excited-state grating component; while the lower sketch assumes the density wave components are in phase with the excited-state component. The two smaller density wave components rotate in opposite directions in the complex plane at the acoustic frequency, since they represent oscillating or traveling-wave terms. Note that the observed amplitude variation of the total scattered signal with time can only be explained by the lower sketch. An acoustic phase grating would, in fact, cause the total scattered intensity to have an amplitude variation of opposite sign.

C. Detailed Analysis of the Scattering Efficiency

Leaving aside inessential constants and geometrical factors, the scattering susceptibility $\chi_n(t)$ can be written as

$$\chi_n(t) = i \left\{ \sum_i N_{i,p}(x, t) \sigma_{i,p}(x, t) \right\}_n \quad (4)$$

where $N_{i,p}$ and $\sigma_{i,p}$ are the density-modulated molecular state populations and cross sections, respectively, and where the subscript n indicates that only the $\exp(jn2\pi x/\Lambda)$ spatial component is to be considered. The sum in the present case extends over two levels, the ground state $i=0$ and the first excited singlet level $i=1$. The population and cross sections may be written as

$$\begin{aligned} N_{i,p}(x, t) &= N_i(x, t) [1 + \Delta\rho(x, t)/\rho_0] \\ \sigma_{i,p}(x, t) &= \sigma_i + (\partial\sigma_i/\partial\rho) \Delta\rho(x, t) \end{aligned} \quad (5)$$

where $N_i(x, t)$ and σ_i without arguments give the unperturbed values. The values both of σ_i and of their derivatives may in general be complex, with the real part corresponding to absorption and the imaginary part corresponding to phase shift or index of refraction effects.

The general expression for $\Delta\rho(x, t)$ has been given in (3). The populations of the ground and excited levels produced by the excitation beam delta functions are [2]

$$\begin{aligned} N_1(x, t) &= \frac{1}{2} N_1^{\max} e^{-t/\tau} [1 - e^{-k^2 D t} \cos(2\pi x/\Lambda)] \\ N_0(x, t) &= N_0 - N_1(x, t) \end{aligned} \quad (6)$$

THIS PAGE IS BEST QUALITY PRACTICABLE
FROM COPY FURNISHED TO DDC

where N_0 without arguments is the total density of absorbing molecules in the crystal, N_1^{max} is the initial optically induced excited-state density at the grating peaks, τ is the excited state fluorescent lifetime, and $(1/\tau + k^2 D) = K/2$ is the decay rate for the excited-state fringe pattern due to excited-state relaxation plus excited-state diffusion with diffusion coefficient D .

We now define the normalized maximum density variation

$$\eta = \Delta \rho_{\text{max}} / \rho_0 \ll 1 \quad (7)$$

and the oscillatory modulation component

$$M(t) = \exp(-t/\tau_{ac}) \cos \omega t - 1. \quad (8)$$

We also define the cross section sensitivity parameters, or normalized density derivatives

$$\begin{aligned} S_0 &= (\partial \sigma_0 / \partial \rho) \rho_0 / \sigma_0 \\ S_1 &= (\partial \sigma_1 / \partial \rho) \rho_0 / \sigma_1 \end{aligned} \quad (9)$$

which could be complex or even imaginary if the density modulation produces an index of refraction grating. We then obtain the $n = 1$ Bragg angle component of the scattering susceptibility from (4), (8), and (9) as

$$\begin{aligned} -j\chi_1(t) &= (N_1^{\text{max}}/2) (\sigma_1 - \sigma_0) e^{-(1/\tau + k^2 D)t} \\ &\quad + \eta \sigma_1 (S_1 + 1) (N_1^{\text{max}}/2) e^{-t/\tau} M(t) \\ &\quad + \eta \sigma_0 (S_0 + 1) (N_0 - (N_1^{\text{max}}/2)) e^{-t/\tau} M(t). \end{aligned} \quad (10)$$

This expression contains three terms. The first is the basic excited-state transient-grating signal [2] unperturbed by acoustic effects. It gives the pure exponential decay observed at low intensities, as determined by the excited-state lifetime τ and the diffusion coefficient D . The second and third terms describe how the first excited state and ground-state diffraction effects are modulated by the thermally induced density variations or coherent acoustic waves. In the $(S_i + 1)$ factors in the second and third terms, the factor of 1 represents simple density modulation of the local molecular density, while the S_i factors represent density modulation of the molecular cross sections σ_i , as in (5). It will turn out that the magnitudes of the S_i seem to be substantially larger than unity to fit the observed results.

The resulting diffracted signal intensity is then given by

$$\begin{aligned} I_1(t) &= \int_{-\infty}^{\infty} I_0(t' - t) |e^{-(K/2)t'}| \\ &\quad + A_1 e^{-t'/\tau} M(t') \\ &\quad + A_0 (2N_0/N_1^{\text{max}} - e^{-t'/\tau}) M(t')^2 dt' \end{aligned} \quad (11)$$

where we have normalized the initial scattering efficiency to unity. The oscillatory terms have magnitudes

$$\begin{aligned} A_0 &= \frac{\eta(S_0 + 1) \sigma_0}{\sigma_1 - \sigma_0} \\ A_1 &= \frac{\eta(S_1 + 1) \sigma_1}{\sigma_1 - \sigma_0} \end{aligned} \quad (12)$$

Note that squaring this expression not only squares each of the above terms, but most importantly leads to beating effects between the basic excited-state grating and the two acoustic terms. Because the probe pulsewidth of ~ 70 ps is short compared to the time constants involved in $\chi_1(t)$, we can simplify (11) as

$$\begin{aligned} I_1(t) &= |e^{-(K/2)t} + A_1 e^{-t/\tau} M(t) \\ &\quad + A_0 (2N_0/N_1^{\text{max}} - e^{-t/\tau}) M(t)|^2 \\ &\approx e^{-K \cdot t} + A_1 M(t) e^{-t/\tau} e^{-(K/2)t} \\ &\quad + A_0 (2N_0/N_1^{\text{max}} - e^{-t/\tau}) M(t) e^{-(K/2)t}. \end{aligned} \quad (13)$$

Here we have also ignored products of order η^2 in the second line, since $\eta^2 \ll 1$.

Fig. 7 shows Eq. (13) plotted for typical values of the relevant time constants as we slowly "turn on" the excited-state density-modulation term A_1 and the ground-state density modulation term A_0 independently. The experimental parameters employed are

$$N_1^{max}/N_0 = 0.3$$

$$\tau = 9.5 \text{ ns}$$

$$\tau_{ac} \approx 100 \text{ ns}$$

$$\Lambda = 5 \mu\text{m}$$

$$v_s = 2.65 \times 10^5 \text{ cm/s}$$

$$D = 0.5 \text{ cm}^2/\text{s}$$

(14)

It clearly seems that the shape of our experimental results can be matched only by assuming that density modulation of the excited state is the dominant mechanism causing the acoustic effects. This is supported by the data shown in Fig. 8, obtained from the third plot from the top in Fig. 3. The plot shows both the exponential decay of the peak amplitudes, which gives the diffusion coefficient D , and also the decay of the depth-of-modulation amplitudes i.e., the difference between the fitting exponential and the observed amplitude at the minima. The decay rates are essentially the same, which says that the oscillatory term decays at the same rate as the grating component of $N_1(x)$, not $N_0(x)$. Only if density modulation of the excited state is the dominant mechanism can this depth of modulation decay be explained. For ground state modulation the decay would have to be significantly slower.

D. Comparison to Experimental Results

Fig. 9 repeats the experimental result of Fig. 3, second curve from the top ($\Lambda = 5.33 \mu\text{m}$), along with a semilog plot of the peak amplitudes in this curve, showing their almost exact exponential decay. At the peak times, the instantaneous density change $\Delta\rho(x, t)$ is zero, and hence the observed exponential decay rate for the peaks should be $(2/\tau + 2k^2 D)$. The observed results are in fact in agreement with low-intensity, nonoscillating measurements which give $\tau = 9.5 \text{ ns}$ and $D = 0.5 \text{ cm}^2/\text{s}$ for this particular sample. Also shown in Fig. 9 is a theoretical fit using (13) for these experimental conditions, with $A_0 = -0.02$ and $A_1 = +0.37$. Evidently it is density modulation of the excited rather than the ground level that is dominant.

From all our other measurements, we can estimate that $\sigma_1/\sigma_0 \approx 5$, and from the heat deposition and thermoacoustic properties of the material, we can estimate that in the high intensity experiments, the normalized maximum density change corresponds to $\eta \sim 10^{-3}$. From (12) we then obtain the rough values

$$(S_0 + 1) \sim -100$$

$$(S_1 + 1) \sim +500$$

$$\frac{\Delta\sigma_0}{\sigma_0} \sim +0.05$$

$$\frac{\Delta\sigma_1}{\sigma_1} \sim -0.5$$

(15)
(16)

at the peak of the acoustic wave (where $\Delta\rho/\rho_0 < 0$). There is independent support for the assumption that $\partial\sigma_0/\partial\rho < 0$, if we consider the ground state absorption spectrum of pentacene in the vicinity of 532 nm, and a static pressure tuning study of pentacene lines [10]. No data on the pressure tuning of the first singlet excited state of pentacene seems to be available, but our results imply that the net effect at 532 nm must be of opposite sign, and several times larger. The agreement shown in Fig. 9 is good, especially if we look at the simplicity of the theoretical model, in which we did not include highly nonlinear effects potentially present in the interaction volume, such as the following.

1) In the high compressibility regime produced by the laser induced acoustic waves (excess pressure ≈ 50 atm), the sound velocity can no longer be considered constant [11], and the acoustic waves can no longer be rigorously treated by a linearized model.

2) A linear dependence of cross section on density has been assumed, when in more rigor we should use the exact nonlinear absorption lineshape around 532 nm.

However, we believe including these nonlinear effects would only change the fit in Fig. 9 by a negligible amount, and in the right direction for an even more exact fit.

IV. CONCLUSION

The present paper reports the observation of amplitude grating effects produced by coherent acoustic waves induced by optical absorption of picosecond pulses. These pulses from overlapping transient excited-state and thermal gratings in the bulk of a molecular crystal. A simple model introduced to treat the coherent acoustooptic interaction fits the experimental results with quite good agreement. The results yield information about a variety of processes, including:

1) The nature and rate of energy migration for the molecular excited states, obtained by studying the decay of the oscillatory signal peaks.

2) Information regarding high-frequency acoustic phonon processes in the crystal, including acoustic velocity and attenuation. By changing the grating orientation in the crystal, anisotropic and nonlinear acoustic effects might also be directly studied.

3) Information regarding the pressure or density modulation of the ground-state and excited-state absorption in the crystal.

The amount of information simultaneously obtained from measurements such as these, concerning both molecular and crystalline properties, is sizable. We hope this process can be naturally extended to other materials as well, providing a unified understanding of their properties.

ACKNOWLEDGMENT

Earlier work on the transient grating experiments was supported by the Joint Services Electronics Program at Stanford University and by the National Science Foundation. This work grew out of studies of energy transport in pentacene carried out in collaboration with Prof. M. Fayer and D. Dlott of the Stanford Chemistry Department, and we appreciate the use of molecular crystal samples provided by them.

REFERENCES

- [1] D. W. Phillion, D. J. Kuizenga, and A. E. Siegman, "Subnanosecond relaxation time measurements using a transient induced grating method," *Appl. Phys. Lett.*, vol. 27, p. 85, 1975.
- [2] J. R. Salcedo, A. E. Siegman, D. D. Dlott, and M. D. Fayer, "Dynamics of energy transport in molecular crystals: The picosecond transient grating method," *Phys. Rev. Lett.*, vol. 41, p. 131, July 10, 1978, also in *Picosecond Phenomena*, C. V. Shank, E. P. Ippen, and S. L. Shapiro, Eds. Berlin: Springer Series in Chem. Phys., vol. 4, 1978, pp. 240-243.
- [3] D. C. Auth, "New high-power source of coherent microwave phonons," *Appl. Phys. Lett.*, vol. 16, p. 521, June 15, 1970.
- [4] D. W. Phillion, "Evolution of mode locked pulses and their application to time-resolved spectroscopy," Ph.D. dissertation, Stanford Univ., Stanford, CA, Nov. 1974.
- [5] H. Kogelnik, "Coupled wave theory for thick hologram gratings," *Bell Syst. Tech. J.*, vol. 48, p. 2909, 1969.
- [6] A. E. Siegman, "Bragg diffraction of a Gaussian beam by a crossed Gaussian volume grating," *J. Opt. Soc. Amer.*, vol. 67, p. 545, 1977.
- [7] D. R. Dean, "Optically induced diffraction gratings in liquids and solids," Office of Naval Research, Washington, DC, Tech. Rep. TR-73-02.
- [8] M. E. Mack, "Stimulated thermal Rayleigh scattering with picosecond pulses," *Ann. N.Y. Acad. Sci.*, vol. 168, p. 419, 1970.
- [9] R. Herman and M. Gray, "Theoretical prediction of the stimulated thermal Rayleigh scattering in liquids," *Phys. Rev. Lett.*, vol. 19, p. 824, 1967.
- [10] J. M. Donini, "Effet d'une compression sur les spectres de l'anthracène et du pentacène en solution dans le p-terphenyle à 1.7 K," *J. Chim. Phys.*, II, vol. 11-12, p. 1542, 1974.
- [11] H. Fiebler and H. Stahl, "Time and frequency behavior of sound waves thermally induced by modulated laser pulses," *J. Appl. Phys.*, vol. 44, p. 3429, Aug. 1973.

Fig. 1. Transient grating concept and geometry. Probe pulse is orthogonally polarized relative to excitation pulses, and signal is extracted with cube polarizer.

Fig. 2. Transient grating experimental setup.

Fig. 3. High excitation intensity transient grating results showing the dependence of the oscillation period T on the grating fringe spacing Λ , for four experimental results.

Fig. 4. Linear dependence of Λ versus T .

Fig. 5. Density wave dynamical behavior. Fringe peaks are at $x/\Lambda = 0, 1, 2, \dots$. Excited and ground state population spatial distribution at $t = 0$.

Fig. 6. Graphical (phasor) description of acoustically induced phase or amplitude grating added to excited state amplitude grating. Resultant time dependences are radically different. Only acoustically induced amplitude grating effects can explain observed time dependence.

Fig. 7. Excited state (upper) modulation and ground state (lower) modulation, for several modulation "depths" A_1 and A_0 . Although behavior may look similar, the oscillation decay is radically different, being much slower for ground state modulation.

Fig. 8. •-Peak amplitudes for third plot in Fig. 3 ($\Lambda = 4.7 \mu\text{m}$), showing excellent exponential decay. Decay time constant gives $D = 0.5 \text{ cm}^2/\text{s}$ for this particular sample, for diffusion along the b axis. X-Depth of modulation points obtained from minimum of same plot. Observed decay can only be explained if an acoustic modulation of excited state optical properties is assumed. Ground state modulation would produce a much slower decay.

minima

Fig. 9. Theoretical fit to second experimental plot in Fig. 3 ($\Lambda = 5.3 \mu\text{m}$), for $A_0 = -0.02$ and $A_1 = +0.37$.

APPENDIX II

R. A. Baumgartner and R. L. Byer, "Optical
Parametric Amplification"

TABLE OF CONTENTS

	Page
I. INTRODUCTION.....	1
II. THEORY.....	3
A. Second Order Nonlinear Interactions.....	3
B. Coupled Wave Equations.....	6
C. Special Case Solutions.....	17
D. Parametric Amplification.....	20
III. COMPUTER METHODS AND EXAMPLE SOLUTIONS.....	23
IV. PARAMETRIC AMPLIFIER EXPERIMENTS.....	26
A. Introduction.....	26
B. KD^*P OPA Experiments.....	27
C. $LiNbO_3$ OPA Experiments.....	30
V. SUMMARY AND CONCLUSIONS.....	34
Table I	36
Table II.....	37
APPENDIX I: Crystal Acceptance Angle and Bandwidth.....	38
APPENDIX II: Nonlinear Coefficient Values by Miller's Δ Scaling.....	40
VI. FIGURE CAPTIONS.....	42
VII. REFERENCES.....	44

OPTICAL PARAMETRIC AMPLIFICATION

Richard A. Baumgartner and Robert L. Byer

I. INTRODUCTION

Experiments in nonlinear optics were performed in 1961 soon after the demonstration of the laser.¹ These experiments were possible due to the increase in power spectral brightness made possible by the laser. The first mixing experiment involving three optical frequencies was performed by Wang and Racette² in 1965. Prior to that experiment the possibility of parametric gain in a three frequency process was considered theoretically by Kingston,³ Kroll,⁴ Akhmanov and Khoklov,⁵ and Armstrong, Bloembergen, Ducuing and Pershan (ABDP).⁶

Parametric oscillation, an important extension of parametric amplification, was first achieved in 1965 by Giordimaine and Miller.⁷ Parametric oscillation is quite useful for generation of widely tunable coherent radiation. The progress in parametric amplification and oscillation has been the subject of review papers by Harris,⁸ Smith,⁹ and Byer.¹⁰

Since the original experiment of Wang and Racette, laser sources for pumping parametric processes have improved considerably. Pulsed lasers are now available with energies greater than 0.5 J/pulse at repetition rates greater than ten pulses per second and operating with either a TEM₀₀ transverse mode profile or various plane wave unstable resonator beam outputs. Recent LiNbO₃ parametric

amplification experiments demonstrated that small signal gains of 50 and saturated conversion efficiencies of 20% are available. Consequently, parametric amplification is an important technique for amplification and power generation over wide frequency ranges. The detailed understanding of the parametric amplification process is also useful for the design of optical parametric oscillator tunable sources.

This paper examines the theoretical solutions of parametric amplification valid in the depleted pump regime. The solutions are compared with experimental measurements for KD^*P and LiNbO_3 optical parametric amplifiers (OPA). The theoretical derivations, based on previous work by ABDP,⁶ Boyd and Kleinman (BK)¹¹ and Harris¹² and computational methods are considered in Sections II and III. The theoretical treatment includes the transition from parametric amplification solutions with pump depletion to solutions valid where pump depletion is not important. A parametric amplifier general solution program with and without time dependence is discussed in Section III.

The experimental measurements are presented in Section IV. The experiments include small signal gain measurements of a 355 nm pumped KD^*P OPA and its angle tuning curve. The gain and energy conversion efficiency of a 1064 nm pumped LiNbO_3 OPA is also presented. The experimental results are compared with the computer solutions presented in Section III.

The theoretical and experimental results and comparisons presented in this paper are the first detailed study of the optical parametric amplifier. Together they show that OPA's are useful devices for amplification of tunable coherent radiation in the optical spectral region.

II. THEORY

A. Second Order Nonlinear Interactions

The second order nonlinear interaction of light beams is characterized by the generation of a nonlinear polarization

$$\vec{P}_3(\omega_3) = \epsilon_0 \vec{\chi}(-\omega_3, \omega_1, \omega_2) : \vec{E}_1(\omega_1) \vec{E}_2(\omega_2) \quad (1)$$

where $\vec{P}_3(\omega_3)$ is the nonlinear polarization at frequency ω_3 , ϵ_0 is the dielectric constant, $\vec{\chi}(-\omega_3, \omega_1, \omega_2)$ is the nonlinear susceptibility tensor and $E_1(\omega_1)$ and $E_2(\omega_2)$ are the interacting laser fields.

The second order nonlinear susceptibility is responsible for sum and difference frequency generation and for parametric amplification in the interaction of two laser fields in a nonlinear medium. Parametric amplification involves three frequencies related by

$$\omega_3 = \omega_1 + \omega_2 \quad (2)$$

The field at ω_3 is assumed to be the most intense. Energy at either ω_1 or ω_2 incident on the nonlinear crystal is amplified with the remaining non-incident field being generated. For an

efficient transfer of energy to occur between the waves, momentum or phase velocity phase matching, defined by the k vector relation

$$\bar{k}_3 = \bar{k}_1 + \bar{k}_2 \quad (3)$$

must be accomplished, where $|k_i| = 2\pi \lambda_i / n_i$ and n_i is the index of refraction in the crystal. For uniaxial crystalline media with birefringence, phase velocity matching¹³ can be achieved by angle tuning, crystal heating, or electro-optic effect. In the present experimental work Type I angle phase matching was used with the signal (ω_1) and idler (ω_2) fields polarized as ordinary and the pump (ω_3) field polarized as extraordinary waves in the negative birefringent LiNbO_3 and KD^*P crystals. In negative uniaxial crystals the Type I phase matching condition for collinear propagating waves is given by

$$\lambda_3 / n_e(\lambda_3, \theta) = \lambda_2 / n_o(\lambda_2) + \lambda_1 / n_o(\lambda_1)$$

where

$$\left[\frac{1}{n_e(\lambda_3, \theta)} \right]^2 = \frac{\sin^2 \theta}{n_e^2(\lambda_3)} + \frac{\cos^2 \theta}{n_o^2(\lambda_3)} \quad (4)$$

Here θ is the propagation angle relative to the optic axis and $n_e(\lambda)$ and $n_o(\lambda)$ the principle extraordinary and ordinary crystalline indices of refraction.

A phase velocity mismatch factor

$$\vec{\Delta k} = \vec{k}_3 - \vec{k}_1 - \vec{k}_2 \quad (5)$$

is a modification of Eq.(3) when phase matching is not quite achieved. Possible causes of non-zero Δk as well as finite crystal acceptance angle and bandwidth, are discussed in Appendix I.

The pump beam, propagating as an extraordinary ray in the nonlinear crystal has a power flow direction at an angle β to the wavefront normal. The Poynting vector walk-off angle for uniaxial crystals is given by

$$\tan \beta = \frac{\sin \epsilon_m \cos \epsilon_m (n_e^2 - n_o^2)}{n_e^2 \cos^2 \epsilon_m + n_o^2 \sin^2 \epsilon_m} \quad (6)$$

with a positive angle β for positive birefringent crystals. The presence of β causes a slight adjustment in the observed value of the phasematching angle ϵ_m given by

$$\epsilon_{m_{\text{obs}}} = \epsilon_{m_{\text{calc}}} + \beta \quad (7)$$

The specific nonlinear polarization relations derived from Eq.(1) are

$$P_1 = 2 \epsilon_o d_{\text{eff}} E_2^* E_3 \quad (8a)$$

$$P_2 = 2 \epsilon_o d_{\text{eff}} E_1^* E_3 \quad (8b)$$

$$P_3 = 2 \epsilon_o d_{\text{eff}} E_1 E_2 \quad (8c)$$

where the notation has been simplified by dropping the explicit frequency dependence and the susceptibility has been written in terms of an effective nonlinear coefficient. For LiNbO_3 with 3m point group symmetry

$$d_{\text{eff}} = d_{31} \sin \theta_m - d_{22} \cos \theta_m \sin 3\phi \quad (9)$$

which is maximized for $\phi = -90^\circ$. For KD^*P with $\bar{4}2\text{m}$ point group symmetry the effective nonlinear coefficient for Type I phase-matching is

$$d_{\text{eff}} = -d_{14} \sin \theta_m \sin 2\phi \quad (10)$$

which is maximized for $\phi = -45^\circ$. A derivation of the effective nonlinear coefficient used here is presented in Appendix 2 of BK.¹¹ The coordinate rotations necessary to relate d_{eff} to the d_{il} coefficient along the crystallographic axes are discussed in Zernike and Midwinter.¹⁴

B. Coupled Wave Equations

The derivation of the coupled set of wave equations proceeds from Maxwell's equations

$$\vec{\nabla} \times \vec{E} = - \frac{\partial \vec{B}}{\partial t} \quad \vec{\nabla} \times \vec{H} = \vec{J} + \frac{\partial \vec{D}}{\partial t} \quad (11a)$$

$$\vec{\nabla} \cdot \vec{D} = 0 \quad \vec{\nabla} \cdot \vec{B} = 0 \quad (11b)$$

and the constitutive relations

$$\bar{D} = \epsilon_0 \epsilon \bar{E} + \bar{P} \quad (12a)$$

$$\bar{B} = \mu_0 \bar{H} \quad (12b)$$

The linear polarization is contained in ϵ so that \bar{P} contains only the nonlinear polarization terms. The medium is assumed to be magnetically inactive. The fields obey the wave equation

$$\frac{\partial^2 \bar{E}}{\partial z^2} - \mu_0 \sigma \frac{\partial \bar{E}}{\partial t} - \mu_0 \epsilon_0 \epsilon \frac{\partial^2 \bar{E}}{\partial t^2} = \mu_0 \frac{\partial^2 \bar{P}}{\partial t^2} \quad (13)$$

and are assumed to be monochromatic plane waves propagating in the near field in the z direction. The nonlinear interaction occurs over distances and times that are large with respect to the individual sinusoidal variations of optical fields so that an envelope representation

$$E_i(z, t) = \sum_m R_e(E_{im} e^{j(\omega_m t - k_m z)}) \quad (14a)$$

$$P_i(z, t) = \sum_m R_e(P_{im} e^{j(\omega_m t - k_m z)}) \quad (14b)$$

is used. The subscript i represents the direction of polarization x or y and m the frequency of interest 1, 2 or 3. The Eqs.(14a and 14b) are substituted into Eq.(13) and the slowly varying

envelope approximations are applied leading to

$$\frac{\partial F_m}{\partial z} + (n_m/c) \frac{\partial F_m}{\partial t} + \alpha_m F_m = -j \frac{\nu_0 c \omega_m}{2n_m} P_m \quad (15)$$

where $n_m = (\epsilon_m)^{\frac{1}{2}}$ and $\alpha_m = \frac{1}{2} \nu_0 \sigma c / n_m$ is the electric field loss factor. The slowly varying envelope approximation is quite valid at the wavelengths, intensities and pulse lengths relevant to the present experimental investigations. The envelope representation applied to the nonlinear polarization components given by Eq.(8) gives

$$P_1 = 2\epsilon_0 d_{eff} E_2^* E_3 e^{-j\Delta kz} \quad (16a)$$

$$P_2 = 2\epsilon_0 d_{eff} E_1^* E_3 e^{-j\Delta kz} \quad (16b)$$

$$P_3 = 2\epsilon_0 d_{eff} E_1 E_2 e^{+j\Delta kz} \quad (16c)$$

These polarization components substituted into Eq.(15) produce the coupled set of equations

$$\frac{\partial E_1}{\partial z} + \frac{n_1}{c} \frac{\partial E_1}{\partial t} + \alpha_1 E_1 = -j \frac{\omega_1 d_{eff}}{n_1 c} E_2^* E_3 e^{-j\Delta kz} \quad (17a)$$

$$\frac{\partial E_2}{\partial z} + \frac{n_2}{c} \frac{\partial E_2}{\partial t} + \alpha_2 E_2 = -j \frac{\omega_2 d_{eff}}{n_2 c} E_1^* E_3 e^{-j\Delta kz} \quad (17b)$$

$$\frac{\partial E_3}{\partial z} + \frac{n_3}{c} \frac{\partial E_3}{\partial t} + \alpha_3 E_3 = -j \frac{\omega_3 d_{eff}}{n_3 c \cos \beta} E_1 E_2 e^{+j\Delta kz} \quad (17c)$$

The experiments operate in frequency regions where crystal losses are negligible i.e. $\alpha_1 = \alpha_2 = \alpha_3 = 0$. The $\cos^2 \beta$ factor in Eq.(17c) accounts for the Poynting vector walkoff at angle β of the pump field.

An improvement in the coupled equations range of validity and a mathematical convenience occurs if one accounts for the slight crystal dispersion contained in ϵ . The frequency dependence of ϵ contained in the definition of the linear part of the polarization¹⁵ is written as

$$P_{LIN}(t,z) = \epsilon_0 \int_{-\infty}^{\infty} \chi(\omega) E(\omega,z) e^{j\omega t} d\omega \quad (18)$$

where the field is represented as

$$E(t,z) = A(t,z) e^{+j(\omega t - kz)} \quad (19)$$

The Fourier transform of Eq.(19) with a Taylor series expansion of k and χ , about the center frequency ω_0 , when substituted into Eq.(18) gives to the first order

$$P_{lin}(t,z) = \epsilon_0' \chi(\omega_0) A(t',z)$$

where

$$t' = t - (n/c)[1 + (\omega/[2\epsilon]) \frac{d\epsilon}{d\omega}] z$$

Previous Δk derivations arising from $e^{+j(\omega t - kz)}$ factors remain the same while envelope quantities now are dependent on t' rather than t . Thus the phase velocity terms $1/v_p = n/c$

are replaced by the group velocity terms

$$1/v_g = \partial k / \partial \omega = (n/c)[1 + (\omega/[2\epsilon]) \frac{d\epsilon}{d\omega}] \quad (20)$$

in Eq.(17). Group velocity considerations are primarily of interest for operation of parametric amplifiers with short pulses in the region of the tens of picoseconds.¹⁶ The group velocities for the coupled waves in the present experiments are equal to within 2% so that

$$v_{g1} = v_{g2} = v_{g3} = v_g \quad (21)$$

is a good approximation for nanosecond pulses.

The change from phase velocity to group velocity in the left side of Eq.(17) makes a reduction to ordinary differential equations possible using a transformation indicated by Scott.¹⁷ The transform equations are

$$z \rightarrow r = z \quad (22a)$$

$$t \rightarrow \tau = t - z/v_g \quad (22b)$$

$$\frac{\partial}{\partial z} \rightarrow \frac{\partial}{\partial r} - \frac{1}{v_g} \frac{\partial}{\partial \tau} \quad (22c)$$

$$\frac{\partial}{\partial t} \rightarrow \frac{\partial}{\partial \tau} \quad (22d)$$

with a resultant simplification of the coupled equations to

$$\frac{\partial E_1}{\partial r} = -j \frac{\omega_1 d_{\text{eff}}}{n_1 c} E_2^* E_3 e^{-j\Delta k r}$$

$$\frac{\partial E_2}{\partial r} = -j \frac{\omega_2 d_{\text{eff}}}{n_2 c} E_1^* E_3 e^{-j\Delta k r}$$

$$\frac{\partial E_3}{\partial r} = -j \frac{\omega_3 d_{\text{eff}}}{n_3 c \cos^2 \beta} E_1 E_2 e^{+j\Delta k r}$$

The use of $E_i = \rho_i e^{-j\phi_i}$ with $i = 1, 2$ and 3 accomplishes a rectangular to polar dependent variable conversion. The polar form equations that result are

$$\frac{\partial \rho_1}{\partial r} = - \frac{\omega_1 d_{\text{eff}}}{n_1 c} \rho_2 \rho_3 \sin \theta \quad (23a)$$

$$\frac{\partial \rho_2}{\partial r} = - \frac{\omega_2 d_{\text{eff}}}{n_2 c} \rho_1 \rho_3 \sin \theta \quad (23b)$$

$$\frac{\partial \rho_3}{\partial r} = + \frac{\omega_3 d_{\text{eff}}}{n_3 c \cos^2 \beta} \rho_1 \rho_2 \sin \theta \quad (23c)$$

$$\frac{\partial \theta}{\partial r} = \Delta k + \frac{d_{\text{eff}}}{c} \left(\frac{\omega_3}{n_3 \cos^2 \beta} \frac{\rho_1 \rho_2}{\rho_3} - \frac{\omega_2}{n_2} \frac{\rho_1 \rho_3}{\rho_2} - \frac{\omega_1}{n_1} \frac{\rho_2 \rho_3}{\rho_1} \right) \cos \theta \quad (23d)$$

where

$$\Theta = \Delta k + \phi_3 - \phi_2 - \phi_1 \quad .$$

An invariant for the parametric conversion process representing the power flow per unit area parallel to the direction of propagation is

$$W = (\epsilon_0 c/2) (n_1 \rho_1^2 + n_2 \rho_2^2 + n_3 \rho_3^2 \cos^2 \beta) \quad (24a)$$

or

$$W = I_1(0) + I_2(0) + I_3(0) \cos^2 \beta \quad . \quad (24b)$$

Introducing a set of normalized dependent and independent variables given by

$$u_1 = \left(\frac{\epsilon_0 \lambda_1 n_1}{4 \pi W} \right)^{\frac{1}{2}} \quad \rho_1 = \left[I_1 / (\omega_1 W) \right]^{\frac{1}{2}} \quad (25a)$$

$$u_2 = \left(\frac{\epsilon_0 \lambda_2 n_2}{4 \pi W} \right)^{\frac{1}{2}} \quad \rho_2 = \left[I_2 / (\omega_2 W) \right]^{\frac{1}{2}} \quad (25b)$$

$$u_3 = \left(\frac{\epsilon_0 \lambda_3 n_3 \cos^2 \beta}{4 \pi W} \right)^{\frac{1}{2}} \quad \rho_3 = \left[(I_3 \cos^2 \beta) / (\omega_3 W) \right]^{\frac{1}{2}} \quad (25c)$$

and

$$\xi = \frac{4 d_{\text{eff}} \pi (\omega W)^{\frac{1}{2}} r}{(\epsilon_0 \lambda_1 \lambda_2 \lambda_3 n_1 n_2 n_3 \cos^2 \beta)^{\frac{1}{2}}} \quad (25d)$$

where

$$\Delta S = \Delta k r / \xi \quad (25e)$$

results in the normalized coupled equations.

$$\frac{du_1}{d\xi} = -u_2 u_3 \sin \theta \quad (26a)$$

$$\frac{du_2}{d\xi} = -u_1 u_3 \sin \theta \quad (26b)$$

$$\frac{du_3}{d\xi} = +u_1 u_2 \sin \theta \quad (26c)$$

and

$$\frac{d\theta}{d\xi} = \Delta S + \left(\frac{u_1 u_2}{u_3} - \frac{u_2 u_3}{u_1} - \frac{u_1 u_3}{u_2} \right) \cos \theta \quad (26d)$$

The phase equation may also be written as

$$\frac{d\theta}{d\xi} = \Delta S + \frac{\cos \theta}{\sin \theta} \frac{d}{d\xi} [\ln(u_1 u_2 u_3)]$$

The phase equation can be integrated with a substitution from Eq.(26c) to give

$$\cos \theta = (\Gamma - \frac{1}{2} \Delta S u_3^2) / (u_1 u_2 u_3) \quad (27)$$

where

$$\Gamma = u_1(0) u_2(0) u_3(0) \cos \theta + \frac{1}{2} \Delta S u_3^2(0)$$

is a constant of integration.

Energy conservation, power conservation, and momentum conservation for the three wave interactions are given by the three auxiliary equations

$$\omega_3 = \omega_1 + \omega_2 \quad , \quad (2)$$

$$1 = \omega_1 u_1^2 + \omega_2 u_2^2 + \omega_3 u_3^2 \quad (28)$$

and

$$\Delta k = \frac{\xi}{r} \left[\frac{d\theta}{d\xi} - \left(\frac{u_1 u_2}{u_3} - \frac{u_2 u_3}{u_1} - \frac{u_1 u_3}{u_2} \right) \right] \cos \theta \quad (26d)$$

Equation (28) is a normalized version of W. The relative phase between the waves is related to momentum conservation through Δk by Eq.(26d). Additional invariants over ξ are derived by substitution of Eq.(2) into Eq.(28) giving

$$m_1 = u_1^2 + u_3^2 \quad (29a)$$

$$m_2 = u_2^2 + u_3^2 \quad (29b)$$

$$m_3 = u_1^2 - u_2^2 \quad (29c)$$

which are the Manley-Rowe¹⁸ relations.

The solution of the normalized coupled equations is based on integrating Eq.(26c) after substituting the integration constant Γ and the Manley-Rowe relations. The resultant integral is

$$\xi = \frac{1}{2} \int_{u_3^2(0)}^{u_3^2(\xi)} \frac{d(u_3^2)}{\left(u_3^2(m_2 - u_3^2)(m_1 - u_3^2) - (\Gamma - \frac{1}{2}\Delta S u_3^2)^2 \right)^{\frac{1}{2}}} \quad (30)$$

The cubic polynomial in the denominator radical suggests the use of elliptic integrals as solutions. However, several algebraic manipulations are required to produce a standard elliptic integral form. The denominator polynomial has roots that may be ordered as $u_{3c}^2 \geq u_{3b}^2 \geq u_{3a}^2 \geq 0$. Two algebraic substitutions

$$y^2 = (u_3^2 - u_{3a}^2)/(u_{3b}^2 - u_{3a}^2) \quad (31a)$$

and

$$\gamma^2 = (u_{3b}^2 - u_{3a}^2)/(u_{3c}^2 - u_{3a}^2) \quad (31b)$$

convert the integral expression to standard elliptic integrals.¹⁹

By partitioning ξ into $(\xi + \xi_0) - \xi_0$ the elliptic integral

can be written with zero lower limits as

$$\xi = \frac{1}{(u_{3c}^2 - u_{3a}^2)} \left(\int_0^{y(\xi)} \frac{dy}{[(1-y^2)(1-\gamma^2 y^2)]^{\frac{1}{2}}} - \int_0^{y(0)} \frac{dy}{[(1-y^2)(1-\gamma^2 y^2)]^{\frac{1}{2}}} \right)$$

The inverse operation of the elliptic integral is a Jacobian elliptic function. The above equation re-written with the Jacobian elliptic functions becomes

$$y(\xi) = \operatorname{sn}[(u_{3c}^2 - u_{3a}^2)^{\frac{1}{2}} (\xi + \xi_0), \gamma] \quad (32a)$$

$$y(0) = \operatorname{sn}[(u_{3c}^2 - u_{3a}^2)^{\frac{1}{2}} (\xi_0), \gamma] \quad (32b)$$

The general solution for the normalized u values is

$$u_3^2(\xi) = u_{3a}^2 + (u_{3b}^2 - u_{3a}^2) \operatorname{sn}^2[(u_{3c}^2 - u_{3a}^2)^{\frac{1}{2}} (\xi + \xi_0), \gamma] \quad (33a)$$

$$u_2^2(\xi) = [m_2 - u_3^2(\xi)] = u_2^2(0) + u_3^2(0) - u_3^2(\xi) \quad (33b)$$

$$u_1^2(\xi) = [m_1 - u_3^2(\xi)] = u_1^2(0) + u_3^2(0) - u_3^2(\xi) \quad (33c)$$

where $\xi_0 = F(\sin^{-1}[y(0)], \gamma) / (u_{3c}^2 - u_{3a}^2)^{\frac{1}{2}}$ and $F(\phi, \gamma)$ is a standard elliptic integral.

C. Special Case Solutions

In this section the solutions to the coupled equations given by Eqs. (33a, 33b and 33c) are investigated for boundary conditions appropriate to up-conversion, sum and second harmonic generation, mixing and parametric amplification. Appropriate approximations allow the elliptic functions to be reduced to circular and hyperbolic functions in the non-pump depleted regime.

The frequency up-conversion process is described by the input conditions

$$u_3^2(0) = 0 \quad (34a)$$

$$u_2^2(0) \ll u_1^2(0) \quad (34b)$$

causing
$$u_{3a}^2 = 0 \quad \text{and} \quad \Gamma = 0$$

where ω_3 is the sum frequency, ω_1 is the frequency of the highest intensity wave, and ω_2 is the lowest frequency which is up-converted. The up-conversion solutions are

$$u_3^2(\xi) = u_2^2(0) \operatorname{sn}^2[u_1(0)(\xi + \xi_0), \gamma]$$

$$u_2^2(\xi) = u_2^2(0) (1 - \operatorname{sn}^2[u_1(0)(\xi + \xi_0), \gamma])$$

$$u_1^2(\xi) = u_1^2(0) - u_2^2(0) \operatorname{sn}^2[u_1(0)(\xi + \xi_0), \gamma]$$

Equations (31) and (34) yield $\gamma^2 = u_2^2(0)/u_1^2(0) \ll 1$ making possible the approximation $\operatorname{sn}(u, \gamma) \approx \sin u$ for $\gamma^2 \ll 1$.

Since $y(0) = 0$ from Eqs.(32) and (34) and $\xi_0 = 0$, inverting the normalized variables given by Eq.(25) yields the up-conversion solutions

$$I_3(r) \approx (\omega_3/\omega_2) \frac{I_2(0)}{\cos^2 \beta} \sin^2 (r/\ell_u) \quad (35a)$$

and

$$I_2(r) \approx I_2(0) \cos^2(r/\ell_u) \quad (35b)$$

$$I_1(r) \approx I_1(0) \quad (35c)$$

where

$$1/\ell_u = u_1(0) \quad \xi/r = \frac{\pi d_{\text{eff}} [8I_1(0)]^{\frac{1}{2}}}{\epsilon_0 \lambda_2 \lambda_3 n_1 n_2 n_3 \cos^2 \beta c)^{\frac{1}{2}}}$$

For sum generation we assume the input conditions

$$u_1^2(0) = u_2^2(0) \quad (36a)$$

$$u_3^2(0) = 0 \quad (36b)$$

resulting in a denominator polynomial inside the radical for Eq.(30) of

$$u_3^2(m_1 - u_3^2)^2$$

The integration simplifies to

$$\xi = \int_{u_3(0)}^{u_3(\xi)} \frac{d u_3}{m_1 - u_3^2} = [1/u_1(0)] \tanh^{-1}[u_3(\xi)/u_1(0)]$$

with the result that

$$I_3(r) = (\omega_3/\omega_1) \frac{I_1(0)}{\cos^2 \beta} \tanh^2(r/\ell_u) \quad (37a)$$

$$I_2(r) = I_2(0) \operatorname{sech}^2(r/\ell_u) \quad (37b)$$

$$I_1(r) = I_1(0) \operatorname{sech}^2(r/\ell_u) \quad (37c)$$

with

$$I_2(0)/I_1(0) = \omega_2/\omega_1$$

Sum generation reduces to second harmonic generation if the further restrictions $\omega_2 = \omega_1$, $\omega_3 = 2\omega$ and $I_1(0) = I_2(0) = \frac{1}{2} I_\omega(0)$ are applied yielding

$$I_{2\omega}(r) = \frac{I_\omega(0)}{\cos^2 \beta} \tanh^2(r/\ell_{SH}) \quad (38a)$$

$$I_\omega(r) = I_\omega(0) \operatorname{sech}^2(r/\ell_{SH}) \quad (38b)$$

$$1/\ell_{SH} = \frac{\pi d_{eff}^2 [I_\omega(0)]^{\frac{1}{2}}}{n_1 \lambda_1 (n_1 c \epsilon_0)^{\frac{1}{2}} \cos \beta}$$

This is the familiar SHG solution which is more directly derived through an energy conservation argument.

D. Parametric Amplification

Parametric amplification of energy at ω_1 by a higher intensity at ω_3 is represented by

$$u_2^2(0) = 0 \quad (39a)$$

$$u_1^2(0) < u_3^2(0) \quad (39b)$$

with

$$u_{3a}^2 = 0, \quad u_{3b}^2 = m_2 = u_3^2(0), \quad u_{3c}^2 = m_1 = u_3^2(0) + u_1^2(0),$$

and

$$\Gamma = 0$$

Since $y(0) = 1$ from Eq.(31a), the elliptic integral becomes

$$F[\sin^{-1} y(0), \gamma] = F(\pi/2, \gamma) = K(\gamma)$$

and consequently

$$\xi_0 = K(\gamma) / [u_3^2(0) + u_1^2(0)]^{\frac{1}{2}}$$

where $K(\gamma)$ is a complete elliptic integral.¹⁹

The identity $\text{sn}[u + 2K(\gamma), \gamma] = \text{sn}(u, \gamma)$ transforms Eq.(33a) to

$$u_3^2(\xi) = u_3^2(0) \text{sn}^2[u_3(0)(\xi - \xi_0)/\gamma, \gamma] \quad (40a)$$

$$\gamma^2 = u_3^2(0) / [u_3^2(0) + u_1^2(0)] \quad (40b)$$

For convenience since β is a small angle we set $\cos^2 \beta = 1$.

The parametric amplification solutions which follow from Eqs.

(25), (33) and (40) are

$$I_1(r) = I_1(0) + (\omega_1/\omega_3) I_3(0) \left(1 - \operatorname{sn}^2 [(r - r_0)/\ell, \gamma]\right) \quad (41a)$$

$$I_2(r) = (\omega_2/\omega_3) I_3(0) \left(1 - \operatorname{sn}^2 [(r - r_0)/\ell, \gamma]\right) \quad (41b)$$

$$I_3(r) = I_3(0) \operatorname{sn}^2 [(r - r_0)/\ell, \gamma] \quad (41c)$$

where

$$1/\ell = \nu_3(0) \xi/(\gamma r) = \frac{\pi d_{\text{eff}} [8I_3(0)]^{\frac{1}{2}}}{(\epsilon_0 n_1 n_2 n_3 \lambda_1 \lambda_2 c)^{\frac{1}{2}}} \left(1 + I_1(0) \omega_3 / [I_3(0) \omega_1]\right)^{\frac{1}{2}}$$

and

$$r_0/\ell = \nu_3(0) \xi_0/\gamma = K(\gamma) = \frac{1}{2} \ell_n \left(16 \left[1 + I_3(0) \omega_1 / I_1(0) \omega_3\right]\right)$$

where Eq.(25d) and the above expression for ξ_0 with an expansion of $K(\gamma)$ using logarithm¹⁹ have been used.

For small values of ξ where pump depletion is not important and

$$u_1^2, u_2^2 \ll u_3^2 \quad (42)$$

further equation development is useful. A combination of

Eqs.(25) and (40) results in $(\omega_1/\omega_3) I_3(0) = I_1(0) \gamma^2/(1 - \gamma^2)$
which modifies Eq.(41) to

$$I_1(r) = I_1(0) + [\gamma^2/(1 - \gamma^2)] I_1(0) (1 - \text{sn}^2[(r - r_0)/\ell, \gamma]) \quad (43a)$$

$$I_2(r) = (\omega_2/\omega_1) [\gamma^2/(1 - \gamma^2)] I_1(0) (1 - \text{sn}^2[(r - r_0)/\ell, \gamma]) \quad (43b)$$

$$I_3(r) = I_3(0) \text{sn}^2[(r - r_0)/\ell, \gamma] \quad (43c)$$

Identities of Jacobian elliptic functions followed by the
approximation $\gamma^2 = 1$ permit the transformation

$$[\gamma^2/(1 - \gamma^2)] (1 - \text{sn}^2[(r - r_0)/\ell, \gamma]) = \gamma^2 \text{sn}^2(r/\ell)/\text{dn}^2(r/\ell) \\ = \sinh^2(r/\ell) .$$

The result is the familiar relations describing amplification in
the parametric approximation given by

$$I_1(r) = I_1(0) \cosh^2(r/\ell) \quad (44a)$$

$$I_2(r) = I_1(0) (\omega_1/\omega_2) \sinh^2(r/\ell) \quad (44b)$$

$$I_3(r) = I_3(0) \quad (44c)$$

This result agrees with the non-depleted pump parametric
amplification relations previously derived by Harris⁸ and Byer.¹¹

The parametric amplification case with $\Delta k \neq 0$ for the range

$$\Delta k \ell < 2 \quad (45)$$

and $u_1^2, u_2^2 < u_3^2$ is also of interest.

The denominator polynomial of Eq.(30) for $\Delta k \neq 0$ becomes

$$u_3^2(m_2 - u_3^2)(m_1 - u_3^2) - (\Delta S/2)^2 (m_2 - u_3^2)^2 .$$

Except for the change from $u_{3a}^2 = 0$ to $u_{3a}^2 = (\Delta S/2)^2$ the development proceeds in the same manner as the $\Delta k = 0$ solution. The r/ℓ in Eq.(44) becomes

$$r/\ell = \left(u_3^2(0) [\epsilon/r]^2 - [\Delta k/2]^2 \right)^{\frac{1}{2}} r .$$

Introducing the parametric gain coefficient Γ_0 defined by

$$\Gamma_0^2 = u_3^2(0) [\epsilon/r] = \frac{\pi^2 d_{\text{eff}}^2 8 I_3(0)}{\epsilon_0 \lambda_1 \lambda_2 n_1 n_2 n_3 c} \quad (46)$$

allows the solutions to be written in a previously derived form¹⁰ as

$$I_1(r) = I_1(0) \cosh^2 [\Gamma_0^2 - (\Delta k/2)^2]^{\frac{1}{2}} r \quad (47a)$$

$$I_2(r) = (\omega_2/\omega_1) I_1(0) \sinh^2 [\Gamma_0^2 - (\Delta k/2)^2]^{\frac{1}{2}} r \quad (47b)$$

$$I_3(r) = I_3(0) \quad (47c)$$

III. COMPUTER METHODS AND EXAMPLE SOLUTIONS

Evaluation of Eq.(26) was accomplished by digital calculation. A program was developed to calculate I_1 , I_2 , I_3 and θ assuming plane waves with user supplied initial values. To initialize the

program, values for crystal length, wavelengths, refractive indices, nonlinear coefficient, and walkoff angle were entered. The finite difference technique used in the computer solution provided a smooth transition between regions of no significant pump depletion and the high conversion efficiency regime. A computer solution based on the evaluation of elliptic integrals for the general analytic solution had difficulties in the region of small pump depletion as noted by Bey and Tang.²⁰

A computer calculation for a parametric amplifier with only a signal wave input, in addition to the pump, is plotted in Figs. 1a and 1b. Figure 1a represents the relative photon fluxes versus the normalized conversion length parameter $\xi = r/\ell$ with the associated relative phase plotted in Fig. 1b. These plots are solutions of Eqs.(41). The P_i values are the $u_i^2(\xi)$ values normalized by $u_3^2(0)$.

The relative signal to pump wave intensity ratio is arbitrarily chosen in a range relevant to practical parametric amplifier situations. At the optimal conversion point ξ_0 , two practical examples of the pump intensity help calibrate ξ . The value of d_{eff} used for LiNbO_3 is $5.58 \cdot 10^{-12}$ m/V ($\lambda_1 = 1550$ nm, $\lambda_2 = 3400$ nm) and for KD^*P is $5.01 \cdot 10^{-13}$ m/V ($\lambda_1 = 580$ nm, $\lambda_2 = 913$ nm). Appendix II discusses a Miller's Δ derivation of the $d_{i\ell}$ values needed to calculate d_{eff} in Eqs.(9) and (10).

A computer simulation of parametric amplification for the interesting case where both $P_1(0)$ and $P_2(0)$ inputs in addition to $P_3(0)$ are applied to the parametric medium is plotted in Fig. 2. The input ratios were arbitrarily chosen to be $P_1(0)/P_3(0) = 1.89 \cdot 10^{-3}$ and $P_2(0)/P_3(0) = 1.59 \cdot 10^{-3}$ which are near typical experimental values. Figure 2a is the magnitude of the relative photon fluxes while Fig. 2b plots the relative phase from an arbitrary initial value of $\pi/4$. A study of Eq.(26d) for various input conditions suggests a first order approximation of the phase as a linear function of ξ from the initial value $\theta(0)$ to $-\pi/2$. The value of ξ_1 , the approximate point where θ first becomes $-\pi/2$, may be estimated as

$$\xi_1 = -[\pi/2 + \theta(0)] \left. \frac{d\theta}{d\xi} \right|_{\xi=0} .$$

After the exponential conversion region the pump is depleted and the phase changes to $+\pi/2$ to begin the sum conversion process which re-generates the pump. In Fig. 1b the initial phase correction process is immediate at $\xi = 0$ since $P_2(0) = 0$ in contrast to Fig. 2b.

A second program was developed to describe the parametric interaction for Gaussian time envelope inputs for the three waves. The inputs include user supplied pulse widths, relative time offsets and energy fluence values. The assumption of equal group velocities for each field permits the inputs to be divided into time intervals

with appropriate average intensity values. These intensities become inputs for the first computer program. The sequence of outputs are summed to provide an output energy per unit area, $E(\xi)$. A result for this type of calculation as a function of ξ is shown in Fig. 3. The peak input intensities for the Gaussian envelope fields are in a ratio $\omega_3 I_1(\text{pk})/\omega_1 I_3(\text{pk}) = 1.41 \times 10^{-2}$. The result gives conversion efficiencies that are more realistic for actual pulsed parametric amplifier operation. The Q_i values are time integrated values of $u_i^2(\xi)/u_3^2(0)$. In Section IV another computer calculation is considered which also takes into account the transverse spatial variation of the input waves.

IV. PARAMETRIC AMPLIFIER EXPERIMENTS.

A. Introduction

Parametric amplifier experiments were carried out using KD^*P and LiNbO_3 crystals which provide parametric amplification over a tuning range that extends from 460 - 1400 nm and 1400-4000 nm. The KD^*P crystal was pumped with the third harmonic of a Q-switched Nd:YAG laser while the LiNbO_3 crystal was pumped directly at 1064 nm. The parametric gain, proportional to $d_{\text{eff}}^2/(\lambda_1 \lambda_2 \lambda_3)$ was of the same order for both crystals. The crystals were available in large sizes of approximately 1.5 cm diameter by 5 cm long which greatly facilitated the parametric amplifier measurements.

The parametric gain measurements utilized KD^*P crystals due to the excellent optical quality of available crystals. The LiNbO_3 OPA measurements were carried out in conjunction with a remote air pollution monitoring program which required high energy tunable

radiation in the near infrared region.^{21,22} The LiNbO_3 OPA served as a final conversion stage for a 1064 nm pumped LiNbO_3 parametric oscillator source. The experiment emphasized the overall conversion efficiency to tunable output.

B. KD^*P OPA Experiments

The KD^*P OPA measurements were conducted to verify calculated OPA gain values and the predicted angle tuning curve. Figure 4a shows a schematic of the experimental configuration used to measure parametric gain. Figure 4b shows the experimental set up which used a dye laser input to verify the KD^*P tuning characteristics. In both cases, the laser source consisted of an unstable resonator Nd:YAG oscillator/amplifier system which generated up to 700 mJ, 7 nsec 1064 μm pulses at ten pulses per second.²³

For the KD^*P gain measurements 5% of the 1064 nm beam was selected by a beam splitter and transmitted through two polarizers for variable intensity control. The beam was then transmitted through a two to one beam reducing telescope which was carefully adjusted to provide a well collimated idler (ω_2) beam incident on the KD^*P OPA crystal. The majority of the 1064 nm energy was doubled in a 2.5 cm KD^*P Type II angle phasematched crystal producing 250 mJ pulses at 532 nm. The remaining 1064 nm energy was summed with the 532 nm output in a 5.0 cm KD^*P Type II angle phasematched crystal to produce 60 mJ, 6.5 ns pulses of 355 nm energy. A prism disperser separated the wavelengths. The horizontally polarized 355 nm pumping beam was reduced in diameter and collimated by

1.7 to 1 telescope. The pump and input idler beams were combined, passed through the KD*P Type I angle phasematched parametric amplifier crystal, and separated with a prism prior to detection. Small uniform intensity regions with an area of $7.85 \times 10^{-3} \text{ cm}^2$ were selected using apertures to allow accurate measurements of the signal and idler fluences.²⁴ The corresponding input fluences for the pump and idler waves were also measured.

The gains obtained from the measurement of plane wave small area cases are compared with theory in Fig. 5. The dotted line is the intensity gain calculated using the non-depleted pump approximation given by Eq.(47). The solid line corresponds to intensity gains calculated with the input idler and pump fluences as input information for the time dependent computer calculations described in Section III. The values of the calculation, including time dependence and pump depletion, are in agreement within the experimental error of the measurements. Pump depletion becomes more significant at higher intensities consistent with the increasing separation between observed results and the non-depleted pump wave approximation.

A slightly modified experimental arrangement shown in Fig.4b was used to perform the KD*P tuning curve verification. The 532 nm energy remaining after the summing crystal was used to side pump a dye laser oscillator.²⁵ The pulsed dye laser provided an input signal wave source for the parametric amplifier. The dye laser generated 5 ns pulses of 0.2 to 0.5 mJ energy were tunable from 550 nm to 680 nm. The idler wave generated in the parametric

amplifier tuned from 1000 nm to 742 nm. The 355 nm pump beam was reduced by a 1.7 to 1 telescope before combining with the dye laser. The spatial overlap of the dye laser Gaussian mode and the unstable resonator pumping beam produced modest signal wave gains of 1.5, quite adequate for tuning curve verification.

Figure 6 shows a comparison of the calculated and measured phase matching points for KD*P. The phase matching curve was determined from a Sellmeier expression²⁶ for the n_o and n_e indices of refraction, (see Appendix II), combined with the phase matching condition given by Eq.(4). The small walk-off angle correction given by Eq.(7) was included.

Computer calculations indicate that a substantial amount of output energy should be available from a 5 cm KD*P parametric amplifier pumped with 355 nm. A 110 mJ pumping beam with an unstable resonator transverse profile and a Gaussian pulse width of 6.5 ns was modeled by a set of three concentric rings of graduated intensities. The 2 mJ dye input pulses at 580 nm with a Gaussian pulse width of 5 ns used the same ring model. The initial calculations ignored pump beam walkoff. A second calculation re-examined the energy contribution to the output from the most intense dye ring taking into account the walkoff displacement of the pumping from the signal and idler. Without walkoff calculations yielded 26.7 mJ signal wave and 15.6 mJ output at an idler wavelength of 913 nm. This is an overall conversion efficiency of 38.5%. The central dye ring contributed 17.4 mJ of the signal

and 10.3 mJ of the idler output energy. With Poynting vector walkoff included, the central dye input ring contributed 15.1 mJ of signal and 8.9 mJ of idler output energy for an efficiency of 20%.

These calculated results show that a carefully designed KD*P parametric amplifier can convert a significant fraction of the input pump energy to tunable signal and idler output energies.

C. LiNbO_3 OPA Experiments

The LiNbO_3 OPA experiments were designed to measure the OPA gain and energy conversion efficiency. Figure 7a and 7b shows a schematic of the LiNbO_3 OPA experiments with a LiNbO_3 OPO and stimulated Raman scattering input sources. The angle tuning curve for 1.064 μm pumped LiNbO_3 extends from 1400-4000 nm as shown in Fig. 8. The design and operational characteristics of the LiNbO_3 OPO are considered in detail in a recent paper.²⁷ For the present OPA measurements the LiNbO_3 OPO was tuned to an operating wavelength of 1900 nm for comparison with measurements which used the stimulated Raman converter as the input source.

The LiNbO_3 parametric oscillator operated at 56 mJ input 1064 nm energy at two times above threshold. The singly resonate parametric oscillator utilized a double passed pump beam to reduce threshold and improve the output stability. To avoid feedback into the Nd:YAG source a Faraday rotator isolator was employed prior to the 1.5 - 1 beam reducing telescope and LiNbO_3 OPO. The generated

OPO output was transmitted through a polarizer pair for variable attenuation prior to the LiNbO_3 OPA.

The LiNbO_3 OPA was pumped by 350 mJ 8 nsec 1064 nm pulses with the full 6.3 mm diameter near field unstable resonator beam. The smaller area 0.13 cm^2 OPO signal beam was incident directly into the OPA to avoid extra optical components. Thus the input beam did not utilize the full 0.30 cm^2 OPA gain region in this experiment. A dichroic beam splitter was used after the OPA to divert the residual 1064 nm pump energy prior to a power meter which measured the total signal and idler generated output energy.

Figure 9a shows the total OPA output energy available as a function of input signal wave energy for pump characteristics intensities of 52 and 69 MW/cm^2 . Figure 9 shows OPA gain saturation by plotting the total signal plus idler energy output divided by signal wave energy input versus the signal wave energy input. The 52 MW/cm^2 pump intensity provides a gain of 55, while a gain of 136 is realized for a 60 μm input in both cases. The LiNbO_3 OPO followed by a LiNbO_3 OPA provides the capability of efficiently converting input pump energy to tunable output energy in a manner that is analogous to dye oscillator/amplifier sources.

A 1900 nm signal wave source generated by stimulated Raman scattering in hydrogen gas was also used as an input to the OPA. The experimental arrangement was modified as shown in Fig. 7b by substituting a long focal length telescope and the one meter. H_2 cell for the Faraday rotator, beam reducing telescope and parametric oscillator. In this case a 6 cm long LiNbO_3 OPA crystal was

used. Available optics permitted a better transverse spatial overlap between the input Gaussian signal wave with spot size $\omega_0 = .5$ cm and the unstable resonator pump wave than in the OPO-OPA experiment. The one meter Raman cell, using fused silica windows, operated at 20 atmospheres H_2 pressure. The threshold for the first vibrational Stokes wave was 18 mJ for a 1064 nm beam focused 50 cm into the cell.

Figure 9b shows an unsaturated gain value of 140 for a 73 MW/cm^2 pump intensity. This gain value was adjusted to an equivalent gain for a 5.5 cm long OPA crystal used in the OPO experiment. The change in transverse beam overlap significantly improved the total output energy available at higher input energies since more of the available pumping beam area is now utilized.

Table I shows the measured parametric amplifier energy conversion efficiencies from the pump to signal and idler waves for various input pump energies. The measurements were done with $\lambda_1 = 1900$ nm and a pump beam area of 0.45 cm^2 . The conversion efficiency increases from 10 to 20% for pump intensities from 57.5 to 70 MW/cm^2 . The effect of the improved transverse spatial overlap between the parametric oscillator driven and the Raman cell driven parametric amplifier is evident.

The possibility of extracting additional infrared output energy and more conversion efficiency from the pump laser beam was confirmed by an experiment with two sequential parametric

amplifier crystals. The experimental configuration was similar to Fig.7a, but with the polarizers between the parametric oscillator and amplifier source removed. A 4.1 cm crystal was located after the pump beam and input beam combining beam splitter followed by a second 5.5 cm long LiNbO_3 crystal. The amplified signal plus idler energy was measured following the 1064 nm pump beam diverter. All three waves traveled directly from the first crystal to the second. The signal wavelength was chosen as 1900 nm with the idler at 2420 nm. The 8 ns pump pulses had an energy of 248 mJ/pulse with a pump beam area of 0.45 cm^2 . The measurement results are shown in Table II. The second crystal does provide an increase in conversion efficiency from 4 to 13% for the signal wave driven case. In addition, the removal of the polarizer permitted the excitation of the first LiNbO_3 crystal by both the signal and idler waves from the parametric oscillator. A comparison between the two crystal sequence excited by the signal wave only from the parametric oscillator and signal plus idler shows an increase from 32 mJ output to 43 mJ with a conversion efficiency change from 13% to 17.4%.

Figure 10 illustrates the input and output spectra for the Raman cell driven parametric amplifier. A 4.0 mJ input signal wave at 1900 nm was used. The pump energy was 262 mJ with an output signal wave energy of 23 mJ. The output linewidth is predominately controlled by the input bandwidth of 0.4 cm^{-1} with some broadening due to OPA gain saturation.

V. SUMMARY AND CONCLUSIONS

The theoretical derivations of Section II reviewed and extended the coupled wave equation analysis for parametric amplification. The connection between the solutions including pump depletion and earlier derivations assuming non-depleted pump waves was established. A practical method of generating the Jacobian elliptic pump depleted solutions with a computer program was demonstrated. As an example, the case of a parametric amplifier with ω_1 , ω_2 and ω_3 inputs where relative phase is important in the conversion process was considered. A second computer code was written which included a Gaussian pulse time dependence for the parametric amplifier inputs. This model gave more realistic conversion efficiency values. Small area gain measurements in a KD*P parametric amplifier verified the OPA theoretical calculations. The KD*P angle tuning curve for 355 nm pumping was also carefully measured. The computer calculations were extended to include beam transverse profiles which included a first order correction for pump beam Poynting vector walkoff.

Significant values of gain in a LiNbO₃ parametric amplifier of greater than 50 for both signal and idler waves from an initial signal wave input were demonstrated. The importance of the analytical derivations were underscored by the saturation behavior of the LiNbO₃ parametric amplifier which generated 50 mJ of output energy for a 4 mJ input energy with a conversion efficiency from the pump of 22.5%. Finally, additional gain and conversion efficiency was demonstrated by a two crystal parametric amplifier arrangement.

The availability of high optical quality KD^*P and LiNbO_3 nonlinear crystals and the high peak power near diffraction limited Nd:YAG pump source has led to a practical demonstration of optical parametric amplifier capability. The OPA advantages include: a wide tuning range; high gain in the forward direction only, thus avoiding the need for isolation; a relatively narrow bandwidth and narrow angle gain profile which avoids superfluorescence problems; and high conversion efficiencies in saturated gain operation for efficient power amplification. These properties make parametric amplifiers useful for amplification of dye lasers, F-center lasers, parametric oscillators and tunable outputs generated by mixing or summing processes. The advantages of parametric amplifiers which are well known in the microwave region should apply equally well in the optical region.

ACKNOWLEDGEMENTS

This work has been supported by ARO, AFOSR and NSF/RANN division. We wish to thank Mary Farley for her preparation of the manuscript.

TABLE I

ENERGY CONVERSION EFFICIENCY OF LiNbO_3 PARAMETRIC AMPLIFIER

Pump Energy	Pump Intensity	Signal Source	Input Energy	Conversion Efficiency	Total Output Energy
213 mJ	57.5 MW/cm ²	O.P.O.*	0.38 mJ	3.3%	7.0 mJ
213 mJ	57.5 MW/cm ²	O.P.O.	0.75 mJ	4.7%	10.0 mJ
213 mJ	57.5 MW/cm ²	O.P.O.	1.5 mJ	6.6%	14.0 mJ
257 mJ	69 MW/cm ²	O.P.O.	2.0 mJ	9.3%	24 mJ
226 mJ	73 MW/cm ²	Raman Cell**	3.0 mJ	19.5%	44 mJ
226 mJ	73 MW/cm ²	Raman Cell	4.25 mJ	22.6%	51 mJ

* Input Signal Area = 0.13 cm²** Input Signal Area = 0.82 cm²

TABLE II

SEQUENTIAL PARAMETRIC AMPLIFIER PERFORMANCE

Crystals at Phase- matching Angle	Input Energies from O.P.O		Signal and Idler Output After Second Crystal	Energy Conversion Efficiency
	Signal	Idler		
1 Only	2.5 mJ	0	14 mJ	4 %
2 Only	2.5 mJ	0	14 mJ	4 %
1 , 2	2.5 mJ	0	32 mJ	13 %
1 , 2	3.0 mJ	2.4 mJ	43 mJ	17.4 %

* Input Pulse Width = 5 ns

* Input Pulse Area = 0.13 cm²

APPENDIX I

CRYSTAL ACCEPTANCE ANGLE AND BANDWIDTH

The phase velocity mismatch factor is defined by

$$\Delta \vec{k} = \vec{k}_3 - \vec{k}_1 - \vec{k}_2 \quad . \quad (A.1)$$

The geometry of Fig. A.1 illustrates the momentum vectors and associated angles. Assuming small angles for ϕ and ψ and taking into account various contributions to Δk by Taylor's series expansions, the momentum mismatch expression becomes

$$\Delta k = (\omega_3/c) \left. \frac{\partial n_3(\theta)}{\partial \theta} \right|_{\theta_m} \Delta \theta + g \phi^2 - b \Delta \omega_1 \quad , \quad (A.2)$$

where

$$\frac{\partial n_3(\theta)}{\partial \theta} = n_e n_o / [n_o^2 \sin^2 \theta_m + n_e^2 \cos^2 \theta_m]^{\frac{1}{2}} \quad ,$$

$$g = k_1 k_3 / 2k_2 \quad ,$$

and

$$b = \frac{\partial k_1}{\partial \omega_1} - \frac{\partial k_2}{\partial \omega_2} \quad .$$

The first term represents an ω_3 beam acceptance angle in the horizontal plane with the ω_1 input beam at angle θ_m from the crystal optic axis. The second term is either the ω_3 beam acceptance angle in the vertical plane with fixed ω_1 or the ω_1 acceptance angle in any plane with ω_3 fixed. The final term relates Δk to broad linewidth ω_1 inputs.^{28,29}

APPENDIX II

NONLINEAR COEFFICIENT VALUES BY MILLER'S Δ SCALING

The value of $d(-\omega_3, \omega_0, \omega_0)_{ijk}$ or in condensed notation d_{il} (see BK) is estimated by utilizing Miller's Δ .³⁰ The nonlinear tensor element is related to Miller's Δ and linear susceptibilities by³¹

$$d_{ijk} = \epsilon_0 \Delta_{ijk} \chi_{ii}(\omega_1) \chi_{ii}(\omega_2) \chi_{kk}(\omega_3) \quad (A2.1)$$

where

$$\chi_{ii} = (n_o^2 - 1) \text{ at } \omega_1 \quad ;$$

$$\chi_{jj} = (n_o^2 - 1) \text{ at } \omega_2 \quad ;$$

$$\chi_{kk} = (n_e^2 - 1) \text{ at } \omega_3 \quad ;$$

and

$$\Delta_{ijk} = 1.13 \times 10^{-2} \text{ for LiNbO}_3 d_{31} \quad ,$$

$$\Delta_{ijk} = 5.99 \times 10^{-3} \text{ for LiNbO}_3 d_{22} \quad ,$$

$$\Delta_{ijk} = 4.04 \cdot 10^{-2} \text{ for KD}^*\text{P } d_{14} \quad ,$$

from Choy and Byer.³⁰

The indices of refraction for LiNbO_3 are available from previous measurements,³² while the index values for KD^*P have been

curve fit to the following Sellmeier equations²⁶ at $T = 25^{\circ}\text{C}$
for λ in μm .

$$n_o^2(\text{KD}^*\text{P}) = 1.012233 + \frac{1.23137}{1.00 - \frac{0.83818 \times 10^{-2}}{\lambda^2}} + \frac{0.2771624}{1.00 - \frac{15.00}{\lambda^2}}$$

$$n_e^2(\text{KD}^*\text{P}) = 0.933294 + \frac{1.193722}{1.00 - \frac{0.7481954 \times 10^{-2}}{\lambda^2}} + \frac{0.9423675}{1.00 - \frac{15.00}{\lambda^2}}$$

VI.

FIGURE CAPTIONS

1. Computer solutions of Eqs.(26a-d) for $P_1(0)/P_3(0) = 1.89 \times 10^{-3}$, $P_2(0) = 0$.
 - a) Plot of relative photon flux magnitudes versus ξ where $I_i = P_i W(n_3 \omega_i / n_i \omega_3)$.
 - b) Plot of the phase angle θ versus ξ .
2. Computer solutions of Eqs.(26a-d) for $P_1(0)/P_3(0) = 1.89 \times 10^{-3}$, $P_2(0)/P_3(0) = 1.59 \times 10^{-3}$.
 - a) Plot of relative photon flux magnitudes versus ξ where $I_i = P_i W(n_3 \omega_i / n_i \omega_3)$.
 - b) Plot of the phase angle θ versus ξ starting at an initial phase of $+45^\circ$.
3. Time dependent computer solutions for $\tau_1 = \tau_2 = 0.75 \tau_3$, $Q_1(0)/Q_3(0) = 1.41 \times 10^{-2}$, $Q_2(0) = 0$ where the Q values are the time integrated values of $u_i^2(\xi)/u_3^2(0)$. The output fluence is $E_i(\xi) = Q_i W(n_3 \omega_i / n_i \omega_3)$.
4. Experimental configurations for the KD*P OPA investigations.
 - a) Set up for the measurement of small area KD*P OPA gain.
 - b) Set up for the KD*P tuning curve verification.
5. Signal (ω_1) and idler (ω_2) intensity gains vs pump intensity for a KD*P OPA pumped at 354 nm. The estimate is the parametric approximation given by Eq.(47). The calculation is based on the time dependent solutions of Eq.(26).

FIGURE CAPTIONS - cont.

6. Angle tuning curve for a KD^*P OPA Type I phasematched with 355 nm pump at $T = 25^\circ\text{C}$. The solid curve represents a computer calculation by Herbst.²⁶ The input signal wavelengths are shown by the lines and the observed output idler wavelengths by the solid dots.
7. Schematic of the LiNbO_3 OPA experimental configurations
 - a) LiNbO_3 singly resonate OPO source
 - b) A 1064 nm pumped H_2 stimulated Raman source at $\lambda_1 = 1910$ nm.
8. Angle tuning curve for the LiNbO_3 OPA pumped at 1064 nm at $T = 25^\circ\text{C}$.
9.
 - a) LiNbO_3 OPA energy output vs input signal energy for the OPO and stimulated Raman 1900 nm sources.
 - b) LiNbO_3 OPA energy ratio vs input signal energy for the LiNbO_3 OPO and stimulated Raman source inputs.
10.
 - a) 4 mJ, 5 nsec input spectrum at 1910 nm to the LiNbO_3 OPA generated by stimulated Raman scattering in H_2 pumped by 1064 nm
 - b) LiNbO_3 OPA output spectrum at 23 mJ output energy.
- A1. \underline{k} -vector diagram showing phasematching angle θ_m and signal (\underline{k}_1) and idler (\underline{k}_2) angles with respect to the pump (\underline{k}_3) vector.

VII.

REFERENCES

1. P.A. Franken, A.E. Hill, C.W. Peters and G. Weinreich, "Generation of Optical Harmonics", Phys. Rev. Letts. 7, p.118-119 (1961).
2. C.C. Wang and G.W. Racette, "Measurement of Parametric Gain Accompanying Optical Difference Frequency Generation", Appl. Phys. Letts. 6, 169-171 (1965).
3. R.H. Kingston, "Parametric Amplification and Oscillation at Optical Frequencies", Proc. I.R.E. 50, 472 (1962).
4. N.M. Kroll, "Parametric Amplification in Spatially Extended Media and the Application to the Design of Tunable Oscillators at Optical Frequencies", Phys. Rev. 127, 1207-1211 (1962).
5. S.A. Akhmanov and R.V. Khokhlov, "Concerning One Possibility of Amplification of Light Waves", Sov. Phys. JETP, 16, 252-257 (1963).
6. J.A. Armstrong, N. Bloembergen, J. Ducuing, P.S. Pershan, "Interaction Between Light Waves in a Nonlinear Dielectric", Phys. Rev. 127, 1918-1939 (1962).
7. J.A. Giordmaine and R.C. Miller, "Tunable Coherent Parametric Oscillation in LiNbO_3 at Optical Frequencies", Phys. Rev. Letts. 14, 973-976 (1965).

8. S.F. Harris, "Tunable Optical Parametric Oscillators",
Proc. IEEE, 57, 2096-2113 1969.
9. R.G. Smith, "Optical Parametric Oscillators", vol. 4 of
Advances in Lasers, ed. by A.K. Levine and A.J. DeMaria,
Dekker, New York.
10. R.L. Byer, "Optical Parametric Oscillators", Treatise in
Quantum Electronics, vol. 1, part B, ed. by H. Rabin and
C.L. Tang, Academic Press, New York, 1975, pg.587-702.
11. G.D. Boyd and D.A. Kleinman, "Parametric Interaction of
Focused Gaussian Light Beams", J. Appl. Phys. 39, 3597-3639
1968.
12. S.F. Harris, Lecture Notes for Nonlinear Optics Course
at Stanford University, unpublished.
13. D.A. Kleinman, "Nonlinear Dielectric Polarization in
Optical Media", Phys. Rev. 126, 1977-1979 1962.
14. F. Zernike and J.F. Midwinter, Applied Nonlinear Optics,
John Wiley and Sons, New York, p.61-67, 1973.
15. J.A. Armstrong, Sudhanshu S. Jha and N.S. Shiren, "Some
Effects of Group Velocity Dispersion on Parametric
Interactions", IEEE Journ. of Quant. Elect. QE.6, 123-129
1970.

16. M.F. Becker, D.J. Kuizenga, D.W. Phillion and A.E. Siegman, "Analytic Expressions for Ultrashort Pulse Generation in Mode Locked Optical Parametric Oscillators", Journ. of Appl. Phys. 45, 3996-4005 1974.
17. A.W. Scott, Active and Nonlinear Wave Propagation in Electronics, New York, Wiley-Interscience, p.202, 1970.
18. J.M. Manley and H.E. Rowe, "Some General Properties of Nonlinear Elements I General Energy Relations", Proc. IRI, 44, 904-913 (July 1956).
19. P.F. Byrd and M.D. Friedman, Handbook of Elliptic Integrals for Engineers and Scientists, 2nd Edition, Springer-Verlag, New York, 1971.
20. P.P. Bey and C.L. Tang, "Plane Wave Theory of Parametric Oscillator and Coupled Oscillator-Up-converter, IEEE Journ. of Quantum Electronics, QE-8, 361-369 1972.
21. R.A. Baumgartner and R.L. Byer, "Remote SO₂ Measurements at 4 μ m with a Continuously Tunable Source", Optics Letts. 2, 163-165 1978.
22. R.A. Baumgartner and R.L. Byer, "A Continuously Tunable Infrared Lidar with Applications to Remote Measurements of SO₂ and CH₄", Applied Optics, vol.17, p.3555-3561 (Nov.1978).

23. R.L. Herbst, H. Komine and R.L. Byer, "A 200 mJ Unstable Resonator Nd:YAG Oscillator", Optics Commun. 21, 5-7, 1977.
24. J.E. Bjorkholm, "Some Effects of Spatially Non-uniform Pumping in Pulsed Optical Parametric Oscillators", IEEE Journ. Quant. Elect. QE-7, 109-118, 1971.
25. R.L. Byer and R.L. Herbst, "The Unstable Resonator YAG", Laser Focus, vol. 14, p.48-57, (1978).
26. R.L. Herbst, private communication.
27. S. Brosnan and R.L. Byer, "Linewidth and Threshold Studies of a LiNbO_3 Optical Parametric Oscillator (to be published).
28. R.L. Byer, "Parametric Fluorescence and Optical Parametric Amplification", Stanford University Thesis, Microwave Laboratory Report 1711, 5-12 (1968).
29. R.L. Byer, "Parametric Oscillators", in Laser Spectroscopy ed. by R.G. Brewer and A. Mooradian, Plenum, New York, 90-94, (1973).
30. R.C. Miller, "Optical Second Harmonic Generation in Pyroelectric Crystals", Appl. Phys. Letts. 5, 17-19, 1964.
31. M.M. Choy and R.L. Byer, "Accurate Second Order Susceptibility Measurements of Visible and Infrared Nonlinear Crystals", Phys. Rev. B, 14, 1693-1706 (1976).

32. M.V. Hobden and J. Warner, "The Temperature Dependence of the Refractive Indices of Pure LiNbO_3 ", Phys. Letts. 22, 243-244 (1966).

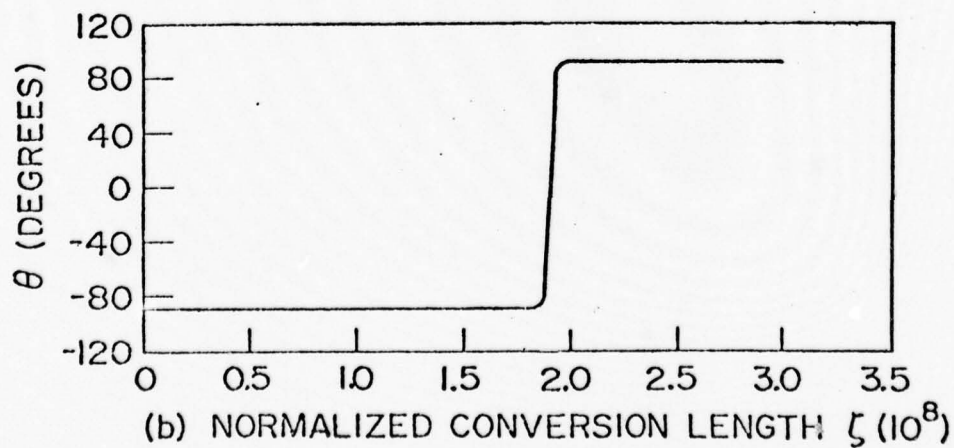
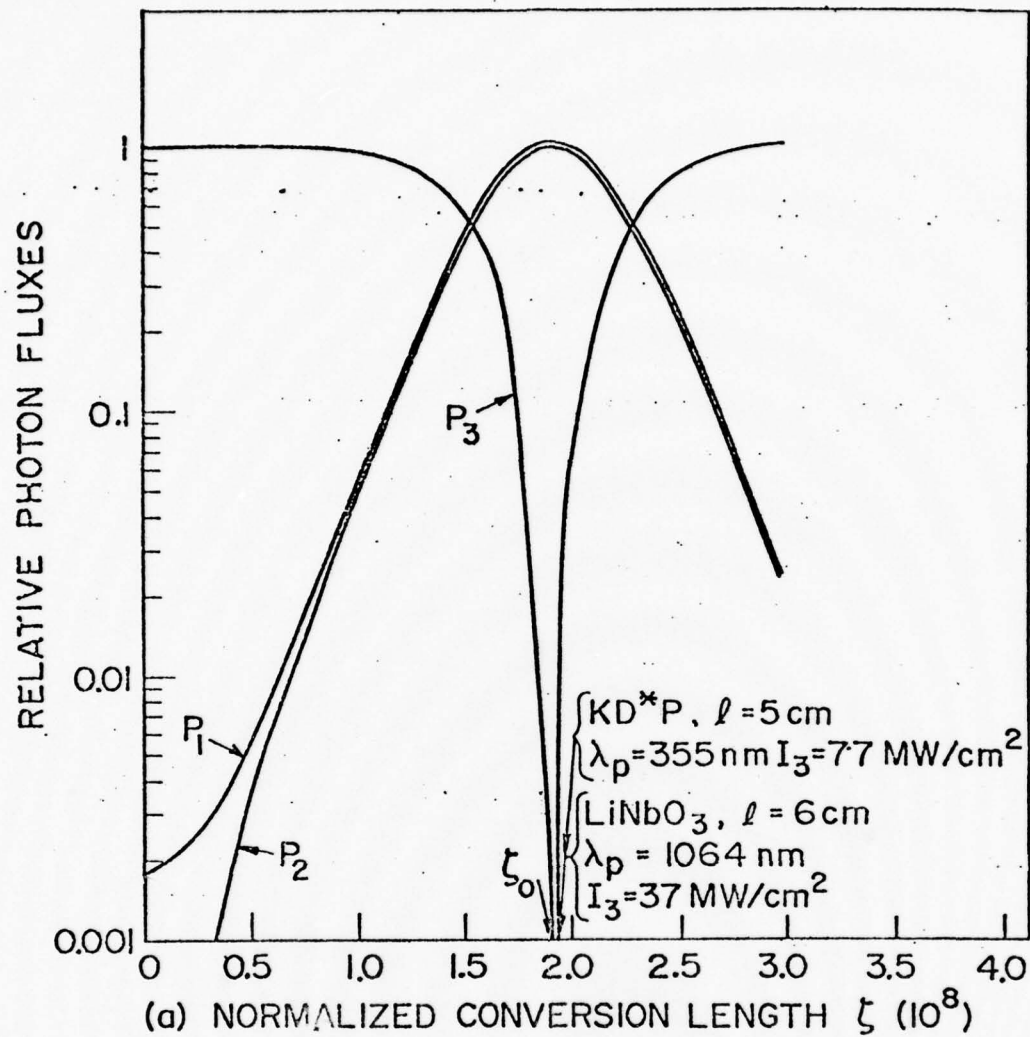
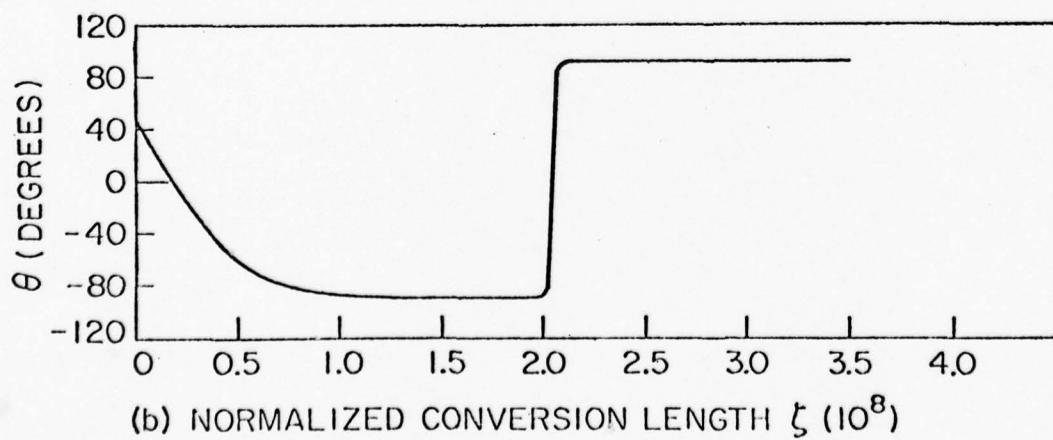
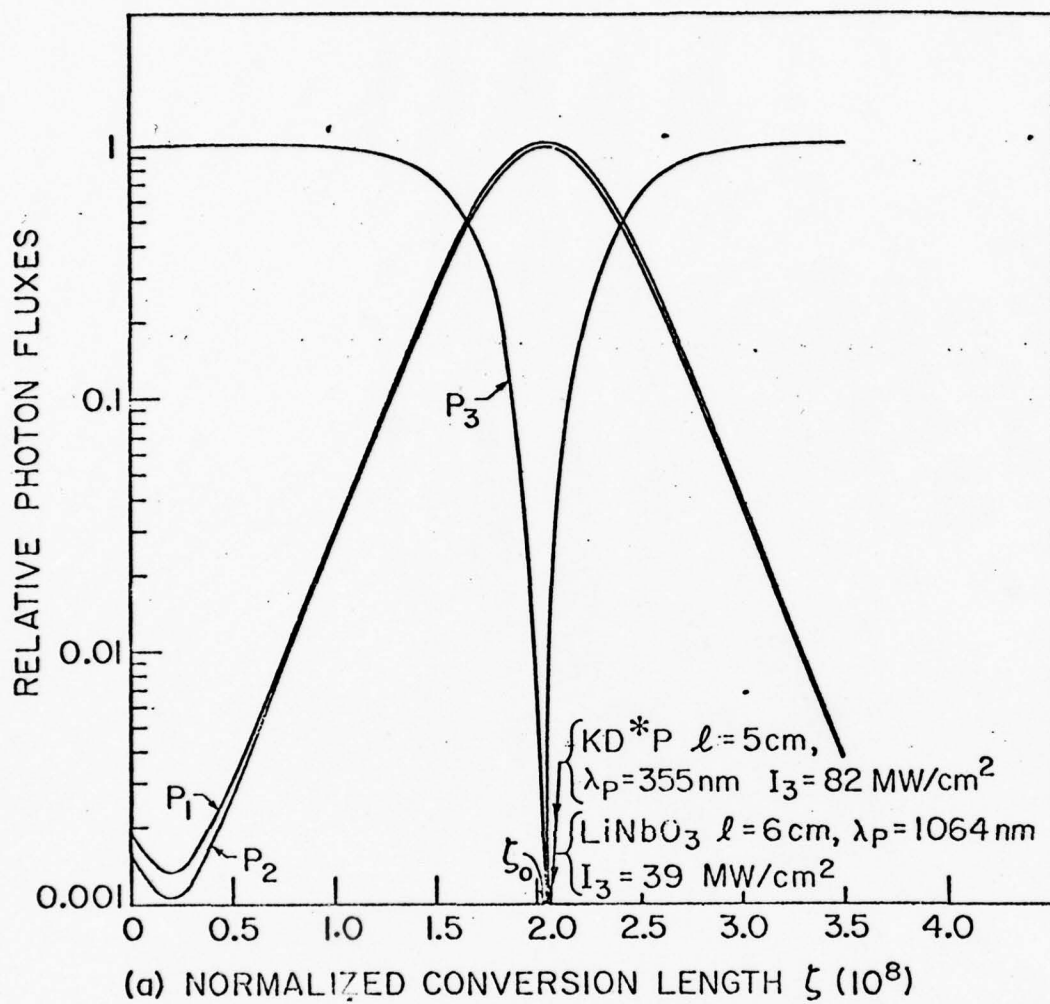


Fig 1a, 1b



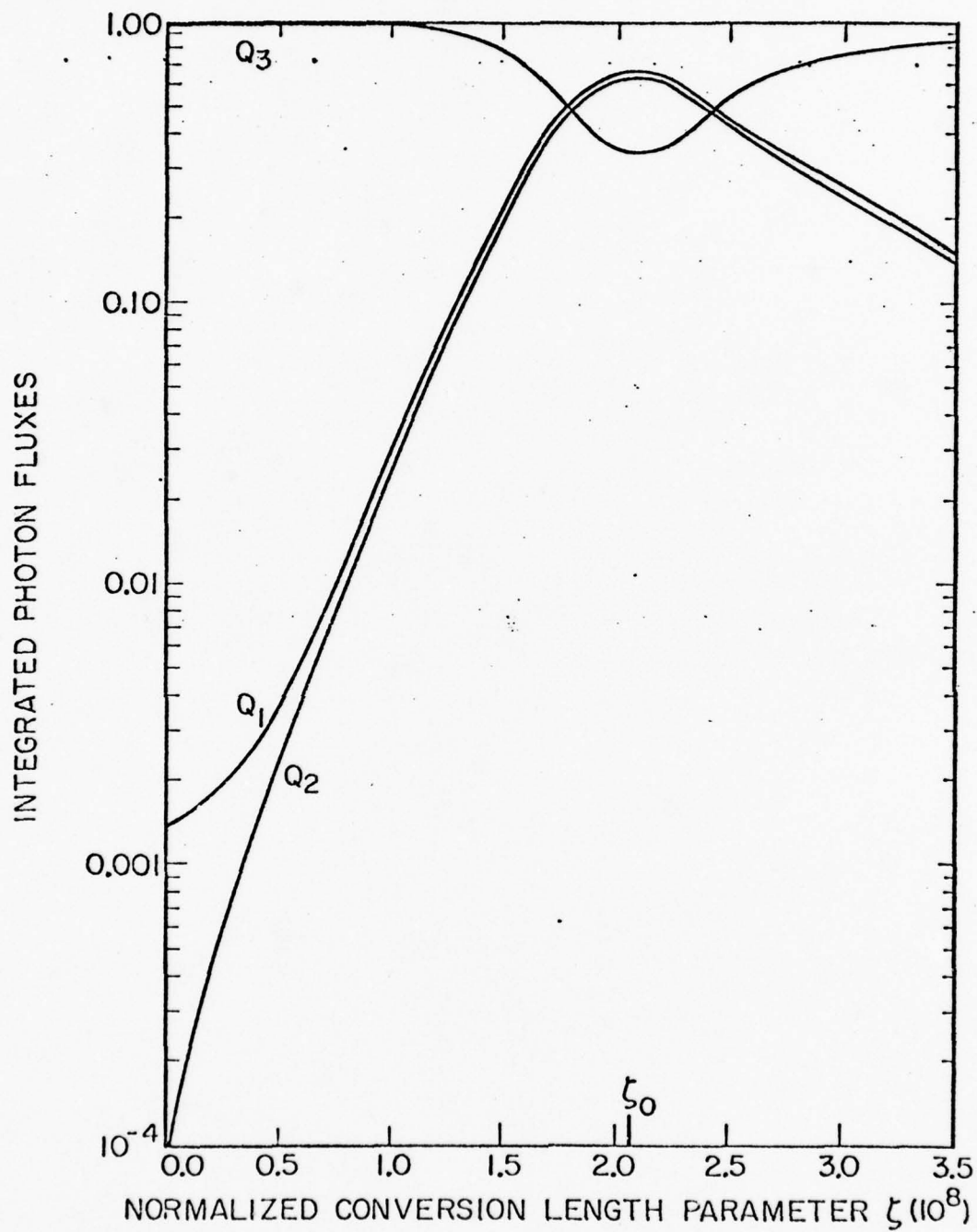
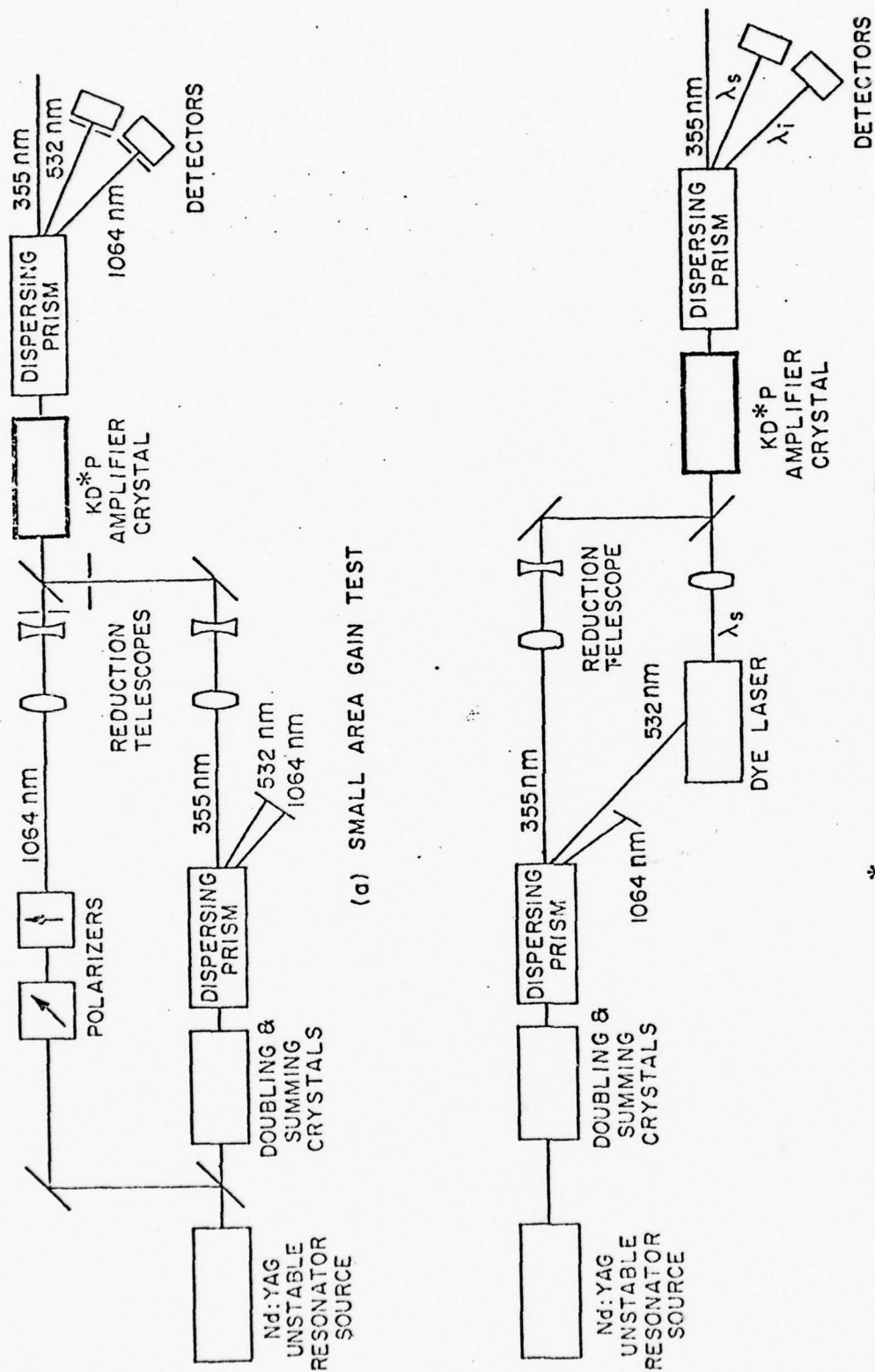
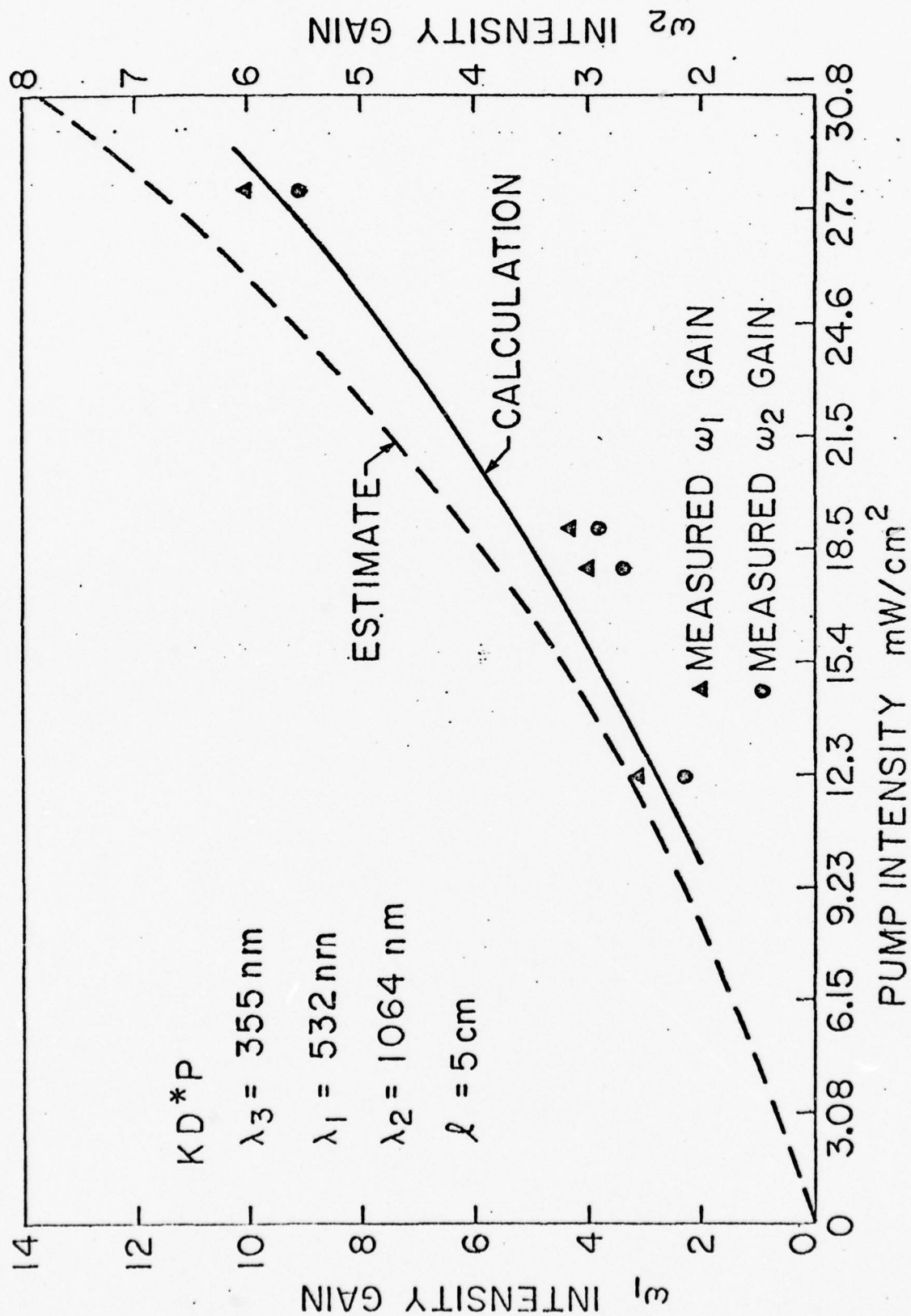


Fig 3



(b) KD*P TUNING CURVE MEASUREMENT



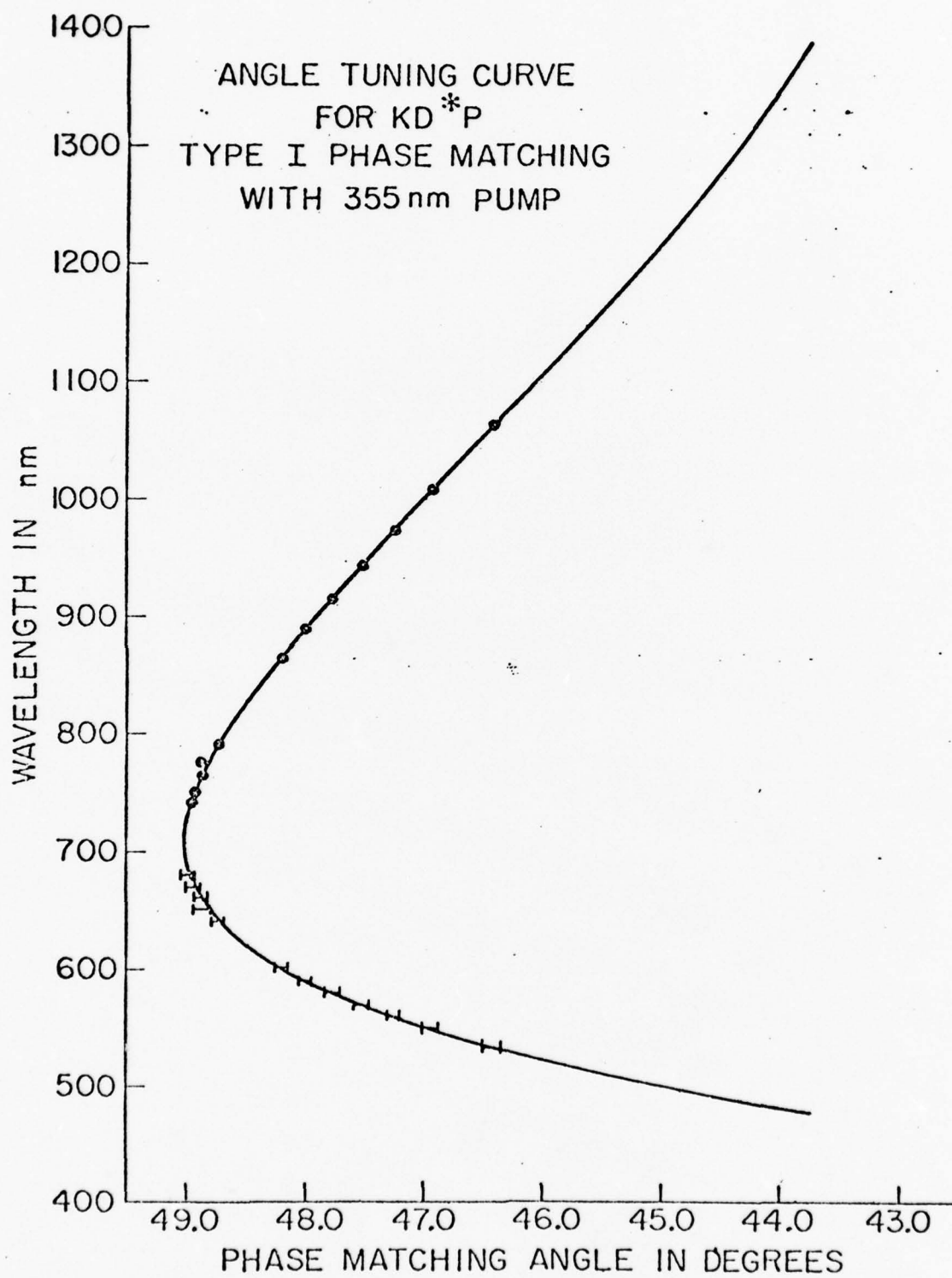
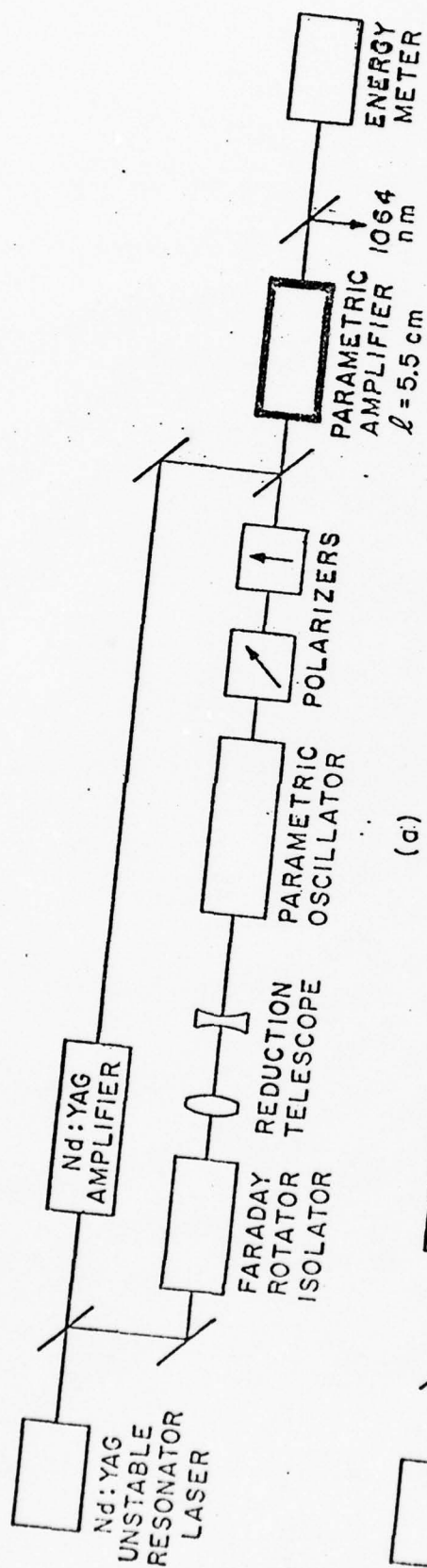
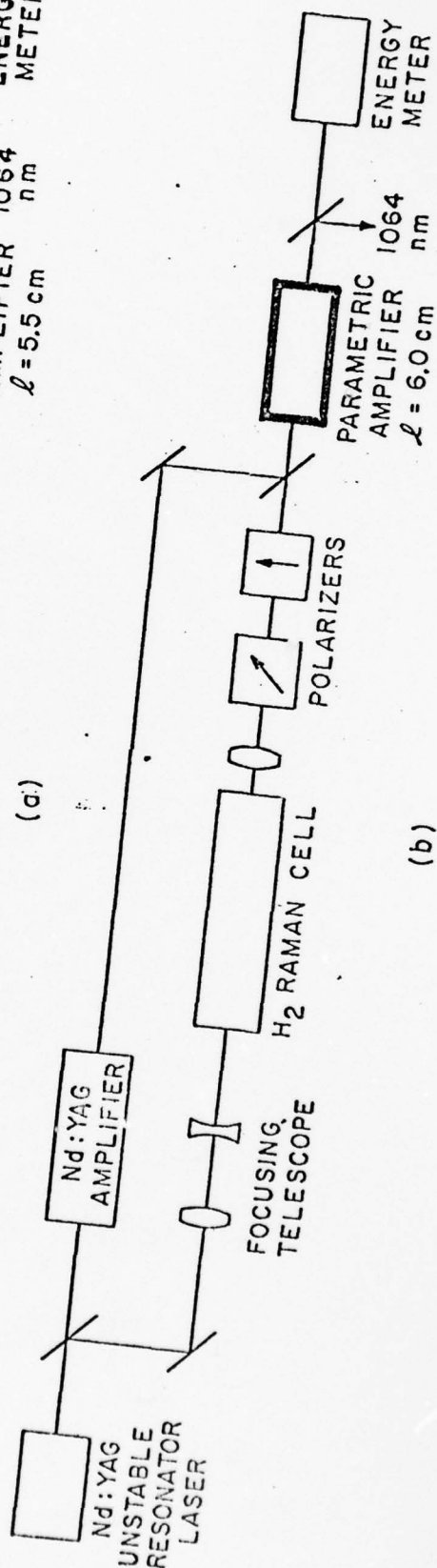


Fig 6

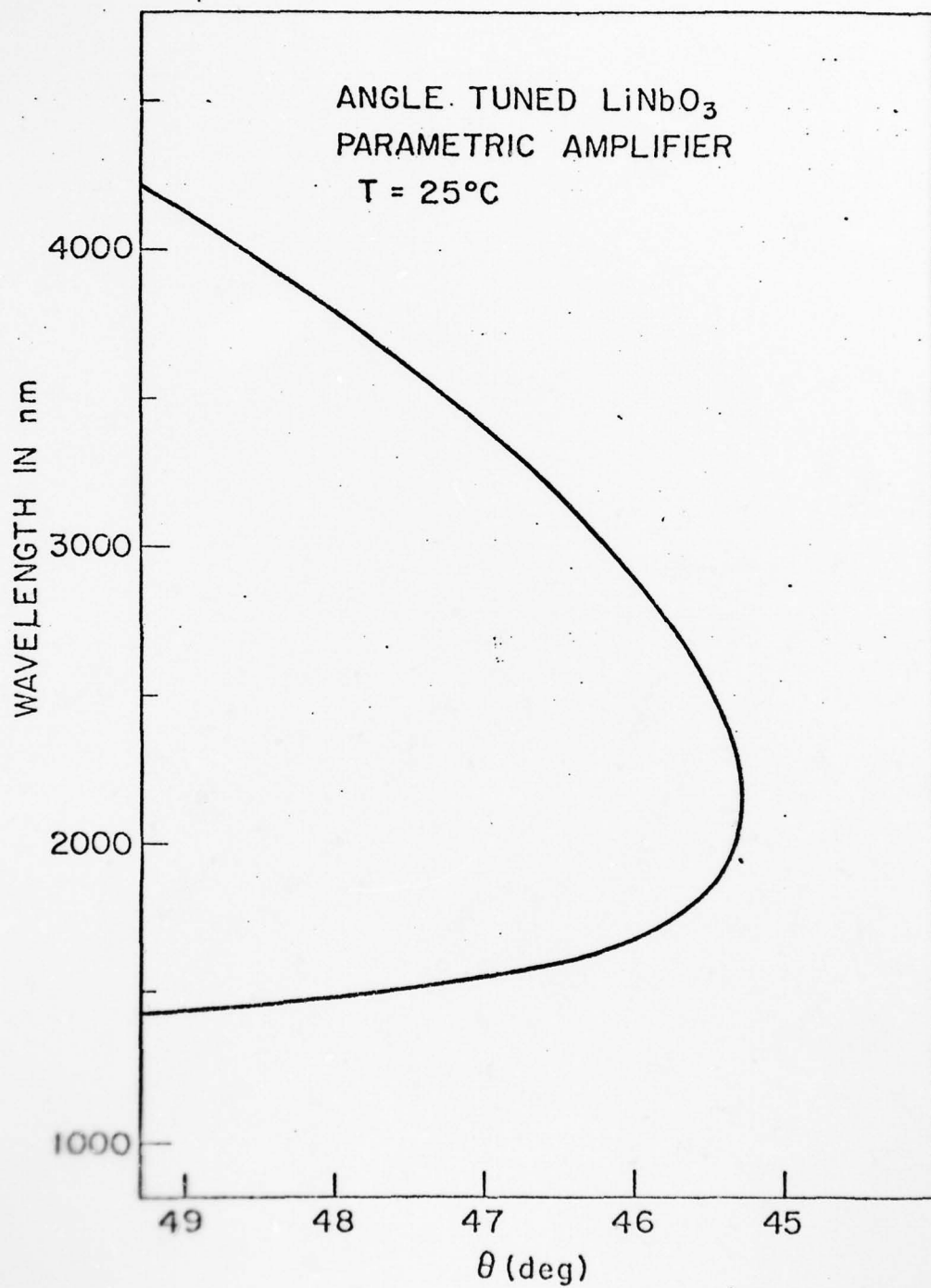


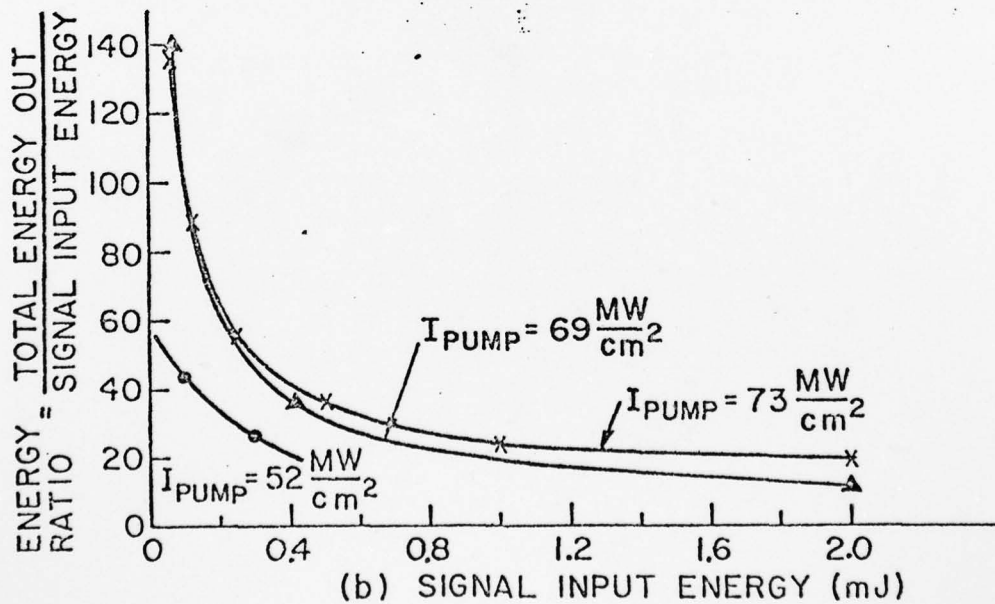
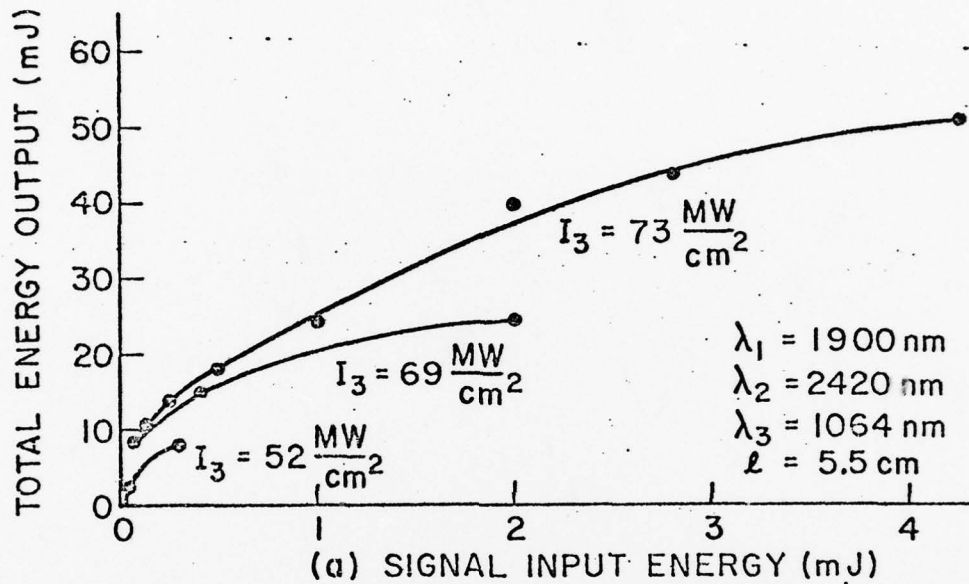
(a)

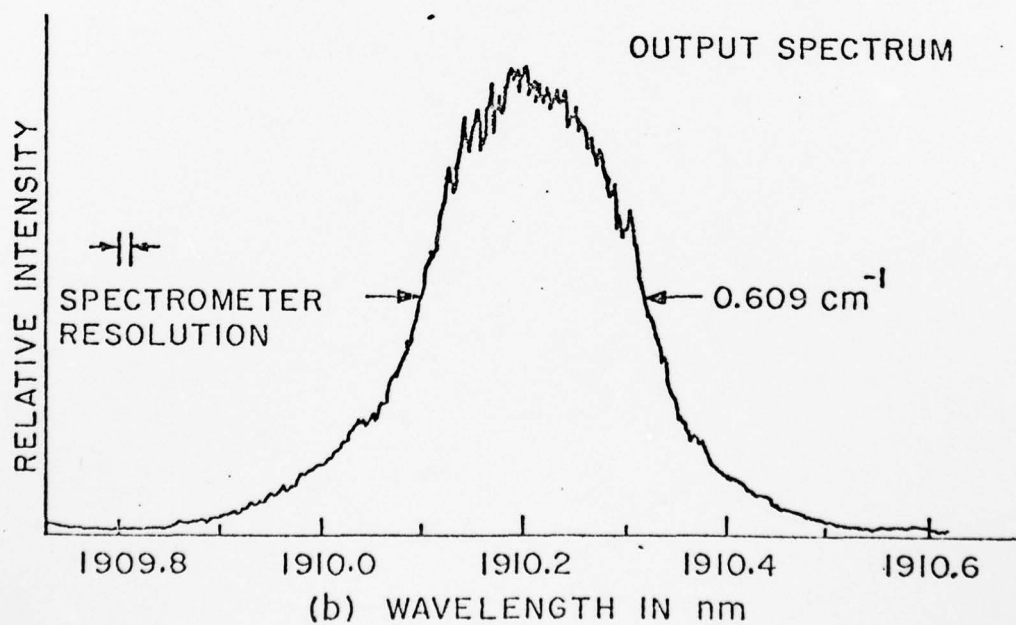
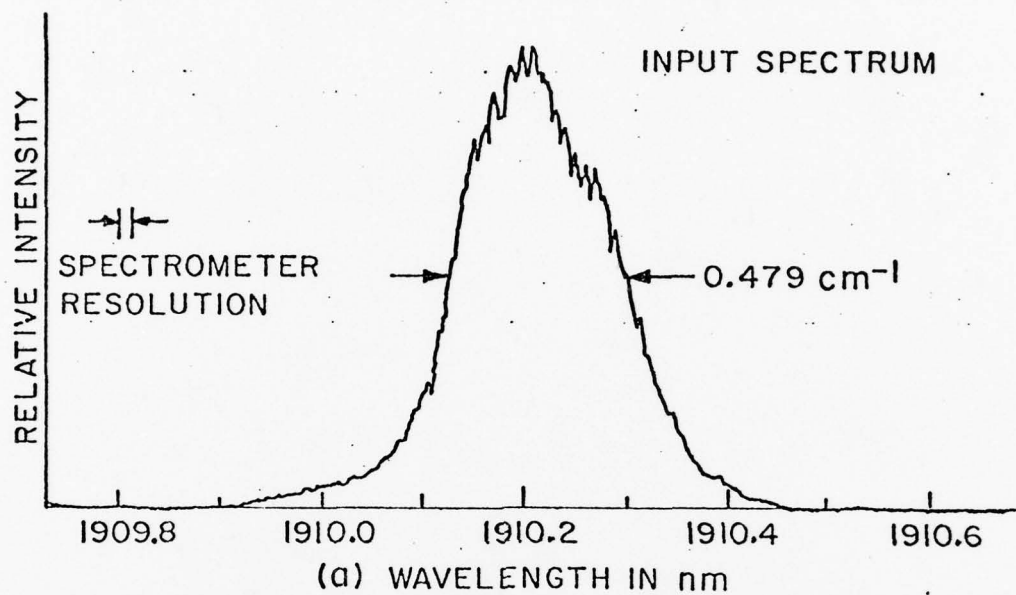


(b)

Fig 7







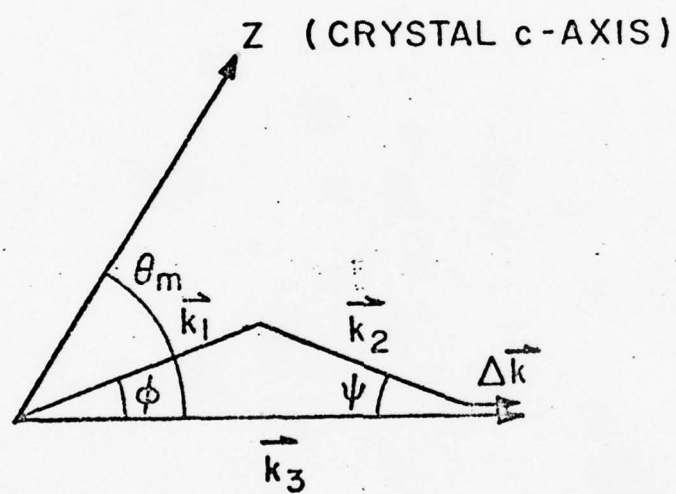


Fig A1

APPENDIX III

S. J. Brosnan and R. L. Byer, " Optical Parametric
Oscillator Threshold and Linewidth Studies.

OPTICAL PARAMETRIC OSCILLATOR
THRESHOLD AND LINEWIDTH STUDIES

S.J. Brosnan and R.L. Byer
Applied Physics Department

ABSTRACT

This paper presents a detailed study of the optimum design parameters for the LiNbO_3 parametric oscillator. Theoretical and experimental studies of the OPO threshold parameters and of linewidth control are presented. Consideration is given to practical factors that limit OPO performance such as laser beam quality and crystal damage mechanisms. In addition, stable single axial mode operation is reported.

OPTICAL PARAMETRIC OSCILLATOR THRESHOLD AND LINEWIDTH STUDIES

I. INTRODUCTION

The optical parametric oscillator (OPO) has been extensively studied and developed since Giordmaine and Miller first demonstrated parametric oscillation in LiNbO_3 in 1965.¹ Following early rapid progress reviewed by Harris in 1969,² work in parametric oscillators has proceeded at a more deliberate pace as summarized in more recent reviews by Byer³ and by Smith.⁴

The development of large, good quality LiNbO_3 crystals⁵ led to the demonstration of the Nd:YAG laser pumped 1.4 - 4.0 μm angle tuned LiNbO_3 OPO by Herbst et. al.,⁶ in 1974. The early results were soon extended to higher output energies and narrower linewidths by Byer et. al.⁷ These improvements led to the application of the LiNbO_3 OPO source in remote air pollution sensing,^{8,9} laser induced chemistry,¹⁰ and laser isotope separation studies.¹¹

To date there has been no detailed study of the optimum design parameters for the LiNbO_3 OPO tunable source. This paper fills that gap by presenting theoretical and experimental studies of the OPO threshold dependencies and linewidth control. Consideration is also given to practical factors that limit the OPO performance such as laser beam mode quality and crystal damage mechanisms and limits.

A model for describing the time dependent OPO threshold pump fluence is introduced in Section II. The model and computer simulated results are compared with detailed experimental measurements of LiNbO_3 OPO threshold as a function of important parameters such as pump pulse width, cavity length, output coupling and pump spatial mode parameters. The LiNbO_3 OPO operating limits and pump laser requirements are determined by crystal damage. We, therefore, present results of damage studies in Section III. In Section IV a model describing the LiNbO_3 OPO linewidth is presented. The model considers the effects of a grating, beam expander and etalons within the OPO cavity. Using a grating with two etalons we have successfully demonstrated stable single axial mode operation of the LiNbO_3 OPO.

The theory of parametric oscillation requires an understanding of the parametric amplification process in a nonlinear medium. In an accompanying paper Baumgartner and Byer¹² have treated optical parametric amplification (OPA) in detail. We refer to the OPA results in our theoretical treatment of the optical parametric oscillator.

II. OPO THRESHOLD

A. Theory

In this section a model is developed describing the threshold pump intensity of a pulsed singly resonant oscillator (SRO) including the effects of Poynting vector walkoff. Simplified expressions for OPO threshold are derived for the cases of a

simple SRO and also for the double pass pumped version (DSRO).

A schematic of the simple oscillator is shown in Fig. 1. A more complicated resonator, which includes line narrowing elements, is easily treated in this model by generalizing the definition of reflective cavity loss R to include all cavity discrete losses. The tuning curve of the LiNbO_3 OPO is shown in Fig. 2.

Consider a parametric oscillator with a plane-parallel two mirror cavity. Such a configuration in a laser is unstable. Here, however, the Gaussian gain profile generated by the Gaussian pump quickly confines the resonated signal wave and stabilizes the cavity.¹³ A discussion of this effect and a method for calculating signal spot size are given in Appendix A.

In the slowly varying envelope approximation the equations describing the collinear OPO fields in terms of complex phasor amplitudes, assuming no pump depletion, are given by

$$\begin{aligned} \frac{dE_s}{dz} + \alpha_s E_s &= j \kappa_s E_p E_i^* e^{j\Delta k z} \\ \frac{dE_i}{dz} + \alpha_i E_i &= j \kappa_i E_p E_s^* e^{i\Delta k z} \end{aligned} \quad (1a)$$

where the α 's are field absorption coefficients, z is the spatial coordinate in the propagation direction and $\Delta k = k_p - k_s - k_i$ defines wavevector mismatch. The interaction coefficients κ_m are defined by the following equation,

$$\kappa_m = \frac{\omega_m d_{\text{eff}}}{n_m c} \quad m = s, i \quad (2)$$

where d_{eff} is the effective nonlinear coefficient and n_m is the refractive index of the nonlinear crystal at angular frequency ω_m for the signal or idler wave.

In Eq.(1) the signal and idler fields are driven by the polarization waves possessing a spatial profile determined by the product of two field profiles. We assume that the idler wave is not resonated and is free to accept the profile of its driving polarization. The signal wave, however, is resonated. Its driving polarization must be expanded in cavity eigen modes to find the fraction of generated signal field which is coupled into the TEM_{00} mode of the resonator. Coupling coefficients of this type have been calculated by Kogelnik¹⁴ and applied to OPO's by Boyd et.al.¹⁵ and Asby.¹⁶ Here, however, it is convenient to include the pump Poynting vector walkoff into the coupling coefficients for both the signal and idler waves. These coefficients and a solution to the coupled equations for the case $\alpha_s = \alpha_i = \alpha$ and $\Delta k = 0$ are given in Appendix B.

The idler field is assumed to be zero at the entrance to the crystal. The signal field at the end of a crystal of length l is given by

$$E_s(l) = E_s(0) e^{-\alpha l} \cosh \Gamma l \quad (3)$$

Fig 4

where

$$\Gamma = \sqrt{\kappa_s \kappa_i g_s |E_p|^2} \quad (4)$$

is the parametric gain coefficient.

Here g_s is the signal spatial mode coupling coefficient defined in Appendix B by

$$g_s = \frac{w_p^2}{w_p^2 + w_s^2}$$

where w_p and w_s are the Gaussian mode electric field radii.

An effective parametric gain length \mathcal{L} is introduced where

$$\mathcal{L} = \ell_w \operatorname{erf} \left(\frac{\sqrt{\pi}}{2} \frac{\ell}{\ell_w} \right) \quad (5)$$

The walkoff length ℓ_w is given by

$$\ell_w = \frac{\sqrt{\pi}}{2} \frac{w_p}{\rho} \sqrt{\frac{w_p^2 + w_s^2}{w_p^2 + w_s^2/2}} \quad (6)$$

where p is the double refraction walkoff angle. The walkoff length is closely related to the aperture length previously introduced by Boyd et.al.¹⁵ For large arguments the error function approaches unity. Therefore, the walkoff length ℓ_w is the effective gain length for an infinitely long crystal.

The single pass signal power gain from Eq.(3) becomes

$$\frac{|E_s(l)|^2}{|E_s(0)|^2} = e^{-2\alpha l} \cosh^2 \Gamma \mathcal{L} \quad (7)$$

For pulsed OPO operation, the buildup to threshold may be calculated by assuming a Gaussian time profile for the incident pump intensity which yields a time dependent gain coefficient Γ described by

$$\Gamma = \Gamma_0 e^{-(t/\tau)^2} \quad (8)$$

where τ is the $1/e^2$ intensity halfwidth of the pump pulse. The generated signal wave is amplified as it makes m cavity transits from an initial parametric noise power.¹⁷ During a single cavity transit the pump intensity is assumed to be constant, or equivalently, $\tau \gg c/n_p l$. For pass m , the signal power is from Eq.(7),

$$P_m = P_{m-1} \left[R e^{-4\alpha l} \cosh^2 [\Gamma_0 e^{-(t_m/\tau)^2} \mathcal{L}] \right] \quad (9)$$

The factor in brackets is the instantaneous cavity net gain. Equation (9) can be easily iterated numerically to compute threshold, incrementing pump intensity until a defined threshold is reached. For the calculations presented here, threshold is defined as a signal energy of 100 μJ , giving a threshold power to noise power ratio of $\ln(P_m/P_0) = 33$. It is shown in the next

section that this numerical model is in excellent agreement with experiment.

A simpler model is desirable, however, for optimizing the OPO parameters that affect threshold. To allow iterative calculations we introduce a time independent gain profile of width $\bar{\tau}$ and magnitude $\bar{\Gamma}$. The width is determined by the time over which the parametric oscillator has net instantaneous gain greater than unity. From Eq.(9) we find that

$$\bar{\tau} = 2\tau \left\{ \ln \left[\frac{\Gamma_o \mathcal{L}}{\ln \left(\frac{1}{\sqrt{R}} + \sqrt{\frac{1}{R} - 1} \right)} \right] \right\}^{\frac{1}{2}} \quad (10)$$

where the relation $\cosh^{-1} x = \ln(x + \sqrt{x^2 - 1})$ has been used.

Next, we relate the square pulse height $\bar{\Gamma}$ to the Gaussian peak Γ . For consistency the total gain of the square pulse must equal the total gain of the Gaussian case, or

$$\begin{aligned} \frac{c\bar{\tau}}{2L} \ln \cosh^2 \bar{\Gamma} \mathcal{L} &= \ln \left| \Pi_q \cosh^2 [\Gamma_o \mathcal{L} e^{-(t_q/\tau)^2}] \right| \\ &= \sum_q \ln \cosh^2 [\Gamma_o \mathcal{L} e^{-(t_q/\tau)^2}] \end{aligned} \quad (11)$$

Fig 7

- 76 -

Nd:YAG
UNSTABLE
RESONATOR
LASERNd:YAG
UNSTABLE
RESONATOR
LASER

For $\tau \gg 2L/c$, this summation may be approximated by an integral. If in addition the hyperbolic functions are approximated by exponentials, we obtain

$$\bar{\Gamma} \mathcal{L} = \Gamma_0 \mathcal{L} \frac{\sqrt{\pi}}{2} \left[\frac{\text{erf}(\bar{\tau}/2\tau)}{\bar{\tau}/2\tau} \right] \quad (12)$$

Let threshold be reached after the p 'th round trip, where $p = c\bar{\tau}/2L$ with the optical cavity length L given by

$$L = L' + (n-1) \ell \quad (13)$$

Here L' and ℓ are the cavity and crystal physical lengths. Rewriting Eq.(9) in the form

$$\ln(P_n/P_0) = p \ln R - 4 p \alpha \ell + 2 p \ln \cosh \bar{\Gamma} \mathcal{L}$$

and making the exponential approximation that $\cosh \alpha = \frac{1}{2} \exp 2\alpha$ we find

$$\bar{\Gamma} \mathcal{L} = L/c\bar{\tau} \ln P_n/P_0 + 2\alpha \ell + \ln(1/\sqrt{R}) + \ln 2 \quad (14)$$

This equation has the clear physical interpretation of a gain equals loss threshold condition. The first term is an effective loss due to the buildup time during pulsed operation. The following terms describe distributed crystal absorption losses and the cavity output coupling loss. The final term $\ln 2$ is due to the SRO operation.

Substituting Eq.(14) into Eq.(12) we have finally

$$\Gamma_0 \mathcal{L} = 2/\sqrt{\pi} \left[\frac{\bar{\tau}/2\tau}{\text{erf}(\bar{\tau}/2\tau)} \right] \left[L/c\bar{\tau} \ln(P_n/P_0) + 2\alpha \ell + \ln(1/\sqrt{R}) + \ln 2 \right] \quad (15)$$

AD-A072 009

STANFORD UNIV CALIF EDWARD L GINZTON LAB
LASER PHYSICS AND LASER TECHNIQUES.(U)
APR 79 A E SIEGMAN, R L BYER

F/6 20/5

UNCLASSIFIED

GL-2953

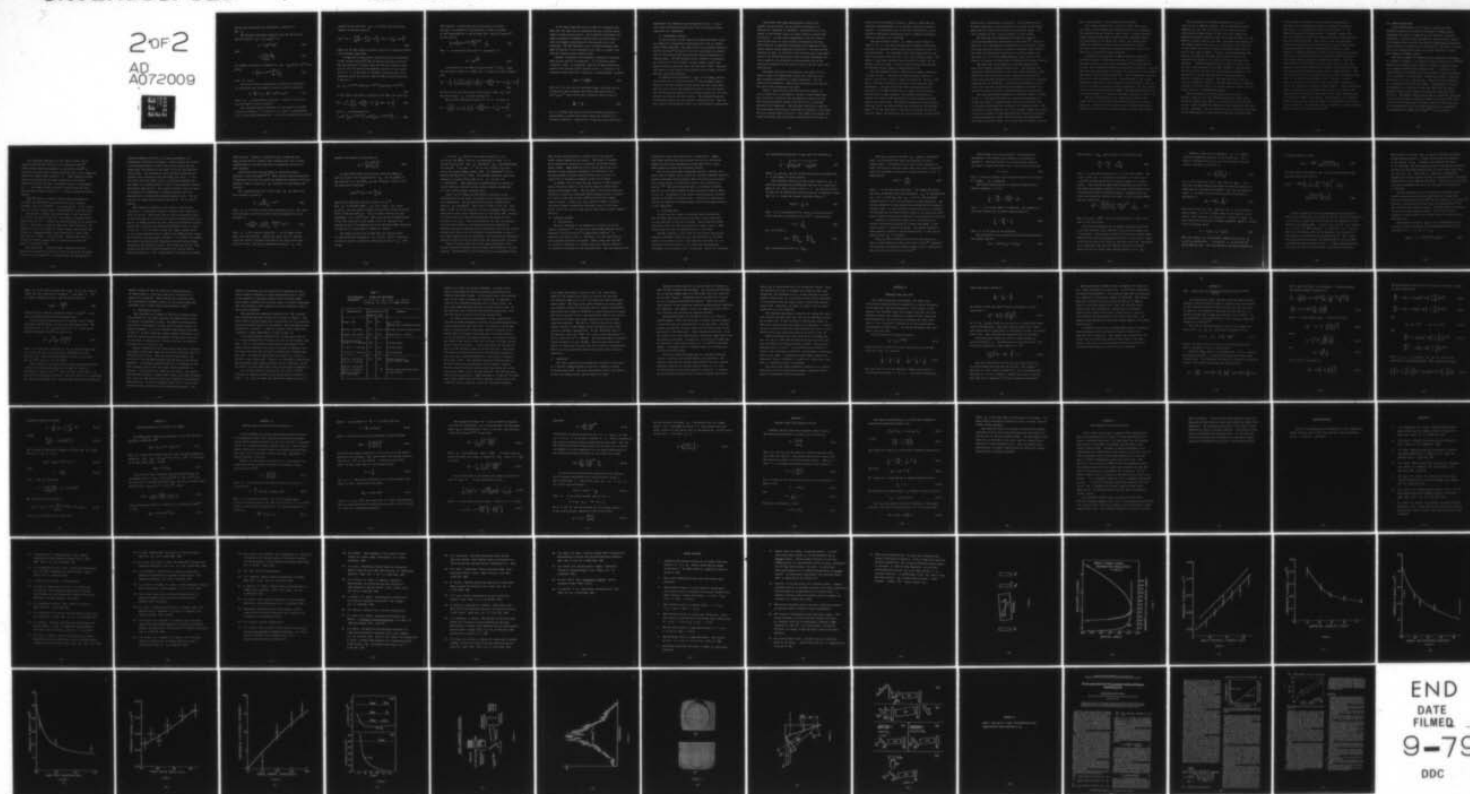
AFOSR-TR-79-0891

F49620-77-C-0092

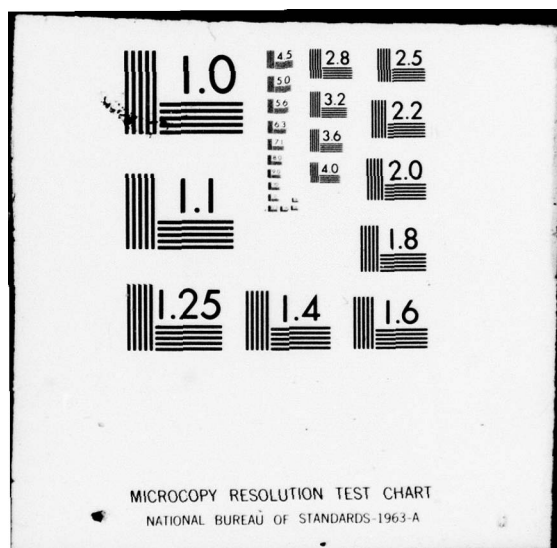
NL

2 of 2

AD
A072009



END
DATE
FILMED
9-79
DDC



Now Eq.(10) and Eq.(15) are iteratively solved for $\bar{\tau}$ and Γ_0 .

The threshold pump peak intensity using Eqs.(2) and (4) and the relation $I_p = \frac{1}{2} n c \epsilon_0 |E_p|^2$ is

$$I_0 = (\Gamma_0 \mathcal{L})^2 / \kappa g_S \mathcal{L}^2 \quad (16)$$

where

$$\kappa = \frac{2 \omega_s \omega_i d_{eff}^2}{n_s n_i n_p \epsilon_0 c^3} \quad (17)$$

For LiNbO_3 we calculate in Appendix C that $d_{eff} = 5.72 \times 10^{-12}$ m/V, giving

$$\kappa = \left(9.33 \times 10^{-10} \frac{\text{cm}^2}{\text{MW}} \right) \frac{1}{\lambda_s \lambda_i} \quad (18)$$

with λ 's in cm.

The energy fluence (energy/area) threshold is calculated by integration over the temporal intensity profile and gives,

$$J_0 = \sqrt{\frac{\pi}{2}} \tau I_0 = \sqrt{\frac{\pi}{2}} \tau (\Gamma_0 \mathcal{L})^2 / \kappa g_S \mathcal{L}^2 \quad (19)$$

where Γ_0 is found from an iterative solution of Eqs.(10) and (15) and \mathcal{L} is given in Eq.(5).

For threshold fluence estimates one can simplify the model further by assuming $\bar{\tau}$ is fixed at 2τ , which is approximately true for most OPO configurations. With this assumption from Eq.(12)

and Eq.(14) we find that $\tau_0 \mathcal{L} = 1.34 \bar{\Gamma} \mathcal{L}$ so that the energy fluence is directly given by

$$J_0(\bar{\tau} = 2\tau) = \frac{2.25}{\kappa g_s \mathcal{L}^2} \tau \left[\frac{L}{2\tau c} \ln \frac{P_n}{P_o} + 2\alpha l + \ln \frac{1}{\sqrt{R}} + \ln 2 \right]^2 \quad (20)$$

These are the SRO threshold fluence values for a Gaussian profile time dependent pump pulse.

A reduction in pump fluence threshold and some enhancement in OPO energy efficiency¹⁸ may be obtained by back reflecting the pump radiation to double pass the OPO thus creating signal gain on both the forward and backward transits of the crystal. If we let γ be the ratio of backward to forward pump field amplitude inside the crystal, then the DSRO relation analogous to Eq.(9) is

$$P_m = P_{m-1} R e^{-4\alpha l} \cosh^2[\Gamma_o \mathcal{L} e^{-(t_m/\tau)^2}] \cosh^2[\Gamma_o \mathcal{L} \gamma e^{-(t_m/\tau)^2}] \quad (21)$$

If the square gain model is applied to the DSRO, the result is

$$\bar{\Gamma} \mathcal{L} = \frac{1}{1 + \gamma} \left[\frac{L}{c\tau_B} \ln \left(\frac{P_n}{P_o} \right) + \ln \frac{1}{\sqrt{R}} + 2\alpha l + \ln \tau \right] \quad (22)$$

where $\bar{\tau}$ is determined from

$$R \cosh^2 \left[\Gamma_o \mathcal{L} e^{-(\bar{\tau}/2\tau)^2} \right] \cosh^2 \left[\Gamma_o \mathcal{L} \gamma e^{-(\bar{\tau}/2\tau)^2} \right] = 1 \quad (23)$$

This equation is satisfied only on the wings of the gain envelope, so arguments of the hyperbolic cosines are small.

In this approximation it can be shown that $\cosh \gamma x \approx (\cosh x) \gamma^2$.

We then obtain

$$\left\{ \cosh \left[\Gamma_0 \mathcal{L} e^{-(\bar{\tau}/2\tau)^2} \right] \right\}^{1+\gamma^2} = \frac{1}{\sqrt{R}} \quad (24)$$

Thus τ is given by Eq.(10) with R replaced by R' ,

$$R' = (R)^{\frac{1}{1+\gamma^2}} \quad (25)$$

A calculation of the DSRO relation between $\bar{\Gamma}$ and Γ_0 shows that Eq.(12) is valid for a DSRO also. We obtain for the threshold gain,

$$\Gamma_0 \mathcal{L} = \frac{2}{\sqrt{\pi}} \left[\frac{\bar{\tau}/2\tau}{\operatorname{erf}(\bar{\tau}/2\tau)} \right] \left(\frac{1}{1+\gamma} \right) \left[\frac{L}{c\bar{\tau}} \ln \left(\frac{P_n}{P_0} \right) + 2\alpha\ell + \ln \frac{1}{\sqrt{R}} + \ln 4 \right] \quad (26)$$

Now Eqs.(10 and (26) are solved iteratively to find $\Gamma_0 \mathcal{L}$, and threshold fluence J_0 is found from Eq.(19).

The estimated threshold fluence for $\bar{\tau} = 2\tau$ is given by

$$J_0 = \frac{2.25}{\kappa g_S \mathcal{L}^2} \frac{\tau}{(1+\gamma)^2} \left\{ \frac{L}{2c\tau} \ln \left(\frac{P_n}{P_0} \right) + 2\alpha\ell + \ln \frac{1}{\sqrt{R}} + \ln 4 \right\}^2 \quad (27)$$

In the model described here, an implicit assumption has been that the pump beam is collimated and has a uniform phase-front of high optical quality. For an SRO the requirement for pump collimation is somewhat relaxed since the idler wave is free to propagate noncollinearly with phasematching being preserved. The OPO threshold is not strongly dependent upon pump collimation if the divergence cone angle is roughly less than the Poynting vector walkoff angle.

However, threshold can be markedly increased if the pump beam optical quality is nonuniform. If a transverse phase variation $d\psi/dx$ is introduced, then as the pump traverses the crystal with Poynting vector walkoff in the x direction, the generated signal wave sees a pump with a changing phase ψ_p where

$$\psi_p(z) = \left(\rho \frac{d\psi}{dx} \right) z \quad (28)$$

From Eq.(1) we see that the transverse phase variation acts as an effective phase mismatch and reduces OPO power gain by $\text{sinc}^2 \psi_p(l)$.² The critical phase variation value is set by

$$\frac{d\psi}{dx} = \frac{\pi}{\rho l} \quad (29)$$

In a 5 cm LiNbO_3 OPO crystal the critical phase variation is approximately a quarter wave phase change per millimeter of transverse dimension. High quality lenses can easily meet this

requirement, but commercial grade elements may not. In any case, near diffraction limited pump field and imaging optical components are recommended.

B. Experimental Results

In this section the SRO theory and simplified model results are compared to experimental measurements for a 1.06 μm pumped angle tuned LiNbO_3 SRO. The pump source is an unstable resonator Nd:YAG oscillator¹⁹ operated in the far field where the central lobe of the modified Airy disk function closely approximates a Gaussian beam. The SRO threshold energy fluence is determined as a function of cavity length, crystal length, signal wave output coupling, pump spot size, and pump pulse width. Agreement with theory is very good for the highest quality LiNbO_3 crystals and input pump beam profiles.

In making these measurements a total of 26 LiNbO_3 crystals were tested over a nine month period.²⁰ The threshold energy fluence of the best crystal tested agreed very well with theory and was used to scale the experimental data to test the theory. The threshold energy fluence for an average crystal was 1.7 times greater than that of the best crystal. The standard deviation in threshold fluence for the crystals tested was 0.45. Thus the best crystal was exceptional and as yet not generally reproducible.

The Nd:YAG laser pump beam phasefront quality was another critical factor for an accurate experimental to theoretical comparison of threshold. Beam distortion in the output of some Nd:YAG lasers is severe enough to prevent OPO oscillation. In such cases propagation to the far field to allow diffraction to clean up phase perturbations may help. Beam reduction or expansion telescopes using commercial grade lenses induced enough wavefront distortion to increase the OPO threshold by 60%. It should be noted that the near field phasefront of the Nd:YAG laser source used in these experiments was of good quality as determined by interferometry and by the fractional conversion to the central lobe of the far field Airy disk profile.

The simple SRO cavity configurations are shown in Fig. 1. Figure 2 shows the LiNbO_3 angle tuning curve and the crystal gain bandwidth determined by crystal dispersion. For the theoretical-experimental comparisons discussed in this section, the simple SRO configuration was used.

Figure 3 shows the measured SRO threshold fluence vs cavity length for a 4 mm diameter, 20 nsec duration pump beam. The solid line is derived from the numerical solution of the SRO threshold condition given by Eq.(9) and is in excellent agreement with experiment. The nonlinear coefficient used for the theoretical calculation is discussed in Appendix C and yields the gain constant given by Eq.(17). The dashed line showing the simplified square pump pulse model results given by Eq.(19) is

within 10% of the numerical results. Figure 3 shows that the simplified threshold model is of adequate accuracy for design purposes. Its advantage lies in the ease with which it can be applied to OPO design calculations where a number of variables affecting threshold are considered.

The SRO threshold fluence vs LiNbO_3 crystal length is shown in Fig. 4. For these measurements a number of different crystals of comparable quality were used to minimize scatter in the measurements. The threshold values were then scaled to the value in agreement with the best 5 cm long crystal tested. The effect of pump beam Poynting vector walkoff is evident for the longest crystals tested. From the model and these measurements the optimum crystal length is approximately 5 cm.

The SRO threshold fluence dependence on signal reflectance is shown in Fig. 5. The data was taken by using a series of mirrors coated for a range of signal reflectances. However, each mirror also had a different reflectance at the pump and idler wavelengths. The data points have been individually scaled according to the DSRO to SRO ratio to reduce the variation on threshold due to pump feedback.. The present model does not include the effect on SRO threshold of varying amounts of feedback at the idler field. The problem of parametric amplification with both signal and idler present was discussed in the previous paper.¹² It was shown that if the idler is present, but of the incorrect phase, the parametric gain in the crystal is effectively

delayed until the phasing is corrected. The re-phasing occurs by idler depletion to noise followed by re-growth at the proper phase and thus reduces the effective crystal gain length. The error brackets in Fig. 5 are an estimate of this effect.

The pump spot size dependence of parametric gain for critically phasematched interactions is well known.¹⁵ Figure 6 shows the first experimental verification of the decrease in gain for small pump spot sizes as a result of Poynting vector walkoff. The model and experimental results are in good agreement and show that for a 5 cm long LiNbO_3 SRO pump, spot sizes of 4 mm diameter or greater are preferred to minimize the threshold fluence.

The model can also be applied to the OPO pumped by the near field unstable resonator beam profile. The measured and calculated threshold fluence for the near field pump beam is 50% higher than that for the far field. Therefore to obtain the lowest operating OPO threshold far field conversion of the unstable resonator mode is preferred. In the present experiments the far field conversion was accomplished by propagating the beam for a distance of 20 m by multiple reflections between plane mirrors.

The pump pulsewidths dependence of threshold fluence is shown in Fig. 7. The pump pulsewidth was adjusted by operating the Nd:YAG oscillator at varying degrees above threshold and using a following Nd:YAG amplifier to provide the required energy. The experimental values shown in Fig. 7 are somewhat higher than theory in this case because of the pump phasefront distortion caused by the Nd:YAG amplifier crystal and also because the measurements were made in the near field. It is clear from the figure that the

data, when scaled by .37, agrees well with theory.

The results shown in Fig. 7 are for a short OPO cavity. For longer cavity lengths near 15-20 cm required to accommodate the linewidth control elements, there exists a broad threshold fluence minimum resulting in nearly constant threshold values for pulsewidths in the 10-30 μ sec range. For shorter pulse widths the threshold increases due to buildup time effects. For longer pulse lengths the threshold approaches steady state values and is constant in pump intensity.

A significant improvement in SRO performance is possible by double passing the pump beam (see Fig. 1). In addition to a threshold reduction first noted by Bjorkholm¹⁸ and described by Eq.(26), this arrangement improves the oscillator stability, increases the conversion efficiency and provides for separation of the tunable OPO output from the incident pump beam. With a pump high reflector mirror after the OPO output mirror, typically 60% of the forward propagating pump beam is reflected back into the crystal. The rest is lost to mirror and crystal surface reflections. For the present case the theoretically predicted DSRO to SRO threshold reduction is 0.54 which compares to a measured threshold reduction of $0.68 \pm .15$.

The DSRO configuration can be simplified by coating the output mirror to reflect both the resonated signal wave and the pump wave. Coatings of this type have been designed and used in DSRO operation in spite of the more complex coating requirements.

The advantages of the DSRO configuration are not as clear cut as it appears, however. The net threshold fluence reduction is real, but the fluence at the crystal surface, which governs crystal damage is the sum of the forward and backward travelling pump waves and in fact may be larger for the DSRO at threshold than for the SRO. The double pass pumping of the LiNbO_3 crystal also leads to a reduction in the intensity at which small scale self focusing occurs, thus increasing the risk of this type of damage. Finally, the reflected pump beam must be isolated from the pump laser source to prevent the possibility of damage to the laser oscillator from excessive feedback. A pulsed Faraday rotator isolator is usually used for near field operation of the SRO and DSRO.²¹ For operation in the far field, the 20 m one way propagation distance to the OPO provides a round trip time delay of 120 nsec which is sufficient temporal isolation. For SRO operation in the far field no feedback is observed. For DSRO operation some feedback influence is evident, but is not strong enough to affect the pump laser oscillator or the DSRO performance.

The experimental or useful conversion efficiency η , defined as the ratio of the external signal plus idler output energy to incident pump energy, is shown in Fig. 8 for the SRO. At three times threshold the observed energy conversion efficiency is 18%. Bjorkholm has considered the power conversion efficiency for the SRO pumped by a plane wave and Gaussian intensity beam.

In his analysis an integral over the spatial mode profile of the pump wave was performed yielding a fractional transmitted pump power vs the number of times above threshold N . For pulsed OPO operation considered here, a temporal integral must also be performed to obtain the energy conversion efficiency from the peak power efficiency. The result is that the peak power conversion efficiency must be scaled by the ratio of the signal-to-pump pulsewidth, which is approximately given by $1-1/N$. Finally, to compare Bjorkholm's results to the measured conversion efficiency, the internal conversion efficiency must be scaled by the crystal surface and mirror transmittance losses. For the simple SRO cavity considered here the scale factor is 0.6. The agreement between the theoretically expected conversion efficiency and the measured efficiency is quite good as shown in Fig. 8. The conversion efficiency of the SRO continues to increase monotonically with N as shown earlier by Byer et.al.⁷ However, reliable operation at values of N much greater than three is difficult due to the limitations imposed by crystal damage. A more appropriate means of increasing the net OPO output energy is to increase the pump beam area but maintain operation at three times threshold for the maximum available laser energy. An alternative is to utilize an optical parametric amplifier (OPA) after the OPO as an efficient energy converter. The characteristics of the OPA as a power amplifier were discussed in the previous paper.¹²

III. DAMAGE LIMITATIONS

A good understanding of the factors affecting the OPO threshold coupled with a detailed knowledge of LiNbO_3 damage mechanisms and limits is required for the design of a reliable oscillator. In this section experimental and theoretical results are presented which describe the observed LiNbO_3 damage mechanisms. Surface damage is discussed first followed by a discussion of small-scale self-focusing which leads to internal tracking or "angel hair" damage of LiNbO_3 crystals.

The surface damage of LiNbO_3 has been extensively considered by a number of workers. In a series of papers Zverev et.al.,^{22,23,24} proposed that LiNbO_3 surface damage is caused by thermal heating of an oxygen depleted niobium surface layer. In addition, the reduced niobium is assumed to be concentrated at crystal imperfections, inclusions, or microcracks. Damage measurements, initially made by Zverev et.al., and recently repeated in this laboratory, are in agreement with this basic model. Measurements of surface energy damage as a function of spot size show that the damage threshold fluence rises sharply for pump spot sizes less than 60-70 μm . The damage fluence varies from 2.7 J/cm^2 for large spot sizes to greater than 11 J/cm^2 for tightly focused spots.²⁵ This indicates a mean separation of surface defects on this order and is not inconsistent with the recent observation of microdomains and antidomains in LiNbO_3 and LiTaO_3 ,^{26,27} at this density.

The pulsewidth dependence of the damage fluence can be found by modeling the trap sites as an absorbing layer.²⁴ Using thermal diffusion arguments as outlined by Bliss²⁸ we find that for short pulses during which the layer is not completely heated the fluence limit scales as $\sqrt{\tau}$. When complete heating occurs, but pulsewidths are short compared to the thermal diffusion time into the bulk, the damage fluence is independent of τ . For longer pulses, diffusion occurs during the pulse and the damage fluence scales as τ , thereby becoming intensity limited.

Zverev²⁴ reports a constant fluence damage threshold of 4.6 J/cm^2 for pulsewidths less than 30 nsec and a constant intensity limit of 170 MW/cm^2 for longer pulses. In an earlier paper he quotes a damage limit of 120 MW/cm^2 for a 30 nsec pulse.

The results of damage measurements made in our laboratory at $1.06 \text{ }\mu\text{m}$ are shown in Fig. 9a. We measure a constant fluence damage limit of $2.7 \pm .4 \text{ J/cm}^2$ for uncoated LiNbO_3 in the 10-30 nsec region. This value is somewhat lower than Zverev's results. For reference, Fig. 9 also shows the energy fluence just outside the surface of an average LiNbO_3 crystal operating at three times threshold for a short 8 cm cavity SRO. Clearly some means of raising the surface damage limit is desirable for long term damage free OPO operation.

The niobium ion reduction model, proposed by Zverev, provided the incentive to test the effect of oxygen on the damage fluence level of LiNbO_3 .²⁹ The measurements were performed by

mounting LiNbO_3 test plates in an oxygen atmosphere in a temperature controlled environment. Surface damage was defined as the maximum fluence at which the crystal surface did not damage when irradiated for one minute at 10 pps by Q-switched laser pulses. All measurements were carefully normalized to a standard room temperature uncoated LiNbO_3 test plate. It has been shown that the damage fluence is strongly dependent upon the number of integrated pulses as well as pulse spatial diameter and spatial mode quality. The 1 minute survival time was chosen to eliminate the dependence on integrated pulses and to be representative of actual OPO operating damage levels. The spot size was set significantly larger than the 60 - 70 μm defect spacing.

When oxygen was supplied to the crystal, even at room temperature, a significant increase in damage level resulted as shown in Fig. 9a. This result was not totally unexpected since it has been known for some time that oxygen diffuses rapidly into and out of LiNbO_3 crystals and that SiO_2 anti-reflection coatings significantly increase the LiNbO_3 surface damage level as shown in Fig. 9a. It is not clear whether the SiO_2 coating itself or the coating procedure acts to replace the LiNbO_3 surface oxygen and yield the increased damage threshold. It is known that LiNbO_3 anti-reflection coated with ThF_4 shows the same surface damage threshold as the uncoated crystal. The convenience of the SiO_2 coating and its anti-reflection reduction of surface Fresnel reflection losses to 1-2% clearly make it the choice for LiNbO_3

OPO operation. However, it should be kept in mind that the SiO_2 coating must be flawless since imperfections lead to phase perturbations of the pump beam that can aggravate the onset of self focusing.

Small-scale self-focusing using an instability theory approach is given by Suydam.^{31,32} Small spatial beam perturbations in amplitude and phase are amplified through the nonlinear intensity dependent index of refraction n_2 resulting in beam breakup and focusing.

For a Gaussian beam the critical power P_c for whole beam self-focusing is given by

$$P_c = \frac{\lambda_o^2 c}{32 \pi^2 n_2} \times 10^{-7} \quad (30)$$

where P_c is in Watts and the other parameters are in cgs units. For small-scale self-focusing the intensity damage limit given by Suydam is

$$I_d \left(\frac{W}{\text{cm}^2} \right) = \frac{\lambda_o c n}{48 \pi^2 n_2} \frac{\ln(3/\delta)}{z_f} (10^{-7}) \quad (31)$$

where z_f is the focusing length and δ is the depth of the small scale perturbation. Suydam also shows that an optimum transverse spatial frequency perturbation for small-scale self-focusing exists. The spatial modulation dimension λ_m that

produces the greatest self-focusing is

$$\lambda_m = \lambda \left[\frac{c \cdot 10^{-7}}{12 \pi n_2 I} \right]^{\frac{1}{2}} \quad (32)$$

To apply small-scale self-focusing theory to LiNbO_3 we need an estimate for the magnitude of n_2 . We are unaware of any measured value for LiNbO_3 n_2 and, therefore, choose to use the approximate expression

$$n_2(10^{-13} \text{ esu}) = 391 \frac{n_d - 1}{v_d^{5/4}}$$

based on the empirical relation of Boling et.al.³⁴

Here v_d is the Abbé number, $v_d = (n_d - 1)/(n_f - n_c)$ where n_d and n_c are the crystal indices of refraction at the wavelength 0.486, 0.588 and 0.656 μm . Using the above relation we find $n_2(\text{LiNbO}_3) = 11.1 \times 10^{-13}$ esu. This value may be an underestimate of the true value due to the effect of the d states of the niobium ion and to the application of the empirical model developed for glasses to a high index of refraction crystal.

For LiNbO_3 we find from Eq.(30) that the critical power for whole beam self focusing is $P_c = 100 \text{ kW}$. This is comparable to critical powers for materials with large values of n_2 , such as CS_2 .

If we set z_f equal to the crystal length of 5 cm, (10 cm for the DSRO), then for a perturbation of order $\delta = 1$ we find from Eq.(31) that $I_d = 290 \text{ MW/cm}^2$ ($I_d = 145 \text{ MW/cm}^2$ DSRO) for the SRO. If we take $\delta = .15$, as for a defect in an anti-reflection coated LiNbO_3 surface, then $I_d = 800 \text{ MW/cm}^2$ for an SRO and 400 MW/cm^2 for a DSRO. The optimum transverse modulation dimension is found from Eq.(32) to be $\lambda_m = 0.5 \text{ mm}$ for $I = 300 \text{ MW/cm}^2$. This dimension is approximately the spacing of crystal Schlieren defects and the Fresnel intensity modulation of a near field unstable resonator beam.

Since n_2 for LiNbO_3 and the detailed character of the perturbations are not known, the damage values presented here are only approximate. One measured data point gave a DSRO damage track at $I_d = 300 \text{ MW/cm}^2$. This value is shown in Fig. 9b. Also shown in Fig. 9b is the intensity inside an average LiNbO_3 crystal operating at three times threshold for an 8 cm cavity SRO. Clearly, for pump pulses less than 10 nsec duration the danger of self-focusing is critical. This is particularly the case for crystals with Schlieren defects or for beam perturbations produced by imperfect coatings or damaged optical components prior to the crystal. An additional factor may be introduced by partial mode locking or axial mode modulation in the pump beam. The resultant instantaneous intensity values may easily exceed twice the average peak intensity.

Figure 9 clearly shows that longer pump pulsewidths reduce the OPO intensity threshold and thus reduce the probability of self-focusing. Experimentally we have found that for pulsewidths longer

than 15 nsec self-focusing is avoided even in the case of severe surface damage to the crystal. The longer O-switched pulse lengths were obtained by increasing the Nd:YAG optical cavity length. Added benefits of the longer pump pulse are a decrease in the operating linewidth of the OPO due to the increased number of passes during buildup and a greater insensitivity of intensity threshold on OPO cavity length.

In summary, Fig. 9 shows that any increase in OPO threshold brings the device closer to the surface damage or small-scale self-focusing damage limit. One may either rely on the SiO_2 anti-reflection coating for increased surface damage fluence or operate at a fluence less than the 2.7 J/cm^2 set by the bare LiNbO_3 crystal surface. In any case, care should be taken to minimize the energy fluence threshold by the proper choice of OPO parameters and by the use of a high quality pump beam of proper temporal duration.

IV. LINEWIDTH CONTROL

A. Introduction

The gain linewidth of the parametric oscillator is set by crystal dispersion.^{2,3} For the angle tuned LiNbO_3 SRO the crystal bandwidth varies from 10 cm^{-1} to approximately 200 cm^{-1} at degeneracy as shown in Fig. 2. Therefore, for most applications some linewidth reduction is desired. Theory shows that the SRO is capable of operating in a single axial mode without reduction of conversion efficiency at the resonated wave. The non-resonated wave

reflects the axial mode spectrum of the pump field. Single axial mode operation has been achieved earlier for the Nd:YAG pumped non-critically phasematched LiNbO_3 SRO using a single high resolution etalon line narrowing element.

The present angle tuned LiNbO_3 SRO requires a primary linewidth control element and an etalon for narrower linewidth operation. Primary linewidth control elements that have been tried include a thin tilted etalon, a birefringent filter, and a diffraction grating.^{7,37} The most attractive method of primary linewidth control is a grating preceeded by beam expansion prisms as shown in Fig. 10. An analysis of the prism expander-grating linewidth control of the OPO is presented next. In Section C experimental results are described including stable single axial mode operation of the LiNbO_3 SRO.

B. Linewidth Model

In this section a model is developed that describes the SRO linewidth when operated with a resonant cavity consisting of beam expansion prisms and a grating. This method of primary linewidth control was selected because of linear tuning, a wide tuning range and ease of implementation at a low cost.

The OPO linewidth is the result of the crystal and grating component lineshape functions after consideration for multiple passes in the optical cavity. The resultant linewidth $\Delta\nu$ is calculated from the product of the individual multiple-pass lineshapes of the crystal and of the grating. Since the lineshapes

are approximately Gaussian, we may write the linewidth as

$$\frac{1}{\Delta\nu} = \sqrt{\frac{1}{[\Delta\nu_c(p)]^2} + \frac{1}{[\Delta\nu_g(p)]^2}} \quad (33)$$

where $\Delta\nu_c$ and $\Delta\nu_g$ are the crystal and grating linewidths and p is the number of cavity transits.

The lineshape function for the crystal bandwidth $\Delta\nu_c$ is given by evaluating the $\text{sinc}^2(\Delta k \ell / 2)$ function for a phase mismatch of Δk and a crystal length of ℓ . An analysis similar to that for the diffraction grating presented in Appendix D shows that for p passes the crystal linewidth reduces to

$$\Delta\nu_c(p) = \frac{1}{\sqrt{p}} \Delta\nu_c \quad (34)$$

where $\Delta\nu_c$ is determined by the crystal dispersion between signal and idler wavelengths and in cm^{-1} is approximately

$$\Delta\nu_c = \frac{2}{\ell \beta_{si}} \quad (35)$$

β_{si} is defined by

$$\beta_{si} = \left. \frac{\partial k_s}{\partial \omega} \right|_{\omega_{so}} - \left. \frac{\partial k_i}{\partial \omega} \right|_{\omega_{io}} \quad (36)$$

and is approximately equal to $2\Delta n_{si}$.

This basic crystal linewidth $\Delta\nu_c$ assumes a collimated pump. For divergent pump beams the linewidth increases significantly. An expansion of the wave vector mismatch for small deviations of the pump input angle and signal frequency¹² gives the linewidth increase due to pump divergence $\delta(\Delta\nu)$ of approximately

$$\delta(\Delta\nu) = \frac{2\rho\alpha}{\lambda_p \beta_{si}} \quad (37)$$

where α is the pump beam cone angle. For LiNbO_3 OPO signal and idler frequencies away from degeneracy, β_{si} is approximately 0.1. For $\rho = 0.03$ rad and $\lambda_p = 1.06 \mu\text{m}$, the linewidth broadens nearly 6 cm^{-1} per milliradian of pump divergence. The crystal bandwidth is then significantly broadened by a diverging incident pump. If line narrowing elements are used, an increase in threshold may be observed because part of the generated signal wave is removed from the gain medium by cavity frequency selection.

Consider the OPO cavity shown in Fig. 10 which uses a Littrow configuration grating at resonant wavelength λ_s and grating angle θ relative to normal. For added resolution a beam expansion element of linear magnification M and angular magnification M_a is included.

The prism beam expander has been described earlier as a means of beam expansion within a dye laser cavity.³⁸ Klauminzer has discussed its advantages, which include ease of construction and insertion into the optical cavity.³⁹

Using LiNbO_3 as the prism material, we designed and constructed a two element prism expander as discussed in Appendix E. The magnification of a single prism, taken as the output to input beam width ratio W/w is given by Eq.(E5)

$$M = \tan \theta \quad (38)$$

For N prisms in sequence the net magnification is the product $M = M_1 M_2 M_3 \dots M_n$ as expected.

The angular magnification of a Brewster angle prism is shown in Appendix E to be

$$\frac{1}{M_a} = \frac{\delta\theta_e}{\delta\theta_i} = \frac{1}{n} \left(\frac{1}{M} \right) = \frac{1}{M^2} \quad (39)$$

where n is the prism index of refraction. For comparison, a telescope expander has an angular magnification of

$$\frac{1}{M_a} = \frac{\delta\theta_e}{\delta\theta_i} = \frac{1}{M} \quad (40)$$

where M is the power of the telescope.

The resolution of the grating is found by differentiating the grating equation

$$m \lambda_s = d(\sin \theta_{in} + \sin \theta_{out}) \quad (41)$$

with respect to θ_{out} which yields, for the Littrow case

$$\frac{d\lambda_s}{\lambda_s} = \frac{dv_s}{v_s} = \frac{d\theta}{2 \tan \theta} \quad (42)$$

Here, d is the groove spacing and m is the order number. The angular width $\Delta\theta$ is calculated in Appendix D for the case of a multiple passed grating with an optical length $2L$ between passes. The calculation shows that diffraction not only sets the single pass angular width but also puts a lower bound on the linewidth attainable by multiple passing. Using Eq.(D.12) we write the diffraction limited full width at half maximum (FWHM) grating linewidth as

$$\Delta\nu_g^{DL} = \frac{\sqrt{2 \ln 2}}{2 \tan \theta} \left(\frac{M}{M_a} \frac{4 L \lambda_s}{\pi w_s^2} \right)^{1/3} \frac{1}{\pi M w_s} \quad (43)$$

where the factor $\sqrt{2 \ln 2}$ converts the halfwidth at $1/e^2$ linewidth to the FWHM value.

The grating resolution may be broader than that specified in Eq.(43) when the finite aperture set by the gain medium size is considered. Wave packets outside the diffraction limited bandwidth may oscillate by propagating off-angle in the cavity. These waves may experience gain over the full pump beam area. Therefore, to be consistent with the $1/e^2$ angular width used to obtain Eq(43) we take the proper pump aperture diameter to be $2w_p$.

Consider a light ray of wavelength $\lambda_0 + \Delta\lambda$ which is initially propagating parallel to the cavity axis. It is shown in Appendix D that after its q 'th reflection from the grating, its angle to the axis is

$$\Delta_q = \left(\frac{M \Delta\lambda}{d \cos \theta_0} \right) q \quad (44)$$

After a beam expansion device, this angle is $M_a \Delta_q$. If we note that the gain region establishes an effective aperture of width equal to the pump spot diameter $2w_p$, then the number of passes p in which the ray travels across the aperture is determined by

$$2w_p = 2DM_a \Delta_1 \sum_{q=1}^p q \quad (45)$$

where the sum has the value $p(p+1)/2$ and D is an effective cavity length. In air, D would simply be the physical cavity length. Here, however, the presence of a crystal of index n_s and a beam expansion device of angular expansion M_a (M^2 for prisms, M for a telescope) gives

$$D = \ell_c/n_s + \ell_a + \ell_{ex}/M_a \quad (46)$$

where the crystal, air and expander lengths are given by ℓ_c , ℓ_a and ℓ_{ex} respectively. In practice, p is fixed by the cavity buildup time. The contribution to grating linewidth due

to cavity geometry is then

$$\Delta\nu_{\text{cav}} = \sqrt{2\ln 2} \frac{2 w_p \cos \theta}{m p(p+1) D \lambda_s^2 M_a} \quad (47)$$

The full grating linewidth is thus a sum of the diffraction and aperture width terms given by

$$\Delta\nu_g(p) = \sqrt{2\ln 2} \left[\frac{1}{2 \tan \theta} \left(\frac{M}{M_a} \frac{4 L \lambda_s}{\pi w_s^2} \right)^{1/3} \frac{1}{\pi M w_s} + \frac{2 w_s d \cos \theta}{m p(p+1) M_a D \lambda_s^2} \right] \quad (48)$$

We now consider the relative magnitudes of the diffraction and aperture width terms in Eq.(48) for typical cavity configurations in an effort to understand which parameters are important to the design of a narrowband QPO. If we let $w_p = 0.2$ cm, $w_s = 0.06$ cm, $\lambda_s = 1.7$ μm , $\frac{1}{d} = 6000$ lines/cm, $D = 8$ cm and $m = 1$, we find that for a 10 ns pump pulse and no expansion, the inclusion of the aperture term increases the linewidth by 30%. For a 20 ns long pump pulse the aperture term contribution to the linewidth is reduced by multiple passing to 8%. If beam expansion prisms are used, the effect of the aperture term becomes negligible.

From Eq.(48) it is clear that to improve linewidth performance we may increase grating θ and/or increase the beam diameter on the grating, $2 M w_s$. However, each approach has limits. As θ increases, the free spectral range of the grating decreases and does not allow OPO operation over the full tuning range from $1.4 \mu\text{m}$ to $2.1 \mu\text{m}$. Increasing M requires a 4 prism beam expander and a larger grating and has the disadvantage of increasing threshold due to the added cavity length. However, for sufficiently long pump pulsewidths near 20 ns the increase in threshold may be tolerable.

Various techniques exist for additional linewidth control. Single frequency operation using interferometer arrangements have been demonstrated for lasers⁴⁰ and for parametric oscillators.³⁵ Internal tilted etalons have also been used successfully,⁴¹ but have suffered from insertion losses, a problem which is alleviated by the use of beam expansion prisms. Due to their ease of alignment we have chosen to use tilted etalons to attain narrow-band operation.

The lineshape function $f_e(\Delta\nu)$ for a transmitted beam of a tilted etalon is Lorentzian in the frequency deviation from resonance, $\Delta\nu = \nu - \nu_0$, for $\Delta\nu \ll \nu_0$,

$$f_E(\Delta\nu) = [1 + 4 \mathcal{F}^2 (\Delta\nu)^2 / (\Delta\nu_{\text{FSR}})^2]^{-1} \quad (49)$$

where \mathcal{F} is the etalon finesse and $\Delta\nu_{\text{FSR}}$ is the free spectral range $2nt$ for a material of thickness t and index n . For p passes through the etalon, the linewidth reduces to

$$\Delta\nu_E(p) = \frac{\Delta\nu_E(1)}{\sqrt{p}} \quad (50)$$

Clearly Eq.(33) could be extended by adding $(\Delta\nu_E(p))^{-2}$ to the sum of linewidth factors under the square root.

For the present application as an internal cavity element with short optical pulses, various loss mechanisms arise. The insertion loss γ for a tilted etalon in a cw laser cavity has been treated by Leeb⁴² and found to be

$$\gamma_E = \frac{2R}{(1 - R)^2} \left(\frac{2t \theta_E}{n w_0} \right)^2 \quad (51)$$

where R is the power reflectivity, θ_E is the tilt angle and w_0 is the spot size in the direction perpendicular to the rotation axis. When the prism expander is used, w_0 is large and $\gamma_E < 10\%$ even for a $\mathcal{F} = 20$ etalon.

A more important loss mechanism for short pulse applications is due to the delay propagation time through the etalon as considered by Daussy et.al.⁴³ They find that a delay near 1 ns may occur for high finesse etalons. This can amount to a considerable loss during the buildup time, increasing OPO threshold prohibitively.

Another finding is that the effective pulsed finesse may be significantly ($\sim 1/3$) lower than that calculated for a steady state condition. These results are consistent with our experimental linewidth results for the pulsed LiNbO_3 OPO operating with a tilted etalon line-narrowing element.

C. Experimental Results

The linewidths for a number of OPO cavity configurations (see Appendix F), have been measured and compared with theory. In general the agreement is good. The observed discrepancies can often be attributed to factors such as crystal quality or optical alignment. As in the threshold measurements described in Part II, we have found that crystal optical uniformity is an important factor and that the presence of Schlieren variations in the index of refraction of a crystal increase the measured linewidth up to a factor of two.

Optical alignment of the cavity and of pump beam collimation telescopes is also more important for narrow linewidths than for threshold minimization. Some care must be exercised in the centering of the grating resonance upon the peak of the crystal bandwidth. A lineshape asymmetry caused by a broadening of the high frequency side of the line occurs if this condition is violated. If the grating is tuned off line center, the crystal phasematching condition is broken more slowly on the high frequency side, since the OPO waves may then angle phasematch and propagate noncollinearly. On the low frequency side $\Delta k > 0$ so that the OPO waves remain collinear but are reduced in magnitude. The

amount of broadening may be calculated by expanding the wave-vector mismatch allowing for angle phasematching and is found to be quadratic in the angle between signal and pump beams. For minimum linewidths and collinear beams it is then recommended that the grating be tuned slightly to the low frequency side of the crystal bandwidth.

The measured and calculated linewidths for OPO cavities with increasing spectral selectivity are given in Table I. The first block of entries shows that a prism power of 10 is required to give wavelength control to the grating. The resulting grating linewidth is 0.53 cm^{-1} . A typical linewidth trace taken using a scanning 1 meter spectrometer is shown in Fig. 11.

It is experimentally observed that the OPO output beam at 2 - 3 times threshold has the same spot size as the incident pump beam. This is explained by noting that the confinement of the signal beam is relaxed as the peak of the pump is depleted, and the signal spot size may increase to approach the incident pump spot size. It might be argued that the proper w_s to use in Eq.(48) is this larger spot. However, the linewidth is determined during buildup before depletion occurs and is, therefore, set by the smaller confined signal spot size as calculated in Appendix A.

If a tilted etalon is inserted into the cavity, the OPO linewidth is reduced as shown in the second group of entries in Table I. As a rule of thumb, the etalon free spectral range is

TABLE I

OPO LINEWIDTHS : THEORY AND EXPERIMENT

PARAMETERS : $\lambda_s = 1.6 \mu\text{m}$, $w_p = .2 \text{ cm}$, $\tau_p = 10 \text{ ns}$,
 $L = 20 \text{ cm}$, $D = 8 \text{ cm}$, $N = 6000 \text{ lines/cm}$

Configuration	Linewidth (cm^{-1})		Comments
	Theory	Expt	
Grating only	2.2	2.2	$w_p = .15 \text{ cm}$ Crystal has wavelength control
Grating, x5 prisms	.86	.73-1.2	Grating & crystal both control
Grating, x10 prisms	.40	.53	Grating has λ control
Grating, x5 prisms + 2 mm, F = 7 etalons	.059	< .1	2 etalon modes
+ 1 mm, F = 7 etalons	.15	.14	1 etalon mode
+ .5 mm, F = 7 etalons	.3	.63	1 etalon mode
Grating, x10 prisms 2 mm, F = 7 etalons	.02	.075	20 ns pump pulse 3 axial modes FWHM
Grating, x10 prisms 2 mm, F = 7 etalons Reflective etalon (R = 50%, 60%)		< .02	Single axial mode operation - very stable

chosen to be twice the grating linewidth. A single etalon mode is then produced with the linewidth determined by the effective multipass finesse. As discussed above, the insertion loss of the etalon increases with increasing \mathcal{F} imposing a limit on the linewidth attainable with a single etalon. We have found experimentally that for a finesse greater than 10 the insertion loss raises the OPO threshold excessively, even when the etalon is used in the prism expanded beam.

In a final series of measurements we have improved the line-narrowed OPO performance and have successfully demonstrated stable single axial mode operation. An elliptical 20 ns pump beam was incident with a 6 mm major diameter oriented in the walkoff plane to minimize threshold and a 2 mm minor diameter set as the aperture for grating narrowing. A reflective etalon was added to the cavity in the form of a pair of output coupler mirrors spaced 5 cm apart. In this experiment the non-optimum choice of 50% and 60% reflecting mirrors was used. The output linewidth was analyzed by diverging the OPO output through an air spaced plane parallel Fabry-Perot etalon with a finesse of 20 in the visible. The resulting rings were observed with an infrared vidicon and photographed from the monitor display. With the output reflective etalon mirror misaligned the etalon ring pattern shown in Fig. 12a was obtained. The pattern shows that the OPO operated at a FWHM linewidth of 0.075 cm^{-1} , or three axial modes spaced 0.025 cm^{-1} apart. When the outside mirror was aligned to form a reflecting etalon the linewidth collapsed

to a single axial mode, as shown in Fig. 12b. The etalon effect of the output mirror pair was verified by observing the frequency jumps of 0.1 cm^{-1} by tilting the lower resolution etalon angle. The single axial mode frequency was quite stable and repeatable which is noteworthy since no special experimental precautions were taken to establish an interferometrically stable OPO cavity. Also, due to the 1 sec. persistence time of the vidicon, observation of clear axial modes supports the claim of their frequency stability. The OPO is a reactive device with small thermal loading of the LiNbO_3 crystal and optical cavity thus avoiding resonator instabilities. To the resolution limit of the analyzer etalon the FWHM of a single axial mode appears to be less than 0.01 cm^{-1} or 300 MHz. The expected Fourier transform limited bandwidth is near 100 MHz. The measured output pulse energy in single mode operation was 10 mJ, which is approximately 80% of the un-narrowed OPO output energy under similar pumping conditions.

V. CONCLUSION

This paper summarizes the parameters relevant to the design of a reliable LiNbO_3 parametric oscillator capable of stable narrowband operation. The prime requirements involve the quality of both the LiNbO_3 crystal and the pump laser beam.

Imperfect crystal quality is a major cause of increases in both the OPO threshold and linewidth. The oscillation threshold for an average LiNbO_3 crystal is 70% higher than that predicted for an ideal crystal. Linewidths may be increased by a factor of two in crystals with Schlieren defects. Pump laser phase-front quality is also important and high quality optical components are essential. For example, the use of commercial grade lenses in a telescope may increase the threshold by 60%.

The operating limits of the OPO are set by the onset of crystal damage. There are two types of damage, and each imposes a constraint upon the configuration of the pump beam. Internal crystal tracking due to small scale self-focusing scales as the peak power of the pump pulse. Pulse lengths greater than 10 ns are essential to avoid self-focusing, and pulses longer than 15 ns are highly recommended. In addition, the surface of LiNbO_3 may be damaged by a peak energy fluence of 2.7 J/cm^2 for uncoated LiNbO_3 . The damage limit is somewhat higher for an SiO_2 anti-reflection coated surface.

We have designed the LiNbO_3 OPO for a minimum threshold fluence to provide for reliable damage free operation. The threshold increase due to pump beam walkoff leads to a minimum pump spot diameter of 4 mm and crystal length of 5 - 6 cm. In addition the cavity length should be minimized. A complete cavity, including grating, prism ten-power expander and tilted

etalon may be constructed with a 16 cm physical length. Since the effective loss due to buildup time dominates other loss mechanisms, the threshold is not a strong function of output coupler reflectivity R . For greater useful energy conversion it is necessary that the output coupler provide the dominant cavity loss. Therefore, we choose to operate with an output reflectivity of less than 50%.

The required pump energy to operate the LiNbO_3 SRO varies with crystal and pump laser, but lies in the 100-150 mJ range. As an added note, we have operated a considerable number of OPO cavity configurations as summarized in Appendix F. However, the best results to date have been obtained with the "L" cavity which utilizes the input beam splitter as shown in Fig. 10.

Narrow linewidths have been achieved in the LiNbO_3 OPO with the use of a 600 ℓ/mm diffraction grating in first order with the addition of a $10\times$ prism beam expander. The measured linewidths were 0.5 cm^{-1} . A 2 mm tilted etalon with $\mathcal{F} = 7$ reduces this linewidth to 0.08 cm^{-1} , corresponding to operation with 3 axial modes. A reflective etalon output coupler configuration further collapses the output to a single axial mode which is remarkably stable in frequency.

The angle tuned LiNbO_3 parametric oscillator is a useful laboratory tool for studies which require a broadly tunable source of narrowband infrared radiation.

APPENDIX A

RESONATED WAVE SPOT SIZE

For a Gaussian profile gain medium, the signal spot size evolves during buildup to threshold to a radius determined by the pump spot size and diffraction. We calculate in this appendix the resonated signal wave steady state spot size and determine whether this condition is indeed reached during the OPO buildup time. We proceed by considering the signal spot size as it is iteratively narrowed by the gain polarization and broadened by diffraction. The balance determines the final signal wave spot size.

Let the fields have Gaussian profiles,

$$E_j = E_{j0} e^{-r^2/w_j^2} \quad (A.1)$$

From Eq.(1) we see that the driving polarization for the OPO waves have radii \bar{w}_i given by

$$\frac{1}{\bar{w}_s^2} = \frac{1}{w_i^2} + \frac{1}{w_p^2}, \quad \frac{1}{\bar{w}_i^2} = \frac{1}{w_s^2} + \frac{1}{w_p^2} \quad (A.2)$$

The idler wave is free and therefore, assumes the profile of its driving polarization, or $\bar{w}_i = w_i$. The signal polarization

radius may now be written as

$$\frac{1}{\bar{w}_s^2} = \frac{1}{w_s^2} + \frac{2}{w_p^2} \quad (\text{A.3})$$

The radius of this wave when allowed to propagate a cavity round trip is

$$\bar{w}_s'^2 = \bar{w}_s^2 \left[1 + \left(\frac{2L\lambda}{\pi \bar{w}_s^2} \right)^2 \right] \quad (\text{A.4})$$

We let $\bar{w}_s' = w_s$ and iterate to see how soon a stable signal mode radius is established. Numerical iteration shows that a spot size within 30% of steady-state is established in only 2-3 cavity round trips. This verifies the assumption made in the model.

The steady state signal spot size is found directly by again letting $\bar{w}_s' = w_s$ and substituting (A.4) into (A.3). The resulting condition is a cubic equation in \bar{w}_s^2 ,

$$\left(\frac{\pi}{2L\lambda} \right)^2 \bar{w}_s^6 + \bar{w}_s^2 - \frac{w_p^2}{2} = 0 \quad (\text{A.5})$$

From this calculation we find that the signal spot size is significantly less than that of the pump. For example, a pump spot of 2 mm radius incident on a 15 cm long OPO cavity operating at 1.9 μm produces a signal spot size of 0.62 mm. This spot size is important for later linewidth calculations.

Some experimental evidence exists to support the prediction for a small confined signal spot size. In an initial experiment to measure OPO threshold, a 6 mm diameter pump beam was apertured to a diameter of 2 mm with no change in threshold. This showed that near threshold only the central portion of the pump is useful in providing signal gain. Next, the flat OPO cavity output mirror was replaced by a curved mirror to produce a Gaussian mode stable cavity with a signal spot size equal to that predicted by the confined signal calculation above. No change in OPO threshold was observed lending support to the model presented here.

It should be noted that for higher pump powers the Gaussian profile assumed in this calculation becomes flattened and distorted due to depletion. This relaxes the constraint on the signal spot size which may expand to match that of the pump. However, the spot size calculated here should be valid during the OPO buildup time and at operation near threshold.

APPENDIX B

SRO - Single Pass Gain Solution Including Poynting Vector Walkoff

To calculate the signal and idler field buildup in an OPO resonator some care must be taken to consider only that fraction of the generated signal wave which couples into the resonator. In addition, the coupling of the pump and generated waves is gradually broken due to pump wave Poynting vector walkoff. It is convenient to treat both effects in the coupling coefficient formalism of Kogelnik.¹⁴

The radii of the polarization fields for the signal and idler waves, \bar{w}_s and \bar{w}_i , are found in Appendix A to be

$$\bar{w}_i = w_i \quad \bar{w}_s = [1/w_s^2 + 2/w_p^2]^{-1/2} \quad (\text{B.1})$$

Because the signal wave is resonant its polarization profile must be expanded in terms of cavity modes.

Only the TEM_{00} mode is of interest here. Let P_j represent the Gaussian profile of a polarization which drives the signal or idler wave. If we describe the fields in transverse coordinates x and y the coupling coefficient can be written as

$$c_{00} = \left[\int_{-\infty}^{\infty} P_j(x) E_j^*(x) dx \right] \left[\int_{-\infty}^{\infty} P_j(y) E_j^*(y) dy \right] \quad (\text{B.2})$$

where $E_j(x)$ and $E_j(y)$ are normalized. Including walkoff the signal coupling coefficient is

$$c_{oo}^s = \frac{2}{\pi w_s^2} \left[\int_{-\infty}^{\infty} dx \exp \left\{ -x^2 \left(\frac{2}{w_s^2} + \frac{1}{w_p^2} \right) - \frac{(x - \rho z)^2}{w_p^2} \right\} \right] \left[\int_{-\infty}^{\infty} dy \exp \left\{ -y^2 \left[\frac{2}{w_s^2} + \frac{2}{w_p^2} \right] \right\} \right] \quad (B.3)$$

where ρ is the walkoff angle. Integration yields,

$$c_{oo}^s = g_s \exp \left[- \frac{\pi}{4} \left(\frac{z}{\ell_w} \right)^2 \right] \quad (B.4)$$

where

$$\ell_w = \frac{\sqrt{\pi}}{2} \frac{w_p}{\rho} \sqrt{\frac{w_p^2 + w_s^2}{\frac{2}{w_p^2} + \frac{2}{w_s^2}}} \quad (B.5)$$

and

$$g_s = \frac{w_p^2}{w_p^2 + w_s^2} \quad (B.6)$$

For the idler, the result is,

$$c_{oo}^i = \exp \left[- \frac{\pi}{4} \left(\frac{z}{\ell_w} \right)^2 \right] \quad (B.7)$$

The polarization terms of Eq.(1) can now be re-written in terms of cavity mode field,

$$\frac{dE_s}{dz} + \alpha_s E_s = j \kappa_s g_s E_p E_i^* \exp \left(-\frac{\pi}{4} \frac{z^2}{\ell_w^2} \right) e^{j\Delta k z} \quad (B.8)$$

$$\frac{dE_i}{dz} + \alpha_i E_i = j \kappa_i E_p E_s^* \exp \left(-\frac{\pi}{4} \frac{z^2}{\ell_w^2} \right) e^{j\Delta k z} \quad (B.9)$$

Let

$$E_s = E'_s e^{-\alpha_s z}, \quad E_i = E'_i e^{-\alpha_i z} \quad (B.10)$$

Then

$$\frac{dE'_s}{dz} = i \kappa_s g_s E_p E_i'^* \exp \left(-\frac{\pi}{4} \frac{z^2}{\ell_w^2} \right) e^{j\Delta k z} \quad (B.11)$$

$$\frac{dE'_i}{dz} = i \kappa_i E_p^* E_s' \exp \left(-\frac{\pi}{4} \frac{z^2}{\ell_w^2} \right) e^{-j\Delta k z}$$

where $\alpha_s = \alpha_i \equiv \alpha$ is assumed. Let $\Delta k = 0$, since we are interested in a phasematched OPO. Then substitution yields,

$$\frac{d}{dz} \left[\exp \left(-\frac{\pi}{4} \frac{z^2}{\ell_w^2} \right) \frac{d}{dz} \right] E'_s = \kappa_s \kappa_i g_s |E_p|^2 \exp \left(-\frac{\pi}{4} \frac{z^2}{\ell_w^2} \right) E_s \quad (B.12)$$

Changing variables by letting

$$z' = \int_0^z \exp -\frac{\pi}{4} \frac{z''^2}{\ell_w^2} dz'' \quad (B.13)$$

yields

$$\frac{d^2 E_S'}{dz'^2} = \kappa_S \kappa_i g_S |E_p|^2 E_S' \quad (B.14)$$

The solution satisfying the boundary condition that $E_S' = E_S(0)$ and $E_i' = 0$ at $z' = 0$ is,

$$E_S(z) = E_S(0) e^{-\alpha_S z} \cosh \Gamma z' \quad (B.15)$$

where

$$\Gamma = \sqrt{\kappa g_S I_p} \quad (B.16)$$

with κ and I_p defined by

$$\kappa = \frac{2 \omega_S \omega_i d_{eff}^2}{n_S n_i n_p \epsilon_0 c^3}, \quad I_p = \frac{1}{2} n c \epsilon_0 |E_p|^2$$

The idler wave has the solution,

$$E_i(z) = E_S(0) e^{-\alpha_i z} \sqrt{\frac{\kappa_i}{g_i \kappa_S}} e^{-\frac{1}{2}j(\psi_p + 3\pi)} \sinh \Gamma z' \quad (B.17)$$

where ψ_p is the phase of the pump field.

APPENDIX C

Effective Nonlinear Coefficient for LiNbO_3

For LiNbO_3 with a point group symmetry of $\bar{3}m$, the effective nonlinear coefficient is⁴⁴

$$d_{\text{eff}} = d_{31} \sin \theta + d_{22} \cos \theta \quad (\text{C.1})$$

where θ is the angle between the optic axis and pump propagation direction. Also, $d_{22} = .53 d_{31}$.⁴⁵ So for $\theta = 47^\circ$, in the middle of the OPO tuning range, we have

$$d_{\text{eff}} = 1.09 d_{31} \quad (\text{C.2})$$

From 1.06 μm second harmonic generation measurements the recommended value of d_{31} given by Choy⁴⁶ is $5.95 \times 10^{-12} \text{ m/V}$. We scale this to the OPO wavelength range, by using the dispersionless Miller's Delta Δ_{ijk} value of 1.13×10^{-3} , where

$$\Delta_{ijk} = \frac{d_{ijk}}{\epsilon_o (n_s^2 - 1)(n_i^2 - 1)(n_p^2 - 1)} \quad (\text{C.3})$$

Using the measured indices of refraction for congruent LiNbO_3 ⁴⁷ we find

$$d_{\text{eff}} = 5.72 \times 10^{-12} \text{ m/V} \quad (\text{C.4})$$

APPENDIX D

Multiple Pass Diffraction Grating Resolution

In this Appendix we consider the multiple passed reflection of monochromatic light from a defraction grating and calculate the resulting angular halfwidth for the case in which a propagation length $2L$ is allowed between grating reflection. This distance permits diffraction to again broaden the grating-narrowed divergence angle and to establish a steady-state $\Delta\theta_D$ independent of further grating reflections.

Neglect for the present the effect of L and consider the normalized grating intensity function for infinitely narrow grooves as given by⁴⁸

$$\bar{I} = \frac{\sin^2 N\gamma}{N^2 \sin^2 \gamma} \quad (D.1)$$

where N is the number of illuminated grating grooves and γ is defined by

$$\gamma = \frac{\pi d}{\lambda} [\sin \theta_o + \sin(\theta_o + \Delta\theta)] \quad (D.2)$$

Here d is the groove spacing, θ_o is the incident angle relative to grating normal, and $\Delta\theta$ is the deviation of a reflected light ray from Littrow configuration. The grating resonance is defined by

$$\frac{2\pi d}{\lambda} \sin \theta_o = n\pi \quad (D.3)$$

where n is an integer. If $\Delta\theta \ll 1$, we then find that

$$\gamma = \frac{\pi d}{\lambda} \cos \theta_0 \Delta\theta \quad (\text{D.4})$$

After p reflections the grating intensity function becomes

$$\bar{I}(p) = \left[\frac{\sin^2 \mathcal{N}\gamma}{(\mathcal{N}\gamma)^2} \right]^p \quad (\text{D.5})$$

We define the angular halfwidth of the grating to be the angular deviation from resonance $\Delta\theta_D$ which reduces the grating intensity function to $1/e^2$ of its maximum. A numerical calculation using Eq.(D.5) shows that to a good approximation

$$\mathcal{N}\gamma \doteq \frac{2}{\sqrt{p}} \quad (\text{D.6})$$

for $p \gg 1$. The angular halfwidth of a grating narrowed light packet is then, from Eq.(D.4) and (D.6),

$$\Delta\theta_D = (\lambda/\pi W) 1/\sqrt{p} \quad (\text{D.7})$$

where W is the $1/e^2$ spot radius and $\mathcal{N} = 2W/d$ has been used. The far field diffraction limited divergence angle is then reduced by $1/\sqrt{p}$ for a multi-passed grating.

The propagation length $2L$ is now included to calculate the effect of diffraction. For a Gaussian beam, the divergence angle $\theta_{\frac{1}{2}}$ is $w(z)/R(z)$ where $w(z)$ is the spot size and $R(z)$ is the beam curvature.⁴⁹ We have then

$$\theta_{\frac{1}{2}} = \frac{\lambda}{\pi w_0} \sqrt{1 + \left(\frac{z_R}{z}\right)^2} \quad (D.8)$$

where z_R is the Rayleigh range $\pi w_0^2/\lambda$. If beam expansion prisms are used, this angle is reduced by $1/M_a$. Since $w_s = w_s/M$ we obtain

$$\theta_{\frac{1}{2}} = \frac{\lambda}{\pi w_s} \frac{M}{M_a} \sqrt{1 + \left(\frac{z_R}{2L}\right)^2} \quad (D.9)$$

We are interested in the steady state condition which must occur for some p' . We may approximately write,

$$\frac{\lambda}{\pi w_s} \left[\frac{1}{\sqrt{p' + 1}} + \frac{M/M_a}{\sqrt{1 + (z_R/2L)^2}} \right] = \frac{\lambda}{\pi w_s} \frac{1}{\sqrt{p'}} \quad (D.10)$$

where L is the cavity optical length. Assuming $p' > 1$ yields

$$4 p'^2 (p' + 1) \cong \left(\frac{M_a}{M}\right)^2 \left[1 + \left(\frac{z_R}{2L}\right)^2 \right] \quad (D.11)$$

Therefore

$$p' \approx \left(\frac{M_a}{M} \frac{z_R}{4L} \right)^{2/3} \quad (D.12)$$

If Eq.(D.11) is less than unity we set $p' = 1$. For $w_s = 0.6$ mm, $\lambda_s = 1.9$ μ m, $L = 15$ cm and 5 x prisms, $p' = 3$. This is much less than the transits possible during the OPO buildup time, $ct/2L$. Thus the same diffractive process which stabilizes the spot size evolution in Appendix A is also responsible for the rapid stabilization of the diffraction limited halfwidth to the steady state value

$$\Delta \theta_D = \left(\frac{M}{M_a} \frac{4L\lambda}{\pi w_s^2} \right)^{1/3} \frac{\lambda_s}{\pi w_s} \quad (D.13)$$

We also need to understand the mechanism of the ejection of off-resonant wavelengths from a grating mirror cavity of center wavelength λ_s and grating angle θ_o . If $\lambda = \lambda_o + \Delta \lambda$ the grating equation becomes

$$\sin \theta' + \sin \theta'' = \frac{m\lambda}{d} \quad (D.14)$$

where d is the groove spacing, and for pass n

$$\theta' = \theta_o - \Delta_{n-1}, \quad \theta'' = \theta_o + \Delta_n$$

where θ' and θ'' are the incident and exit angles relative to the grating normal. Expansion of Eq.(D.13) yields

$$\Delta_n = \Delta_{n-1} + \frac{mN(\Delta \lambda)}{\cos \theta_o} \quad (D.14)$$

For the resonant wavelength λ_0 , the grating acts as a simple mirror. For a wavelength deviation $\Delta\lambda$, the grating reflection angle, relative to the cavity axis, is incremented by $m\lambda/d \cos \theta$ on each pass. If we take $\Delta_0 = 0$,

$$\Delta_n = \left(\frac{m\lambda \Delta\lambda}{d \cos \theta_0} \right) n \quad (D.15)$$

APPENDIX E

Brewster Angle Beam Expansion Prisms

Consider the two prism beam expanders shown in Fig.13
The linear magnification of a single prism is given by

$$M = \frac{\cos \theta_e}{\cos \theta_i} \quad (E.1)$$

where θ_i and θ_e are the angles of incidence and exit from the prism first surface. The maximum magnification occurs when the beam exits normal to the prism second surface. Then $\theta_e = \alpha$, where α is the prism apex angle and Snell's law results in

$$M = \frac{1}{n} \frac{\tan \theta_i}{\tan \alpha} \quad (E.2)$$

For low insertion loss the incident angle is set at Brewster's angle so that

$$n = \tan \theta_i \quad (E.3)$$

and

$$M = \frac{1}{\tan \alpha} = n \quad (E.4)$$

Therefore, near Brewster's angle

$$M \cong \tan \theta_i \quad (E.5)$$

The angular magnification for a prism beam expander is found by differentiating Snell's law

$$\delta \theta_i \cos \theta_i = n \cos \theta_e \delta \theta_e \quad (\text{E.6})$$

so that

$$\frac{\delta \theta_e}{\delta \theta_i} = \frac{1}{n} \frac{\cos \theta_i}{\cos \theta_e} \quad (\text{E.7})$$

Using Eqns.(E.1) and (E.4), we have for a Brewster angle prism,

$$\frac{1}{M_a} \cong \frac{\delta \theta_e}{\delta \theta_i} = \frac{1}{nM} \cong \frac{1}{n^2} \quad (\text{E.8})$$

Therefore,

$$M_a = M_n \cong M^2 \quad (\text{E.9})$$

For comparison, a telescope has an angular magnification of

$$M_a = M \quad (\text{E.10})$$

The minimum optical path length ℓ_o through a prism is given by

$$\ell_o = n W \tan \alpha \cong W \quad (\text{E.11})$$

The two prism expander is nearly achromatic. The angular deviation $\Delta\theta$ for an index dispersion Δn is to first order

$$\Delta\theta = (1/n_o - 1/n_o^2) \Delta n \quad (\text{E.12})$$

where n_o is the mean index of refraction of the medium. For glass prisms the angular deviation is only 2.7 mrad over the entire visible spectrum.

The insertion loss of the prisms is given by the Fresnel reflection loss at the first surface plus the anti-reflection coating loss at the near normal surface. For the LiNbO_3 prisms this loss is less than 1% per prism, which is insignificant compared to output coupling losses. Thus the LiNbO_3 prisms beam expander is readily inserted into the OPO cavity without significantly increasing threshold.

APPENDIX F

Experimental Cavity Configurations

In the course of this work, a number of OPO configurations have been constructed in an effort to reduce threshold and to improve linewidth performance. We have found that the Gaussian pump profile is necessary for minimum threshold due to the longer walkoff length. Attempts to improve performance have concentrated on a reduction of cavity length, as shown by the in-line arrangements using Fresnel pump coupling (Fig. 14a) and using a dichroic input/output separation mirror (Fig. 14b). The latter is necessarily a DSRO but has the disadvantage that for moderate pump levels the signal wave feedback from the pump high reflector mirror is sufficient for oscillation. In the Fresnel coupled cavity, the pump is reflected off the first prism surface. This arrangement works well but is somewhat inconvenient to align and does not efficiently couple the pump beam into the cavity. The L-shaped cavity using a dichroic input mirror shown in Fig. 10, performs better than any other configuration we have tested.

For linewidth control we have operated cavities with a Galilean telescope expander (Fig. 14c), a mirror/grating combination rear reflector (Fig. 14d) and a Brewster angle birefringent tuning element (Fig. 14e). The telescope expander is difficult to align

and to collimate. It also suffers from chromatic aberration and produces back reflected focal spots which may damage other components. The resonant mirror/grating setup must be interferometricly stable to operate properly. Birefringent tuning has the disadvantage of being nonlinear. We find that the diffraction grating when preceeded by a prism beam expander has better performance than any other configuration tested.

ACKNOWLEDGEMENTS

We want to acknowledge the contributions of R.A. Baumgartner during the early part of this work and the support provided by A.R.O., A.F.O.S.R., and N.S.F.

REFERENCES

1. J.A. Giordmaine, R.C. Miller, "Tunable Coherent Parametric Oscillation in LiNbO_3 at Optical Frequencies", Phys. Rev. Letts. vol. 14, p.973-976, 1965.
2. S.E. Harris, "Tunable Optical Parametric Oscillators", Proc. IEEE, vol. 57, p.2096-2113, 1969.
3. R.L. Byer, "Optical Parametric Oscillators", Treatise in Quantum Electronics, H. Rabin and C.L. Tang, ed. Academic Press, p.587-702, 1973.
4. R.G. Smith, "Optical Parametric Oscillators", in Lasers, A.K. Levine, A.J. DeMaria, eds. Marcel Dekker, Inc., New York, 1976, p.189-307.
5. R.L. Byer, R.L. Herbst, R.S. Feigelson and W.L. Kway, "Growth and Application of (01.4) LiNbO_3 ", Opt. Commun. vol. 12, p.427-429, 1974.
6. R.L. Herbst, R.N. Fleming and R.L. Byer, "A 1.4 - 4.0 μm High Energy Angle Tuned LiNbO_3 Parametric Oscillator", Appl. Phys. Letts. vol. 25, p.520-522, 1974.
7. R.L. Byer, R.L. Herbst, R.N. Fleming, "A Broadly Tunable IR Source", Proc. Second International Conference on Laser Spectroscopy, Megeve, France, 1975, Springer-Verlag, 1975, p.206-226.

8. T. Henningsen, M. Garbuny and R.L. Byer, "Remote Detection of CO by Parametric Tunable Laser", Appl. Phys. Letts. vol. 24, p.242-244, 1974.
9. R.A. Baumgartner and R.L. Byer, "Remote SO₂ Measurements at 4 μ m with a Continuously Tunable Source", Optics Letts. vol. 2, p.163-165, 1978.
10. A. Kung and C.B. Moore, to be published.
11. A.Kaldor, R. Rabinowitz, D.M. Cox, J.A. Horsley and R. Brickman, "Laser Chemistry Experiments with UF₆", invited paper at 10th International Quantum Electronics Conference, Atlanta, Georgia, June 1978.
12. R.A. Baumgartner and R.L. Byer, "Optical Parametric Amplification", to be published .
13. L.W. Casperson, S.D. Lunnam, "Gaussian Modes in High Loss Laser Resonators", Appl. Opt. vol. 14, p.1193-1199, 1975.
14. H. Kogelnik, "Coupling and Conversion Coefficients for Optical Modes", in Proc. of Symposium on Quasi-Optics, Polytechnic Press, Brooklyn, 1964, vol. 14, p.333-347.
15. G.D. Boyd, A. Ashkin, "Theory of Parametric Oscillator Threshold with Single Mode Optical Masers and Observation of Amplification in LiNbO₃", Phys. Rev. vol. 146, - 198, 1966.

16. R. Asby, "Optical Mode Interaction in Nonlinear Media", Phys. Rev. vol. 187, p.1062-1069, 1969.
17. R.L. Byer, S.E. Harris, "Power and Bandwidth of Spontaneous Parametric Emission", Phys. Rev. vol. 168, p.1064-1068, 1968.
18. J.E. Bjorkholm, "Some Effects of Spatially Nonuniform Pumping in Pulsed Optical Parametric Oscillators", Journ. Quantum Electronics, vol. OE-7, p.109-118, 1971.
19. R.L. Herbst, H. Komine, R.L. Byer, "A 200 mJ Unstable Resonator Nd:YAG Oscillator", Optics Commun. vol. 21, p.5-7, 1977.
20. The crystals tested were from the Stanford Center for Materials Research and from Crystal Technology Inc., Mountain View, California.
21. R.L. Byer, "Parametric Oscillators" in Tunable Lasers and Applications, A. Mooradian, T. Jasper, P. Stokseth, eds. Springer-Verlag, 1976, p.76-80.
22. G.M. Zverev, E.A. Lervhuk, V.A. Pashkov, Yu.P. Poryadin, "Laser-Radiation-Induced Damage to the Surface of Lithium Niobate and Tantalate", Soviet Journal of Quantum Electronics, vol. 2, p.167-169, 1972.
23. G.M. Zverev, E.A. Levchuk, V.A. Pashkov, Yu D. Poryadin, "Damage to the Surface of Lithium Niobate by Light", Soviet Phys. JETP, vol. 35, p.165-167, 1972.

24. G.M. Zverev, S.A. Kolyadin, E.A. Levchuk and L.A. Skvortsov, "Influence of the Surface Layer on the Optical Strength of Lithium Niobate", Soviet Journal of Quantum Electronics, vol. 7, p.1071 - 1075, 1977.
25. M.M. Choy, private communication.
26. J.D. Venables, "Damage-induced Microdomains in LiTaO_3 ", Appl. Phys. Letts. vol. 25, p.254-256, 1974.
27. N. Ohnishi, T. Iizuka, "Etching Study of Microdomains in LiNbO_3 Single Crystals", Journ. Appl. Phys. vol. 46, p.1063-1067, 1975.
28. E.S. Bliss, "Pulse Duration Dependence of Laser Damage Mechanisms", Opto-Electronics, vol. 3, p.99-108, 1971.
29. Measurement initially done by T.Henningsen, private communication and later repeated in this laboratory by M. Endemann, as described in text.
30. R.W. Wallace, private communication.
31. B.R. Suydam, "Self-focusing of Very Powerful Laser Beams. in Laser Induced Damage in Optical Materials, A.J. Glass and A.H. Guenther, eds. Washington D.C. N B S Special Publication 387, p.42-48. 1973.

32. B.R. Suydam, "Self-focusing of very Powerful Laser Beams, II", Journ. Quant. Electronics, vol . QE-10, p.837-843, 1974.
33. E.L. Kerr, "Filamentary Tracks Formed in Transparent Optical Glass by Laser Beam Self-focusing. II, Theoretical Analysis", Phys. Rev. A, vol. 4, p.1195-1218, 1971.
34. N.L. Boling, A.J. Glass, A. Owyong, "Empirical Relationships for Predicting Nonlinear Refractive Index Changes in Optical Solids", Journ. Quant. Elect. vol. QE-14, p.601-608, 1978.
35. J. Pinard, J.F. Young, "Interferometric Stabilization of an Optical Parametric Oscillator", Opt. Commun. vol. 4, p.425-427, 1972.
36. R.W. Wallace, Chromatix Inc., private communication.
37. R.L. Byer, R.L. Herbst, "Parametric Oscillation and Mixing", in Nonlinear Infrared Generation, Y.R. Shen, ed. Springer-Verlag, 1977 , p.81-137.
38. S.A. Myers, "An Improved Line Narrowing Technique for a Dye Laser Excited by a Nitrogen Laser", Opt. Commun. vol. 14, p.187-9, 1971. Also in, D.C. Hanna, P.A. Karkhainen, R. Wyatt, "A Simple Beam Expander for Frequency Narrowing of Dye Lasers", Opt. and Quantum Electronics, vol. 7, p.115-119, 1975.

39. G.K. Klauminzer, "New High Performance Short Cavity Dye Laser Design", Post Deadline Paper at Conference on Laser Engineering and Applications, Washington D.C. 1977.
40. P.W. Smith, "Stabilized, Single-frequency Output from a Long Laser Cavity", Journ. Quant. Electron. vol. QE-1, p.343-348, 1965.
41. M. Hercher, "Tunable Single Mode Operation of Gas Lasers Using Intracavity Tilted Etalons", Appl. Opt. vol. 8, p.1103-1106, 1969.
42. W.R. Leeb, "Losses Introduced by Tilting Intracavity Etalons", Appl. Phys. vol. 6, p.267-272, 1975.
43. H. Daussey, R. Dumanchin, O. deWitte, "Fabry-Perot with Short Pulse Laser: Spectral Selection and Spectral Analysis in Dye Lasers", Appl. Opt. vol. 17, P.451-458, 1978.
44. J.F. Midwinter, J. Warner, "The Effects of Phase Matching Method and of Uniaxial Crystal Symmetry on the Polar Distribution of Second Order Nonlinear Optical Polarization", British Journ. of Appl. Phys. vol. 16, p.1135-1142, 1965
Orientation is chosen so $\phi = 90^\circ$.
45. G.D. Boyd, R.C. Miller, K. Nassau, W.L. Bond and A. Savage, "LiNbO₃: An Efficient Phase-matachable Nonlinear Optical Material", Appl. Phys. Letts. vol. 5, p.234-236, 1964.

46. M.M. Choy, R.L. Byer, "Accurate Second Order Susceptibility Measurements of Visible and Infrared Nonlinear Crystals", Phys. Rev. B, vol. 14, p.1693-1706, 1976.
47. D.S. Smith, H.D. Riccius and R.P. Edwin, "Refractive Indices of Lithium Niobate", Opt. Commun. vol. 17, p.332-335, 1976.
48. M. Born, and E. Wolf, Principles of Optics, 4th ed, (Pergamon Press, 1970), p.404.
49. H. Kogelnik, T. Li, "Laser Beams and Resonators", Proc. IEEE, vol. 54, p.1312-1329, 1966.

FIGURE CAPTIONS

1. Simplified OPO schematic. Mirror M_1 is highly reflecting between 1.4 - 2.1 μm . Output coupler M_2 has signal reflectance R . For DSRO operation, pump high reflector M_3 may be used.
2. Angle tuned LiNbO_3 OPO tuning curve and crystal gain bandwidth.
3. SRO threshold fluence vs cavity physical length solid curve shows results of numerical calculation. Dashed curve shows results of square pulse model. $\ell = 6 \text{ cm}$, $2 w_p = 4 \text{ mm}$, $R = 60\%$, $\tau = 15 \text{ ns}$.
4. SRO threshold fluence vs crystal length. $L' = 8 \text{ cm}$, $2 w_p = 4 \text{ mm}$, $R = 60\%$, $\tau = 15 \text{ ns}$.
5. SRO threshold fluence vs signal wave reflectance. Error bars reflect variations due to differing idler reflectances. $L' = 8 \text{ cm}$, $\ell = 6 \text{ cm}$, $2 w_p = 4 \text{ mm}$, $\tau = 15 \text{ ns}$.
6. SRO threshold fluence vs pump spot diameter $L' = 8 \text{ cm}$, $\ell = 6 \text{ cm}$, $R = 60\%$, $\tau = 15 \text{ ns}$.
7. SRO threshold fluence vs pump pulsewidth. Data scaled by 0.37. $L' = 8 \text{ cm}$, $\ell = 6 \text{ cm}$, $2 w_s = 4 \text{ mm}$, $R = 50\%$.
8. SRO energy conversion efficiency vs number of times above threshold.

9. Damage limits of LiNbO_3 vs pump pulsewidth. a) solid curve shows pump fluence at 3 x OPO threshold for an average crystal. Surface damage fluences for the bare LiNbO_3 surface, for the uncoated surface in an O_2 atmosphere, for an SiO_2 coated crystal are shown, b) solid curve shows pump intensity at 3 x OPO threshold inside an average crystal. An approximate experimental self-focusing damage limit is indicated by the dashed line.
10. Schematic of the SRO cavity for linewidth studies. Primary linewidth control is provided by prisms and grating combination. Line narrowing is accomplished with a tilted etalon. A resonant reflector used as an output coupler collapses the linewidth to a single axial mode.
11. SRO grating linewidth using a ten power prism beam expander as measured using a scanning 1 meter spectrometer.
12. SRO linewidth measurements using Fabry-Perot etalon. OPO cavity includes a tilted etalon and resonant reflector, a) resonant reflector is misaligned, producing a FWHM linewidth of $.075 \text{ cm}^{-1}$, or 3 axial modes, b) resonant reflector is aligned, producing stable single axial mode operation.
13. Two prism expander setup. Incident and exit angles are shown as θ_i and θ_e . Prisms apex angle is α . Magnification is given by W/w .

14. OPO cavity configurations, a) pump input coupling using Fresnel reflection of prisms P, b) M_2 is pump high reflector, dichroic beamsplitter BS is used to separate signal output, c) telescope T used for beam expansion, d) partially reflecting signal mirror M_3 to act with grating G as resonant reflector, e) birefringent filter BF used as line-narrowing element, M_4 is signal high reflector. Other elements: crystal = XT, output coupler = M_1 .

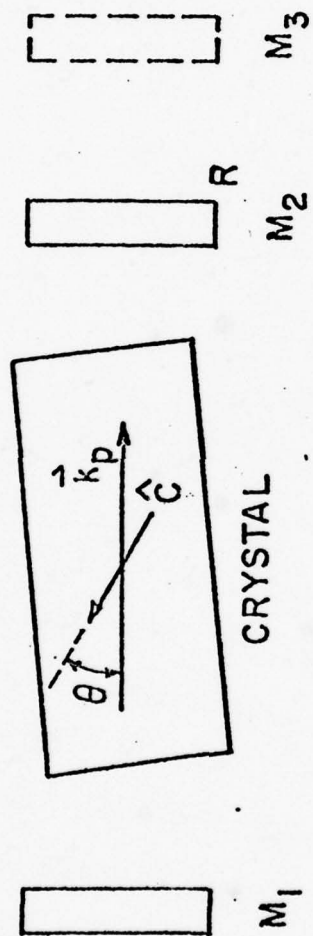


FIGURE 1

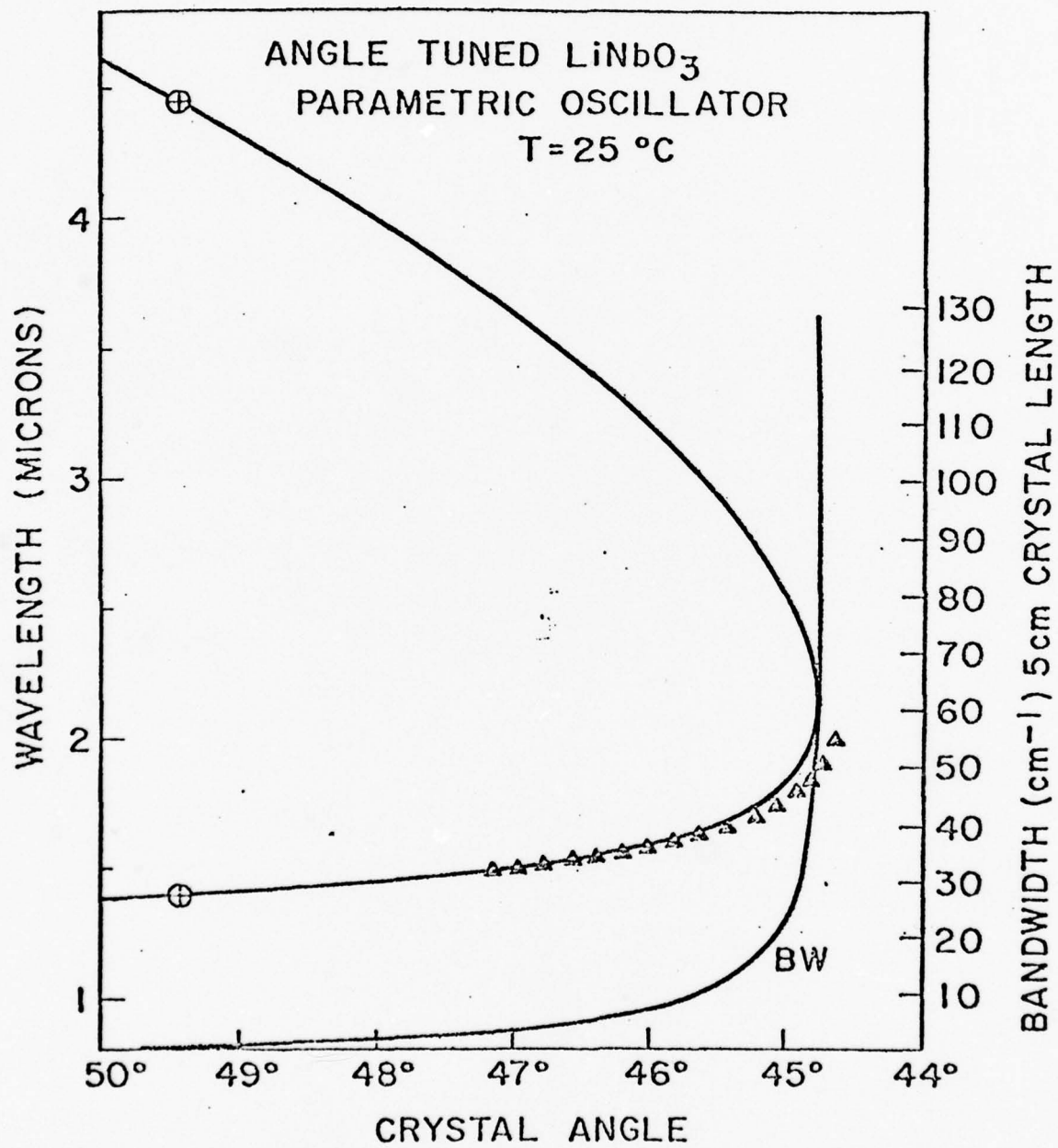


FIGURE 2

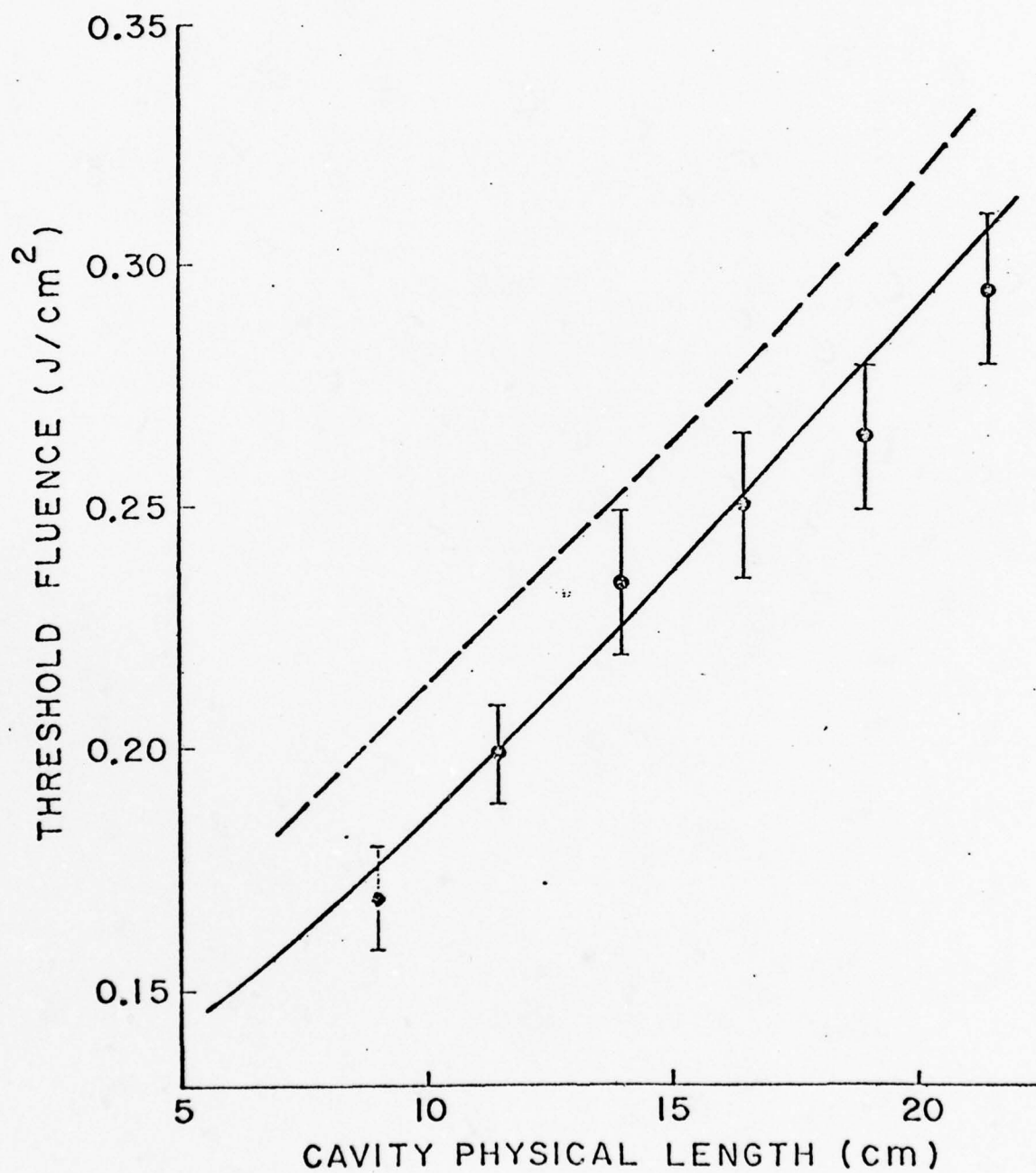


FIGURE 3

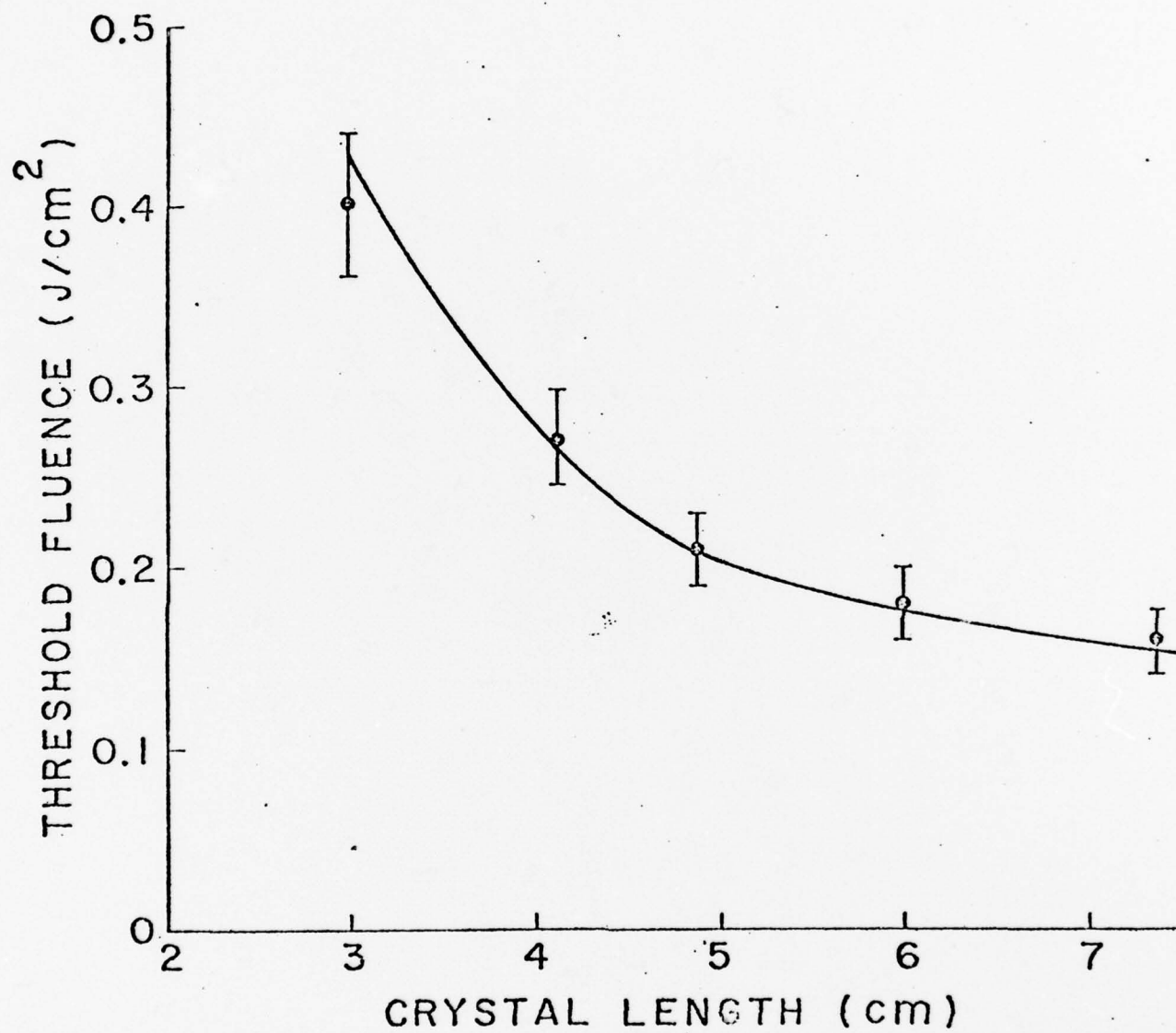


FIGURE 4

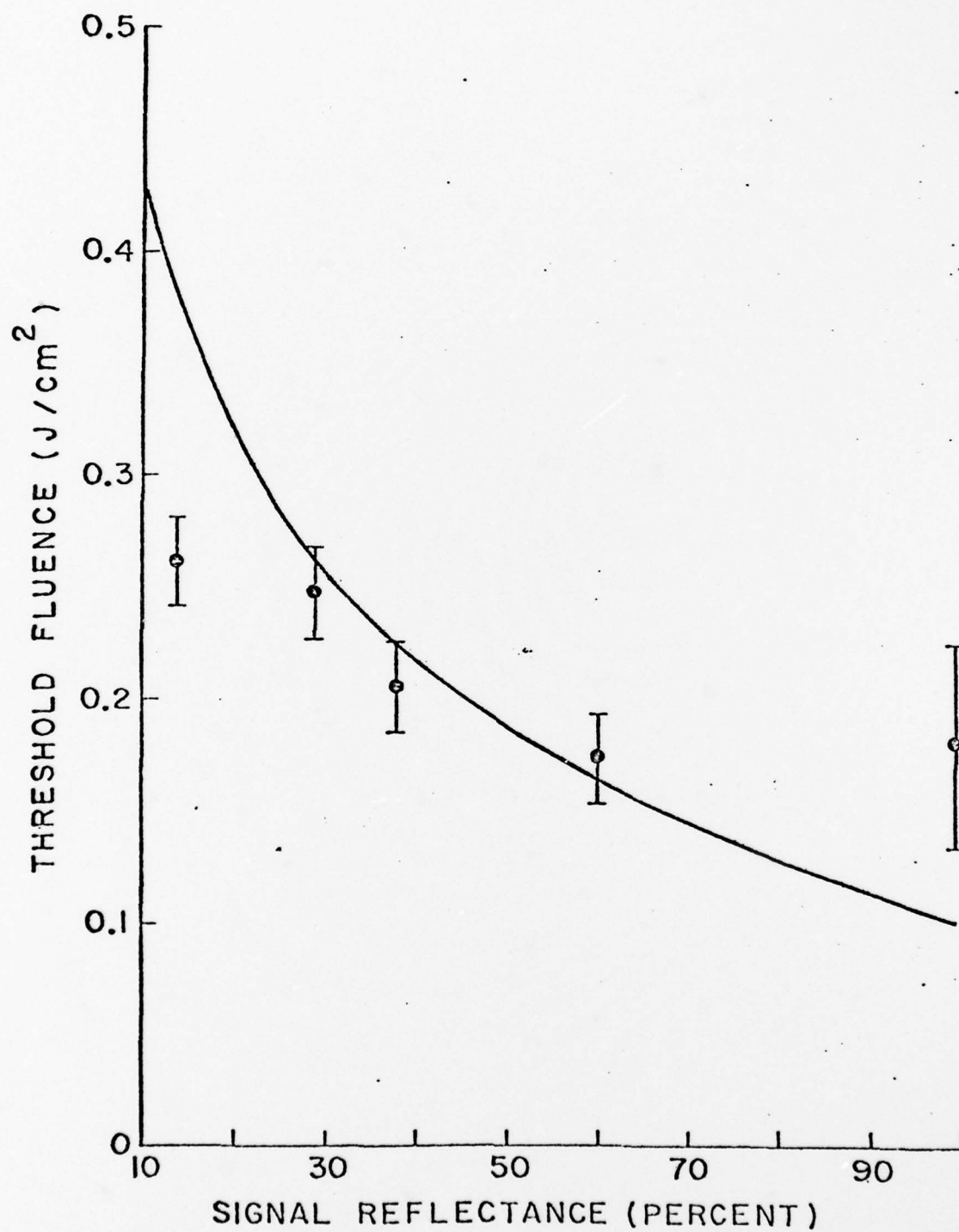


FIGURE 5

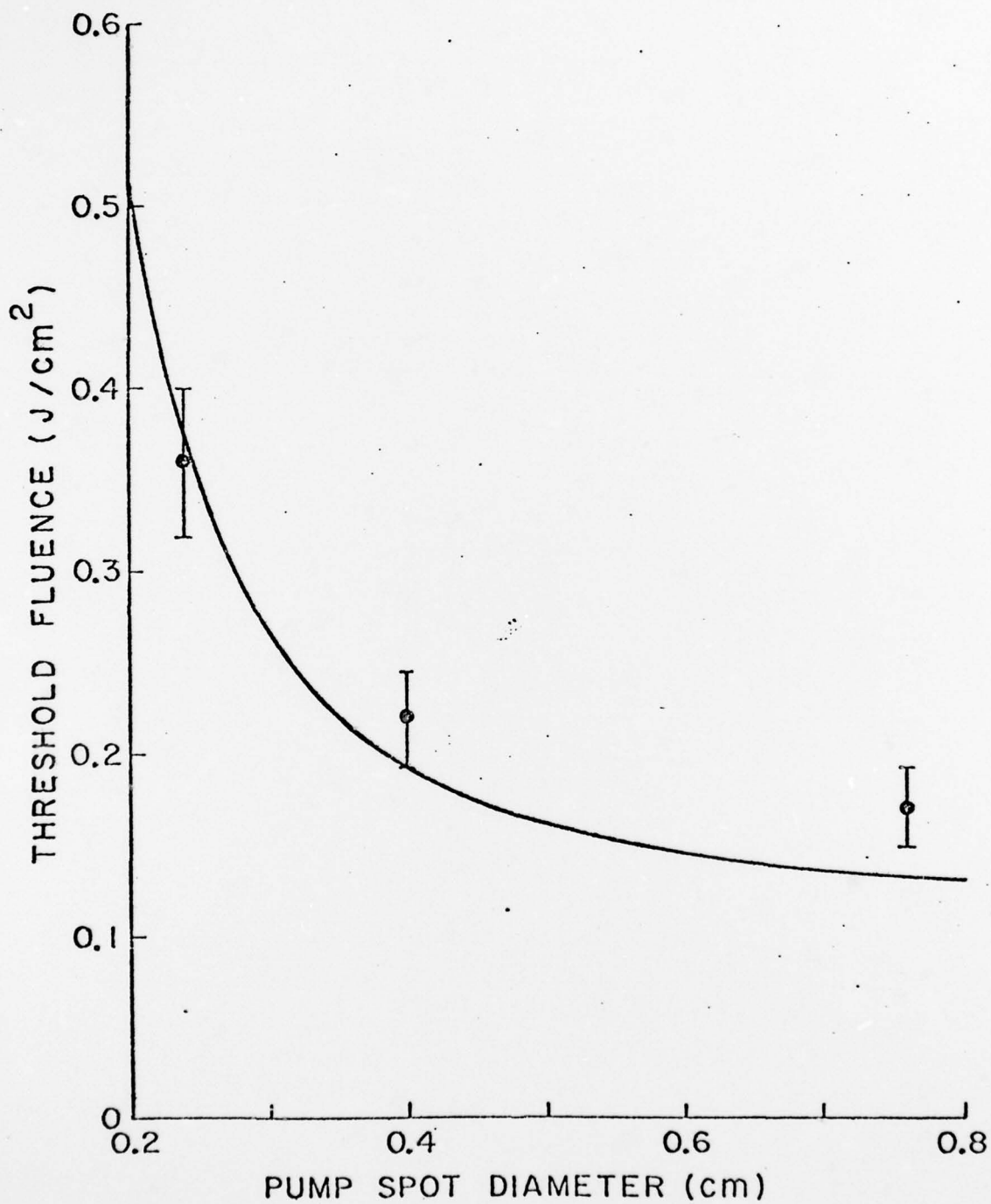


FIGURE 6

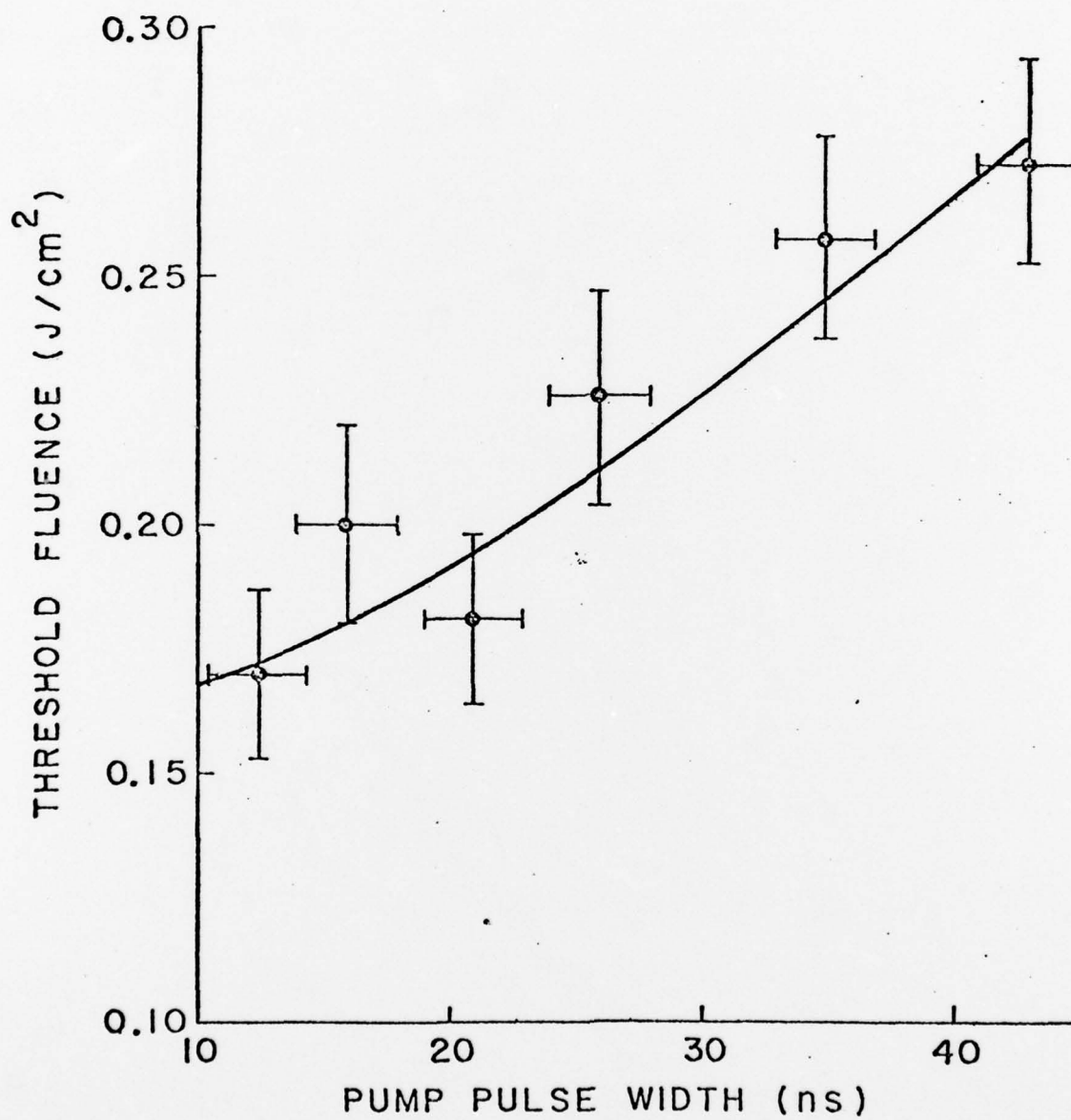


FIGURE 7

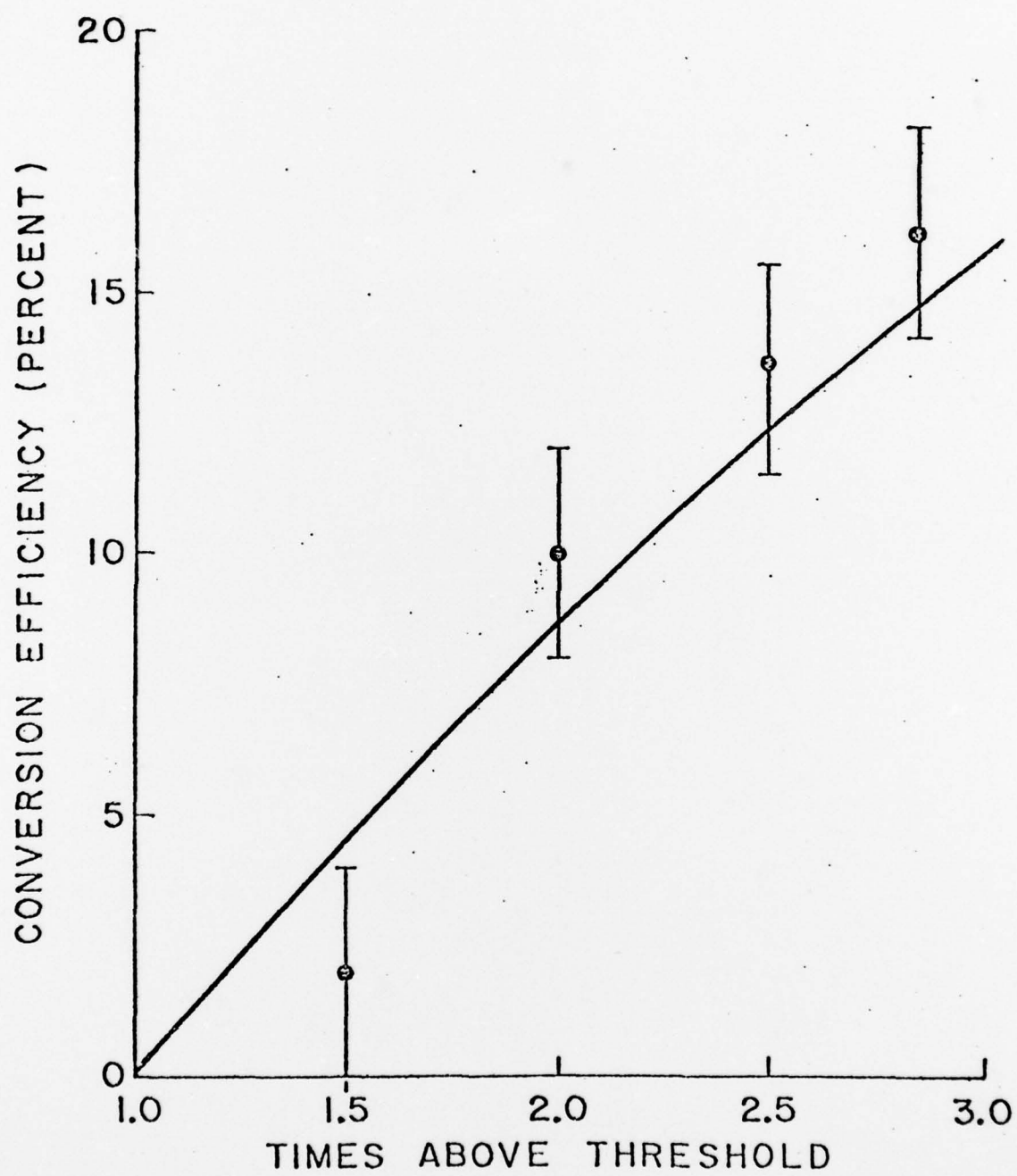


FIGURE 8

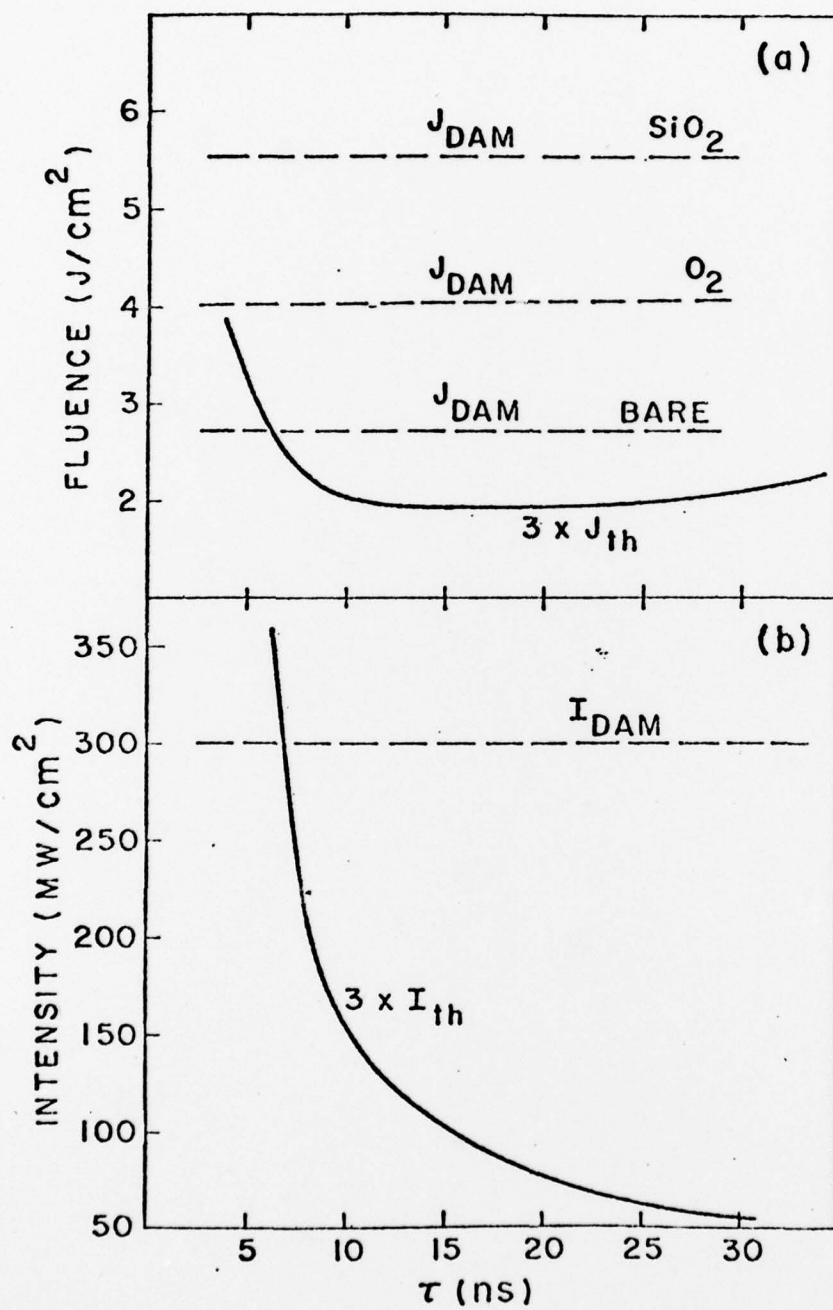


FIGURE 9

OPO LINEWIDTH CONTROL

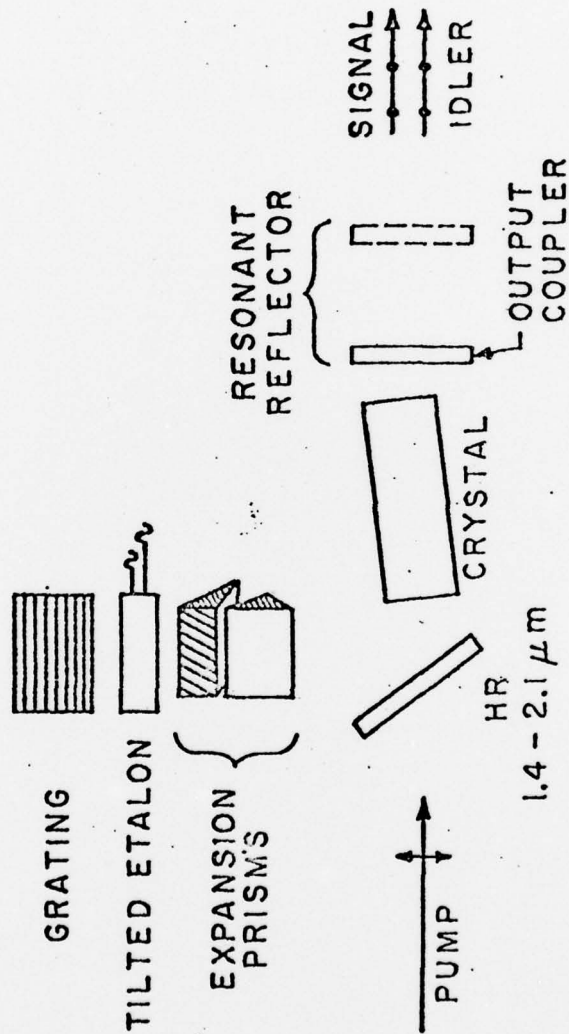


FIGURE 10

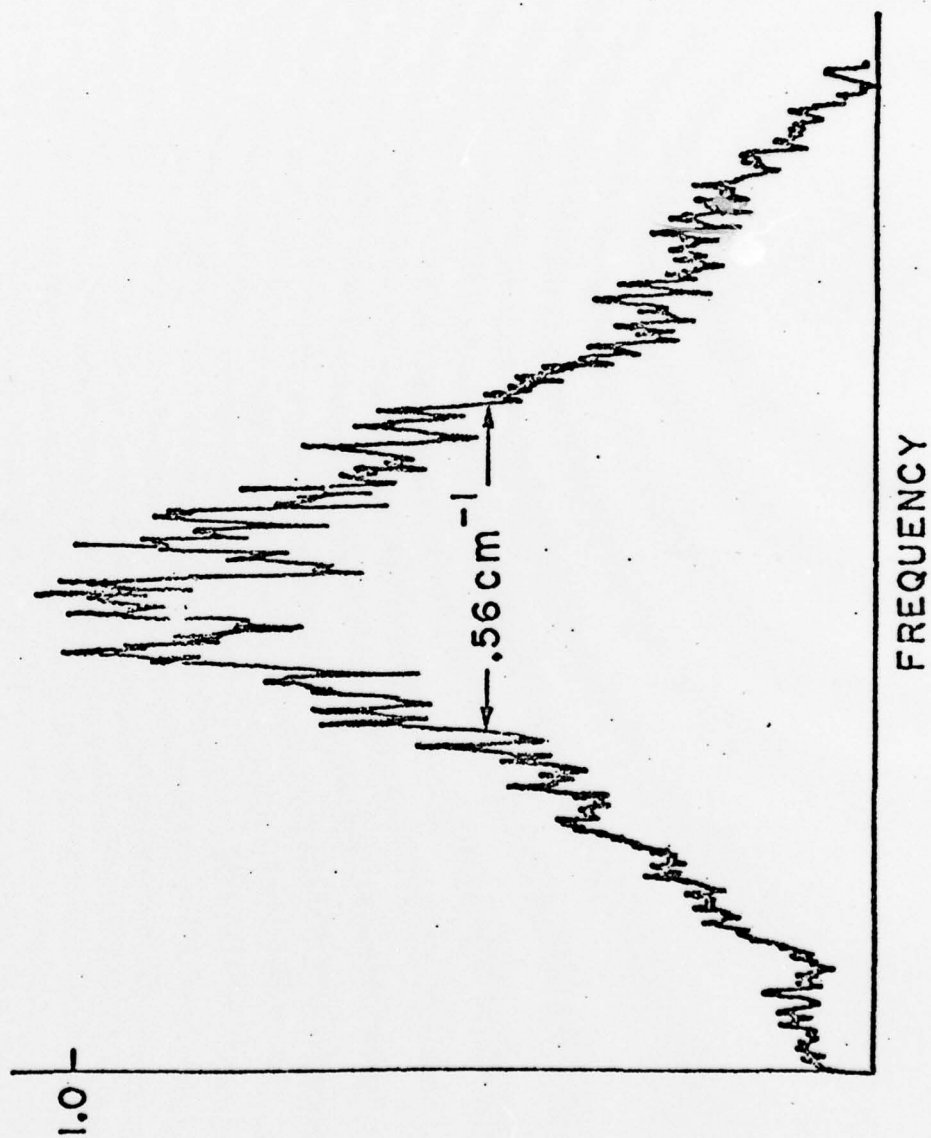
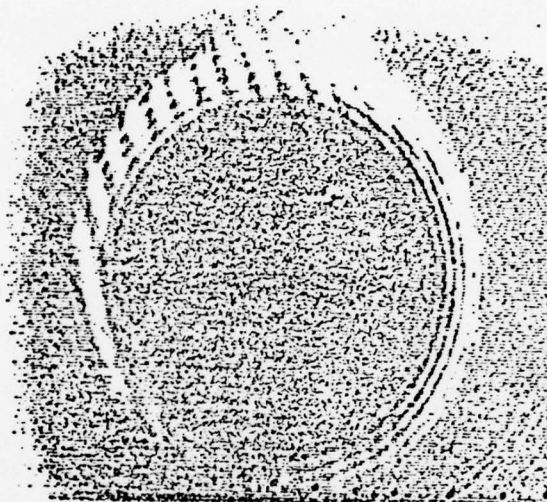
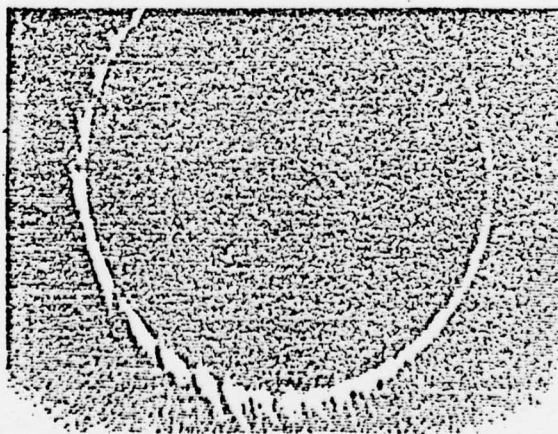


FIGURE 11



(a)



(b)

FIGURE 12

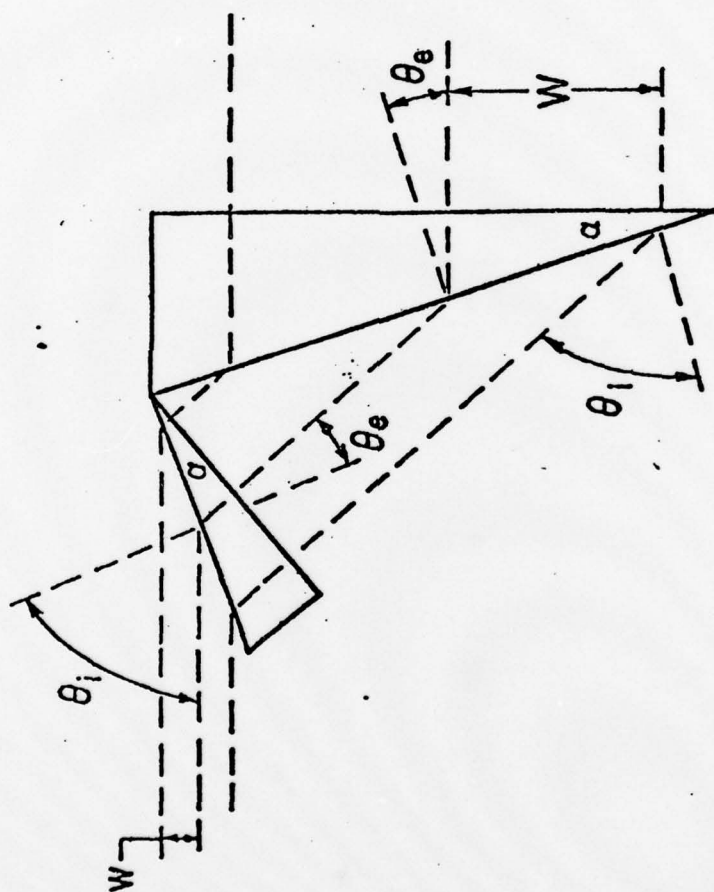


FIGURE 13

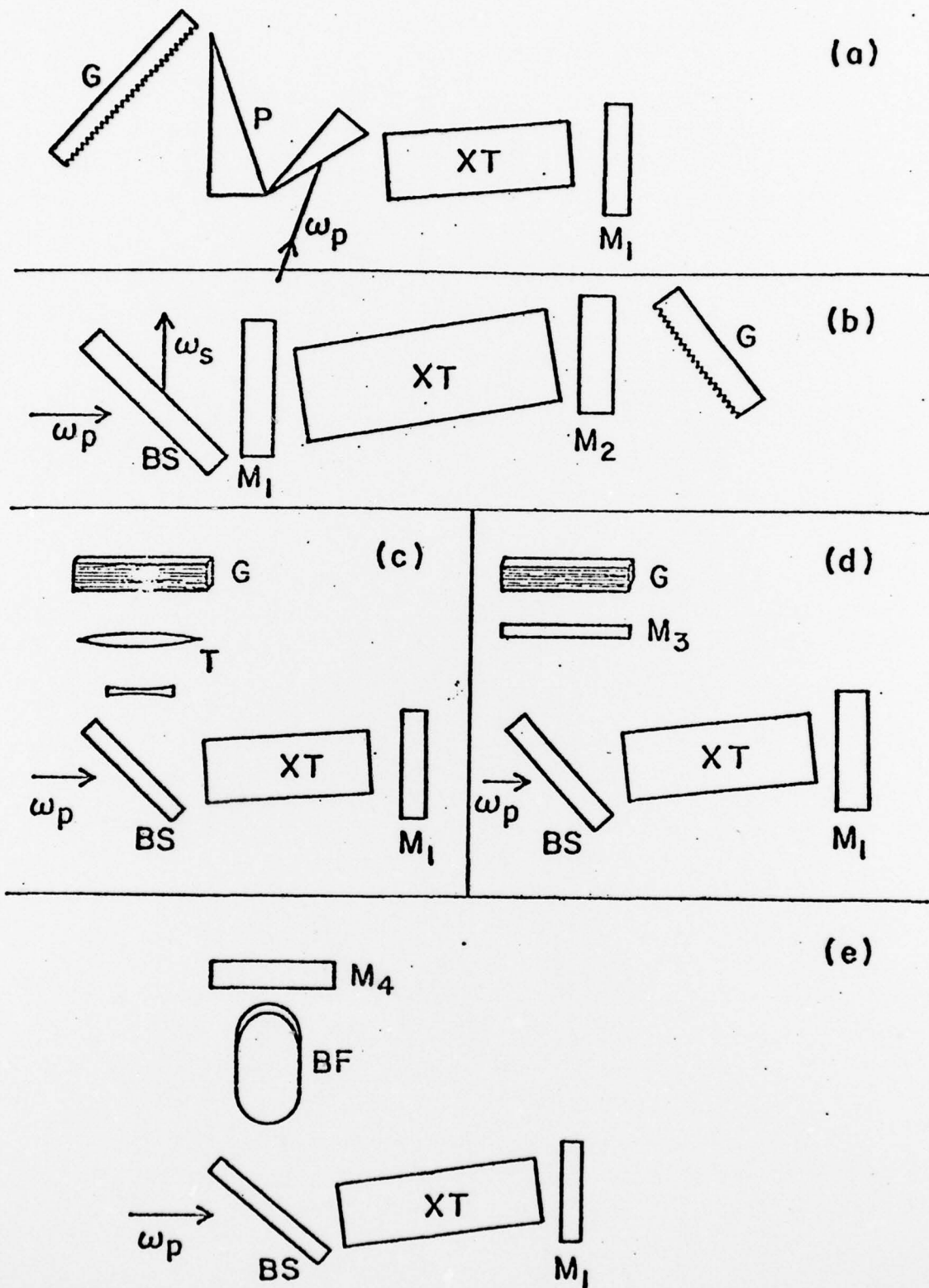


FIGURE 14

APPENDIX IV

Robert L. Byer and W. R. Trutna, "16- μ m Generation by CO₂-
Pumped Rotational Raman Scattering in H₂ .

16- μm generation by CO₂-pumped rotational Raman scattering in H₂

Robert L. Byer and W. R. Trutna

Edward L. Ginzton Laboratory of Physics, Stanford University, Stanford, California 94305

Received July 5, 1978

We have generated 50 mJ of 16.9- μm radiation by stimulated rotational Raman scattering in 3 atm of H₂ gas pumped by a CO₂ TEA-laser source. Threshold was reached by injection of a few microjoules of 16.9- μm radiation generated by four-wave mixing. We achieved 25% peak power, or 40% peak photon conversion efficiency.

In 1976 Byer proposed using stimulated rotational Raman scattering in hydrogen gas as an efficient method of frequency conversion in the infrared.¹ In particular, it was noted that stimulated Raman scattering in *para*-H₂ gas with a CO₂ laser pump generates 16- μm radiation, which is of potential use for UF₆ isotope enrichment. It was subsequently learned that others have also suggested stimulated rotational Raman scattering in the infrared.² Recently Frey *et al.*³ have generated 16- μm output at the 1-mJ level by vibrational Raman scattering in H₂ and N₂ pumped by a ruby-pumped dye laser.

We have successfully generated 50 mJ of 16.9- μm radiation by four-wave mixing-assisted stimulated rotational Raman scattering. We used a 2-J, 70-nsec CO₂ laser source to pump a 25-pass, 4-m-long cell filled with 3 atm of *p*-H₂ gas obtained from a liquid H₂ source. Based on theoretical calculations¹ and rotational Raman threshold, scaled from careful measurements at 1.064 μm , we predicted a CO₂-pumped rotational Raman threshold in our multipass cell of 1.7–2.6 J in a 70-nsec gain-switched pulse. Our available CO₂ pump energy was not adequate to reach stimulated Raman threshold by amplification of spontaneous emission. However, when 16.9- μm radiation generated by four-wave mixing was injected into the multipass cell, the Raman gain was sufficient to lead to significant pump depletion and a peak photon conversion efficiency of 40% to the Stokes wave at 16.9 μm .

The four-wave mixing process was first described for interactions in crystals⁴ and later extended to gases^{5,6} as a means for generating widely tunable infrared radiation.⁷ Sorokin *et al.*⁸ have demonstrated four-wave mixing in H₂ gas using a CO₂ laser source as a method for 16- μm generation.

The equations governing both four-wave mixing and stimulated Raman scattering are given by⁹

$$\frac{\partial E_p}{\partial z} = -\frac{\omega_p}{2cn_p} \chi_R''(|E_s|^2 E_p + E_i E_o^* E_s e^{i\Delta k z}), \quad (1a)$$

$$\frac{\partial E_s}{\partial z} = +\frac{\omega_s}{2cn_s} \chi_R''(|E_p|^2 E_s + E_i^* E_o E_p e^{-i\Delta k z}), \quad (1b)$$

$$\frac{\partial E_i}{\partial z} = -\frac{\omega_i}{2cn_i} \chi_R''(|E_o|^2 E_i + E_p E_s^* E_o e^{-i\Delta k z}), \quad (1c)$$

$$\frac{\partial E_o}{\partial z} = +\frac{\omega_o}{2cn_o} \chi_R''(|E_i|^2 E_o + E_p^* E_s E_i e^{i\Delta k z}), \quad (1d)$$

where $\omega_p - \omega_s = \omega_i - \omega_o$ with $\omega_p - \omega_s = \omega_R$ and $\Delta k = -(k_p - k_s) + (k_i - k_o)$ with ω_R the characteristic Raman frequency of the medium with a peak Raman susceptibility χ_R'' .⁹ In our case E_p is the Nd:YAG pump field at 1.064 μm , E_s is the generated Stokes field at 1.10 μm , E_i is the input field at 10.6 μm , and E_o is the generated output at 16.95 μm .

If we neglect four-wave mixing for the moment, Eqs. (1a)–(1d) separate into two pairs of equations that describe stimulated Raman scattering pumped at E_p and E_i . In the absence of pump depletion, the Stokes power increases exponentially as $P_s(l) = P_s(0) \exp(g_s l)$, where $P_s(0)$ and $P_s(l)$ are the input and output Stokes power, respectively, and g_s is the Raman power-gain coefficient given by

$$g_s = \frac{\omega_s \chi_R'' |E_p|^2}{n_s c} = \frac{4\pi \chi_R'' I_p}{\lambda_s n_s n_p \epsilon_0 c}. \quad (2)$$

The input power to the Raman cell $P_s(0)$ is usually provided by blackbody or spontaneous Raman noise. In our case the spontaneous noise is dominant so that the noise in a single polarization and single spatial mode within the Raman linewidth $\Delta\nu_R$ is $P_s(0) = h\nu_s \Delta\nu_R \approx 10^{-12}$ W.¹¹ Thus, for a CO₂ pump power of 10 MW, the net gain required to amplify the spontaneous power up to the order of the pump power is $g_s l = \ln[P_s(l)/P_s(0)] = \ln[10^7 \text{ W}/10^{-12} \text{ W}] = 44$.

The 16.95- μm radiation generated by four-wave mixing can also be amplified by the stimulated Raman gain process. It has been previously shown^{5,6,9} and is evident from Eqs. (1a)–(1d) that the four-wave mixing conversion efficiency in the absence of significant Raman amplification and pump depletion is given by

$$\frac{I_o}{I_i} = \left(\frac{\omega_o}{\omega_i}\right) \text{supl} 2 \frac{n_i n_p I_s}{n_o n_s I_p}, \quad (3)$$

where I_i , I_o , I_s , and I_p are the intensities and n_i , n_o , n_s , and n_p are the refractive indices at the four fields. In the present case the Nd:YAG laser source at ω_p converts 40% of its energy to the Stokes wave by stimulated Raman scattering on the first transit of the 25-pass cell. The incident CO₂ laser intensity at ω_i then generates

output at ω_o by four-wave mixing. The generated output power at $16.95 \mu\text{m}$ is given by $P_o \approx 0.4(1.10 \mu\text{m}/16.95 \mu\text{m})^2 P_i \approx 1.68 \times 10^{-3} P_i$. A 10-MW CO_2 laser produces 16.8 kW or 134 μJ of energy in an 8-nsec pulse. In practice, less energy is produced because of the imperfect spatial overlap of the beams and the nonzero phase-mismatch factor Δk .⁶ The generated $16\text{-}\mu\text{m}$ energy is then amplified on the remaining passes by the CO_2 laser-pumped Raman gain.

The generated four-wave mixing power is 16 orders of magnitude greater than the spontaneous Raman power and thus significantly reduces the Raman gain required to reach threshold.¹⁰ The required net Raman gain with four-wave mixing injection is $g_s l = \ln[P_s(l)/P_o(0)] = \ln(10^7 W/10^1 W) \approx 7$. The required Raman gain and thus input pump power is, therefore, reduced by a factor of 44/7 or 6.2 times compared to the amplified spontaneous-emission case.

Figure 1 shows a schematic of the experimental apparatus. The CO_2 laser source consists of a Lumonics 103 oscillator followed by a Lumonics 102 amplifier. A Q-switched unstable resonator Nd:YAG laser operating at $1.064 \mu\text{m}$ provided the pumping for generating the four-wave mixing signal. The Nd:YAG laser pulse energy was limited to 70 mJ, which was 35 times the measured 2-mJ threshold because of the onset of damage of the metal turning mirror. The Nd:YAG and CO_2 beams were combined on a ZnSe plate and were focused into the multipass cell by a 9-m-radius mode-matching mirror. This optical arrangement assured that the four-wave mixing-generated $16.95\text{-}\mu\text{m}$ radiation had the proper spectral and spatial profile for amplification in the remaining passes of the cell.

The multipass cell consists of a 3.77-m-long, 15.24-cm-diameter stainless steel tube, with steerable 12.70-cm-diameter, 2-m-radius copper mirrors mounted at each end. Light is coupled into and out of the cell through salt windows mounted on the sides of the tube. Light entering the cell is directed down the axis of the tube by a 1.27-cm-diameter steering mirror. The beam then reflects back and forth between the 12.70-cm-diameter mirrors refocusing on each transit and walks in a circle around the rims of the mirrors. After 25 transits, the beam is coupled out of the multipass cell by a second 1.27-cm-diameter steering mirror and enters the screen room where spectral and energy measurements are made. A pyroelectric energy meter monitors the CO_2 energy. The $16\text{-}\mu\text{m}$ signal is separated from the $10\text{-}\mu\text{m}$ signal by a LiF reststrahlen re-

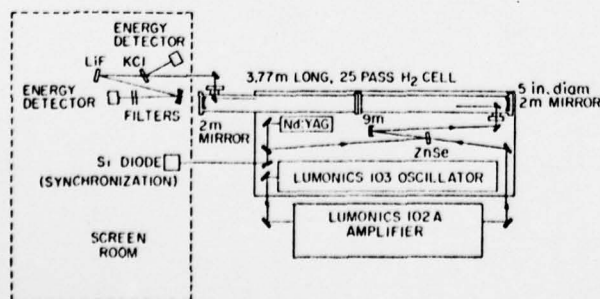


Fig. 1. Schematic of experimental apparatus.

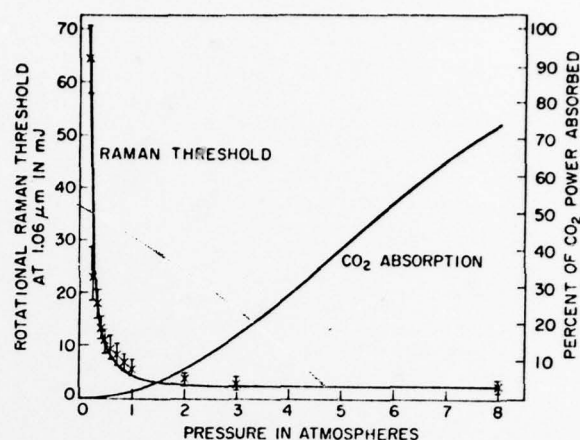


Fig. 2. Dependence of rotational Raman threshold at $1.06 \mu\text{m}$ and pressure-induced absorption at $10.6 \mu\text{m}$ on $p\text{-H}_2$ pressure.

flector followed by a dielectric bandpass filter and is also monitored by a pyroelectric energy meter. The wavelength of the Raman signal measured with a grating monochromator is $16.95 \mu\text{m}$, as expected.

Figure 2 shows the rotational Raman threshold dependence on $p\text{-H}_2$ pressure at $1.06 \mu\text{m}$ in the multipass cell. As the pressure increases, the threshold rapidly drops to about 2 atm, where it levels off at about 2 mJ. In a long cell, pressure-induced absorption in H_2 gas at $10.6 \mu\text{m}$ is significant and limits the maximum operating pressure. The second curve in Fig. 2 is a theoretical curve¹² showing the fraction of CO_2 energy absorbed versus H_2 pressure. Measurements of CO_2 transmittance versus pressure were in agreement with this curve. Taking both pressure-induced absorption and Nd:YAG threshold data into account, it is apparent that there is an optimum operating pressure of between 1 and 4 atm.

The Nd:YAG laser linewidth was also varied from single axial mode to about 0.5 cm^{-1} by inserting etalons into the Nd:YAG resonator. The Raman threshold was found to be independent of laser linewidth, in agreement with theory.^{13,14} Our CO_2 laser source was thus operated without linewidth control to obtain the maximum output pulse energy. Based on the Nd:YAG threshold measurements, we predicted a Raman threshold for the CO_2 laser of between 1.7 and 2.6 J in a 70-nsec pulse for 3 atm of $p\text{-H}_2$ in the multipass cell. The gas-breakdown limit in our present cell is 4.5-J input CO_2 energy.

With both the YAG and CO_2 lasers properly aligned and synchronized in the H_2 cell, significant $16\text{-}\mu\text{m}$ energies were generated. Figure 3 shows the $16\text{-}\mu\text{m}$ output energy versus CO_2 laser peak input power. The $\pm 50\text{-nsec}$ timing jitter between the YAG and CO_2 lasers resulted in large pulse-to-pulse variations in $16\text{-}\mu\text{m}$ energy. What is displayed are clusters of points that represent the best results at each CO_2 laser-power setting. The dots represent data taken at 1.5 atm, and the X's represent data taken at 3-atm H_2 pressure in the cell. An important point to notice is that the $16\text{-}\mu\text{m}$ energy is displayed on a log scale. An increase of 3 in CO_2 laser power results in an increase of 3 orders of

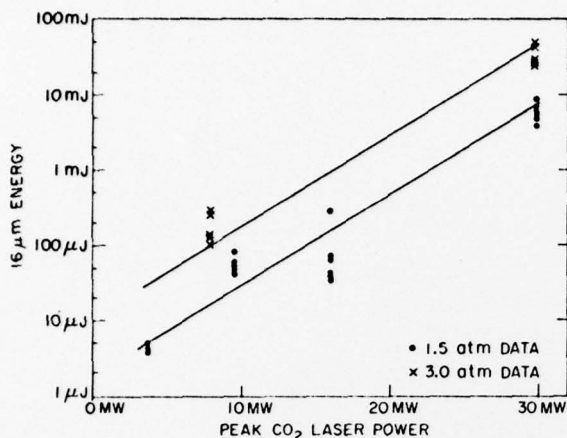


Fig. 3. Output energy at 16.95 μm versus CO_2 -laser peak input power.

magnitude in 16- μm energy. In a four-wave mixing process, the 16- μm energy should be limited to the 100- μJ level and increase linearly with CO_2 power. The exponential increase in 16- μm energy is due to CO_2 -pumped Raman gain. The slopes of the lines give the Raman exponential gain coefficient for the multipass cell, which is 0.28/MW. This gain coefficient is a factor of 3 less than the plane-wave gain value predicted from Nd:YAG laser threshold scaling and is accounted for by the spatial mode overlap factor of the 10.6- and 16.9- μm beams proportional to $(\lambda_s + \lambda_p)/\lambda_p$.

The maximum observed 16- μm pulse energies were 50 mJ. The 8-nsec-long 16- μm pulse generated by four-wave mixing was significantly shorter than the 70-nsec CO_2 -laser pulse, and, therefore, depleted a small portion of the energy in the CO_2 pulse. The 50-mJ pulse energy corresponded to a 27% peak power depletion or to a 40% peak photon conversion from 10.6 to 16.9 μm .

We have successfully used four-wave mixing injection to reduce the CO_2 power required to reach stimulated rotational Raman threshold on the $S(O)$ transition in $p\text{-H}_2$ gas. This technique should permit wider application of stimulated Raman scattering processes in the infrared as an efficient means of frequency conversion. The use of a tunable high-pressure CO_2 -laser source should permit continuous tuning over wide regions of the infrared extending from 8 μm to beyond 20 μm by the generation of Stokes and anti-Stokes output from various rotational levels of hydrogen and its isotopes.

The high conversion efficiency and direct scalability to high peak and average powers of CO_2 -pumped stimulated rotational Raman scattering should permit this approach to meet the large-scale isotope enrichment source requirements.

We acknowledge Westinghouse Research Laboratories and Exxon Research and Engineering Company for the major support of this research. Support was also provided by the Air Force Office of Scientific Research and the U.S. Department of Energy. We also thank A. E. Siegman for continued assistance and R. Mackenzie for equipment loans.

References

1. R. L. Byer, "A 16 μm source for laser isotope enrichment," *IEEE J. Quantum Electron.* **QE-12**, 732-733 (1976).
2. C. D. Cantrell, Los Alamos Scientific Laboratory, Los Alamos, N.M. 87545 (personal communication); S. R. J. Brueck, MIT Lincoln Laboratory, Lexington, Mass. 02173 (personal communication).
3. R. Frey, F. Pradere, J. Lukasik, and J. Ducuing, "Tunable millijoule radiation extending to the 16 μm region," *Opt. Commun.* **22**, 355-357 (1977).
4. J. A. Giordmaine and W. Kaiser, "Light scattering by coherently driven lattice vibrations," *Phys. Rev.* **144**, 676-688 (1966).
5. R. L. Byer, "Parametric oscillators," in *Tunable Lasers and Applications*, A. Mooradian, T. Jaeger, and P. Stokseth, eds. (Springer-Verlag, Berlin, 1976), pp. 70-80.
6. J. Ducuing, R. Frey, and F. Pradere, "Tunable infrared generation in molecular gases," in *Tunable Lasers and Applications*, A. Mooradian, T. Jaeger, and P. Stokseth, eds. (Springer-Verlag, Berlin, 1976), pp. 81-87.
7. S. J. Brosnan, R. N. Fleming, R. L. Herbst, and R. L. Byer, "Tunable infrared generation by coherent Raman mixing in H_2 ," *Appl. Phys. Lett.* **30**, 330-332 (1977).
8. P. P. Sorokin, M. M. T. Loy, and J. R. Lankard, "A 16 μm radiation source utilizing four wave mixing in cooled *para*-hydrogen gas," *IEEE J. Quantum Electron.* **QE-13**, 871-875 (1977); M. M. T. Loy, P. P. Sorokin, and J. R. Lankard, "Generation of 16 μm radiation by four wave mixing in *para*-hydrogen," *Appl. Phys. Lett.* **30**, 415-417 (1977).
9. R. L. Byer and R. L. Herbst, "Parametric oscillation and mixing," in *Topics in Applied Physics*, Vol. 16, *Nonlinear Infrared Generation*, Y. R. Shen, ed. (Springer-Verlag, Berlin, 1977).
10. G. V. Venkin, G. M. Krochik, L. L. Kulyuk, D. I. Maleev, and Yu. G. Khronopulo, "Effect of four wave parametric processes on the dynamics of the Stokes components of stimulated Raman scattering," *Sov. Phys. JETP* **43**, 873-879 (1977).
11. W. H. Louisell, A. Yariv, and A. E. Siegman, *Phys. Rev.* **124**, 1646-1654 (1961).
12. G. Birnbaum, "Far infrared absorption in H_2 and $\text{H}_2\text{-He}$ mixtures," *J. Quant. Spectrosc. Radiat. Transfer* **19**, 51-62 (1978).
13. R. L. Carman, F. Shimizu, C. S. Wang, and N. Bloembergen, *Phys. Rev. A* **2**, 60-72 (1970).
14. S. A. Akhmanov, Yu. E. D'yakov, and L. I. Pavlov, *Zh. Eksp. Teor. Fiz.* **66**, 520-536 (1974).